UNIVERSITY OF
LIVERPOOL

A GEANT4 Simulation of the SAGE Spectrometer and its First Application to ^{255}Lr

Thesis submitted in accordance with the requirements of the University of Liverpool for the degree of Doctor in Philosophy

by

Daniel Martin Cox

Oliver Lodge Laboratory
January 2014

Abstract

A two-part experiment studying ^{255}Lr was performed in the University of Jyväsklyä, Finland. The nucleus was created in the fusion-evaporation reaction ^{209}Bi(^{48}Ca,2n)^{255}Lr. The first part was performed using RITU and GREAT, and was run at a high intensity to study the decay properties of ^{255}Lr. The second part combined RITU, GREAT, and SAGE, and was run at a lower intensity to study excited states in ^{255}Lr.

In parallel a comprehensive GEANT4 simulation has for the SAGE spectrometer has been developed. With the goals of better characterising the experimental setup, and allowing the simulation of complex level schemes such as those seen in ^{255}Lr for the purposes of testing proposed level schemes by direct comparison to experimental data.

This thesis reports the results of both the decay and in-beam spectroscopy of ^{255}Lr, including observation of the previously seen isomeric state with a half-life of 1.73(4) ms and the observation of two previously unseen transitions in the ground-state rotational band at energies of 91 and 140 keV.

"A university is very much like a coral reef. It provides calm waters and food particles for delicate yet marvellously constructed organisms that could not possibly survive in the pounding surf of reality, where people ask questions like 'Is what you do of any use?' and other nonsense."

Science of Discworld
Terry Pratchet, Ian Stewart, and Jack Cohen

Acknowledgements

First and foremost I would like to thank my supervisor Prof. Rodi Herzberg for all his guidance and support during my PhD.

I am incredibly grateful to Philippos for the endless advice and patience over the last four years.

A big thank you to everyone at the University of Jyväskylä for all their help and support over the years and to all the people that brightened up my time there on experiments, far too many to name them all here, but especially all the past and present members of *Team Herzberg*, Philippos, Andy, Andrew, Fuad, and Eddie.

Thanks to all the students and postdocs in the Department for all the good times over the years, the conferences, the summer school, the beers, the incredibly varied and often surreal lunchtime conversations. It was never dull. Thanks must go to Pete, Joe, and Pete, for always patiently listening to my demented GEANT4 based ravings over the years. Special mention goes to my year mates, Mark, Joe, Pete, Anthony, and Baha for being there through it all, the highs and the lows.

My sincere gratitude goes to, again, Dr Philippos Papadakis and Dr Gemma Wilson for their skills as proof readers of this work. Without them, it wouldn't make much sense.

I would also like to acknowledge the STFC, for providing the necessary financial support for this research project.

Finally, I'd like to thank my family, especially my Mum, Dad, and sisters, Vikki and Kate for their endless support and encouragement. I couldn't have done it without you.

Contents

List of Figures

List of Tables

Chapter 1

Introduction

One of the major questions in nuclear physics has always been what is the limit of nuclear binding and to that end what is the heaviest nuclei that can exist. The study of superheavy nuclei, those at the higher extremes of mass and proton number, is at the forefront of this research as it is an excellent testing ground for nuclear models. The nucleus is made up of positively charged protons and uncharged neutrons held together by the strong force. As the number of protons increases, so does the Coulomb repulsion that they experience. According to the liquid drop model (LDM) [Boh37] Coulomb repulsion should become large enough to tear the nucleus apart for more than 104 protons [Kru00], clearly this is not the case however. Elements with Z up to 118 have been produced with relatively long half-lives [Oga07]. There must be other factors contributing to the binding of the nucleus.

The LDM was the first model to accurately describe nuclear properties such as the general trend in binding energy. There were however many effects that it failed to describe such as the enhanced stability at specific numbers

of protons and neutrons. From this came the idea that the nucleons had specific arrangements in the nucleus, much like atomic electrons, and from this arose the shell model.

There is a vast amount of experimental evidence for the existence of magic numbers at 2, 8, 20, 28, 50, 82, for protons and neutrons, and also 126 for only neutrons [Cas01]. Furthermore, the next magic number, its value and its very existence are greatly debated. Comparison of experimental observations with theoretical models is vital to answering questions such as where is the next island of stability? What is the heaviest bound nucleus that can exist?

According to theoretical predictions it is expected that a doubly magic superheavy nucleus will have enhanced stability [Nil68, Nil69, Ćwi05]. This should lead to a so-called "island of stability" [Sto06, Oga00] though the limits of this are unknown.

The upper panel of Figure 1.1 shows theoretical shell closures for Z=50 nuclei. There is little variation within the models shown, and they all strongly agree on Z=50 and N=82 being the most strongly bound. In the lower half of this plot, however, there appears to be no definite closed shell but more an area of increased stability centred between Z=114 and Z=126 depending on the model.

Theoretical models can be split into two categories, microscopic-macroscopic models and self-consistent mean-field models. The former consist of a smoothly varying component described by the LDM, and an oscillatory component described by the shell model. The latter are formed by an iterative procedure where an initial guess of the wavefunction is chosen to calculate the potential, then this potential is used to calculate a new wavefunction un-

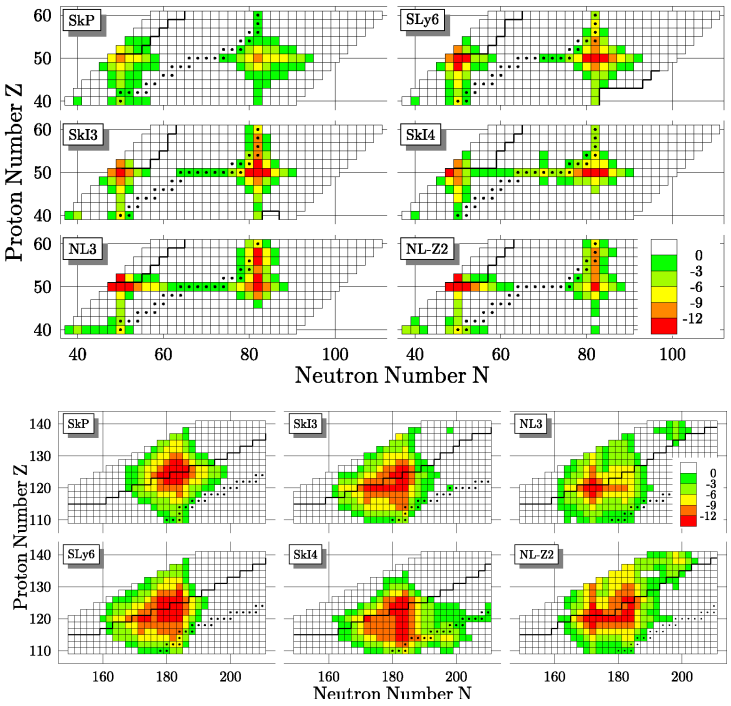

Figure 1.1: Self-consistent mean-field calculations for shell correction energies, in MeV,for the Z∼50 region, and the super heavy nuclei[Ben01].

til self-consistent convergance is achieved, and entirely shell model based. Microscopic-macroscopic models generally predict the next doubly magic nucleus to have Z=114 and N=184 [Nil68, Nil69, Par05, Par04, Möl94, Möl92]. Self-consistent models, however, generally disagree with the microscopic-macroscopic predictions. Comparisons of the mean-field calculations [Kru00, Ben01] indicate that non-relativistic models [Ćwi96, Ben99] give Z=124-126 and N=184. Relativistic models [Afa03, Ben03, Lal96, Ben99] predict a higher Z=120 and a lower N=172. A detailed review of experimental studies relevant to these calculations can be found in [Her11].

Experimentally, these superheavy nuclei are very difficult to produce. The

cross section for production of these elements is so low, that one event may be detected in a day, a week, or even longer. With the heaviest studied so far being $^{294}_{176}118$ [Oga06]. Here only 3 decay chains were detected in over 45 days of experiment. These extremely low production cross sections for superheavy nuclei, <1 pb for element 118 [Arm03] mean that is not possible to get spectroscopic information. The heaviest nucleus to have any spectroscopic information measured is $^{288}115$ [Rud13]. As can be seen in Figure A.1, some states that are involved in the closed shell at Z=114, drop in energy with increasing deformation. Owing to this, these states are accessible in excitations of lighter deformed nuclei in the Z$\sim$102 region. These nuclei are relatively easy to produce in fusion evaporation reactions with cross sections in the microbarn to nanobarn region. This allows for detailed spectroscopic analysis, which can then be used to inform the theory of heavier spherical nuclei.

In-beam spectroscopic studies in γ-rays and conversion-electrons being studied independently have lead to important insight into information such as rotational structure, deformation and stability against fission. Even-even nuclei such as ^{254}No [Her02, Her06] and ^{250}Fm [Gre08, Ros09, Bas06] have been separately studied in both γ-ray and conversion-electron detection experiments. Odd-mass nuclei do provide a more sensitive probe into single-particle structure at the cost of increased complexity, especially when studied independently with γ-rays or conversion-electrons. Odd-mass nuclei ^{253}No [Rei04, Rei05, Moo07], ^{251}Md [Cha07], ^{255}Lr [Ket09] have been studied in γ-ray, with ^{253}No also being studied in conversion electrons [Her02, Her09].

In ^{253}No a strongly coupled rotational band with intra-band E2 and M1

transitions has been established. The M1 transitions were not observed in the early γ-ray experiments [Rei05, Rei04] owing to their low energy and high conversion coefficients but were observed in the following conversion electron study [Her02, Her09]. Later, in higher intensity γ-ray studies, some of these M1 transitions were seen, but lower energy transitions still remain undetected. This case is similar to that of ^{255}Lr, where alongside the ground state rotational band, a strongly coupled rotational band band has been detected [Ket09]. The statistics were not high enough here to measure any M1 transitions.

In this case a combined γ-ray and conversion electron study of ^{255}Lr has a higher sensitivity to these highly converted low-energy transitions whilst retaining the ability to observe the higher energy known transitions, though the cross section to produce ^{255}Lr is very close to the current experimental limit with the lowest cross section studied in-beam being 60 nb for ^{256}Rf [Rub13]. With that in mind it was decided that to meaningfully interpret the results it was required to better understand the experimental response. To that end a comprehensive GEANT4 simulation has been developed with the aim of reproducing experimental data for purposes of testing proposed level schemes and comparing to experimental data.

In this study, after an overview of the relevant theoretical framework, an experiment with the aim of studying excited states in ^{255}Lr will be presented. The experiment was performed at the University of Jyväskylä using the reaction ^{209}Bi(^{48}Ca,2n)^{255}Lr in two parts with a high intensity decay study at a beam intensity of $\sim$110 pnA[1] and a lower intensity in-beam study at $\sim$10 pnA.

[1]Particle nanoampere (1 pnA = 6.25×10^9 particles incident on target)

Alongside this a comprehensive simulation package has been developed using the GEANT4 toolkit [Ago03]. This simulation has been designed to include all relevant geometries for the emission, tracking and subsequent detection of γ-rays and conversion-electrons within the SAGE spectrometer. Within this simulation there is the ability to enter possible structures and decays and reproduce the experimental response for that decay, which can then be directly compared to the experimentally acquired data. Finally results of this spectroscopic study will be shown and compared to simulated data.

Chapter 2

Theoretical Framework

2.1 Liquid Drop Model

The LDM was one of the first models proposed to explain the properties of the nucleus [Boh37]. The LDM treats the nucleus as an incompressible liquid drop. This model successfully describes bulk properties of the nucleus, such as fission, fusion, and α decay. However it fails to explain the experimental observations of systematic deviations in properties such as binding energy, nuclear charge radii, and the energy of the first excited state. It also fails to explain to stability of superheavy nuclei since according to the liquid drop model, nuclei with Z$\geq$104 would be unbound. This led to the development of the shell model [GM49].

2.1.1 Binding Energy

The binding energy, B, of a nucleus is defined as the energy required to separate it into its constituent protons and neutrons. The mass of a bound

nucleus is lower than the mass of its constituent particles by B/c^2 which then follows that

$$B(Z,A) = \big(Zm_p + Nm_n - M(Z,A)\big)c^2, \tag{2.1}$$

from [Boh98], where m_p and m_n are the masses of the proton and neutron, and *M(Z,A)* is the observed mass in the ground state.

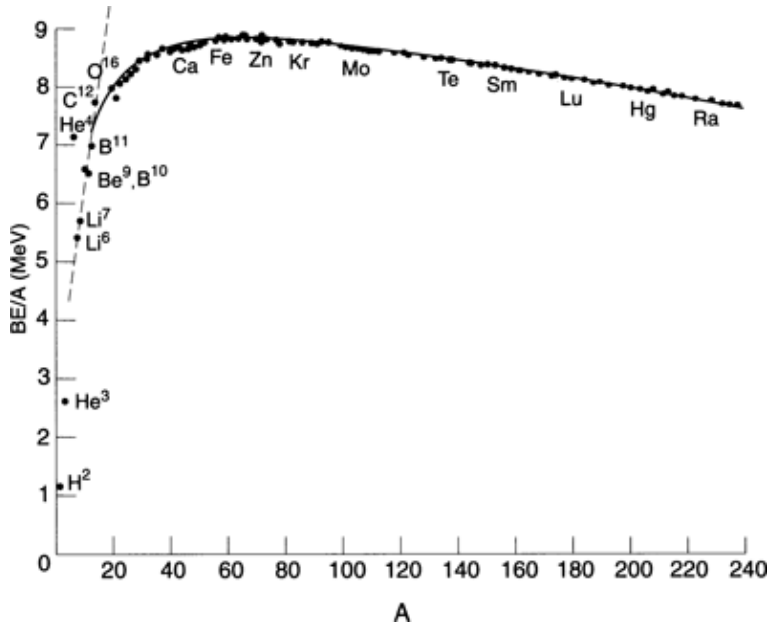

Figure 2.1: A plot of binding energy per nucleon as a function of mass number [Cas01].

Binding energy is most often described in the form of binding energy per nucleon, as shown in Figure 2.1, where binding energy per nucleon is plotted as a function of mass number. There are a number of interesting conclusions that can be drawn from this plot. The binding energy per nucleon increases quickly until *A∼10*, then there is a slower increase to *A∼60*, above this *B/A* is almost constant, though it slowly decreases with increasing A. The interpretation of this trend is as follows: if every nucleon were to contribute to the

attractive force experienced by each nucleon in the nucleus, B would increase proportionally with A^2. This is not the case however, as B/A saturates at a maximum of just over 8 MeV. This indicates that each nucleon only feels an attractive force from its nearest neighbours. From this it follows that the nuclear force is a short range force. The fluctuations at low A show the discrepancies of the LDM, which will be discussed in more detail in later sections.

2.1.2 Semi-Empirical Mass Formula

Weizsäcker [Wei35] derived an empirically refined formulation of the LDM to describe the relatively smooth variation in the binding energy with respect to mass number. The formula is written as:

$$M(Z,A) = Zm_H + Nm_n - \frac{1}{c^2}B(Z,A), \tag{2.2}$$

from [Boh98], where the binding energy is given as

$$B(Z,A) = a_v A - a_s A^{2/3} + a_c Z(Z-1)A^{-1/3} - a_{sym}\frac{(A-2Z)^2}{A} + \delta. \tag{2.3}$$

The first three terms in the Equation 2.3 can be explained by considering the terms in the LDM:

- The volume term, $a_v A$, where a_v is constant. This arises due to all nucleons having the same number of neighbours.
- The surface term, $a_s A^{2/3}$, where a_s is constant. This counteracts the volume term, as surface nucleons are less tightly bound, owing to a

lower number of neighbouring nucleons.

- The Coloumb term, $a_c Z(Z-1)A^{-1/3}$, where a_c is constant. This term accounts for the repulsion between protons within the nucleus and becomes more significant in heavier nuclei.

The first three terms of Equation 2.3 fail to describe the curve shown in Figure 2.1, especially for large A. This is where the LDM breaks down and shell effects become important. The fourth term accounts for the fact that in light nuclei, binding energy is maximal for Z=N. For larger nuclei, this is no longer the case due to the tendency for the neutron-proton interactions being stronger than for like particles owing to the Pauli exclusion principle. This symmetry term is of the form $-a_{sym}(A-2Z)^2/A$, where a_{sym} is constant. The final term, δ, is the pairing term, and accounts for alike nucleons forming pairs, increasing stability in even nuclei. This term is positive for even-even nuclei, negative for odd-odd nuclei and zero for even-odd nuclei. These five terms combined give a relatively accurate description of the trend of nuclear binding energy relative to mass [Cas01].

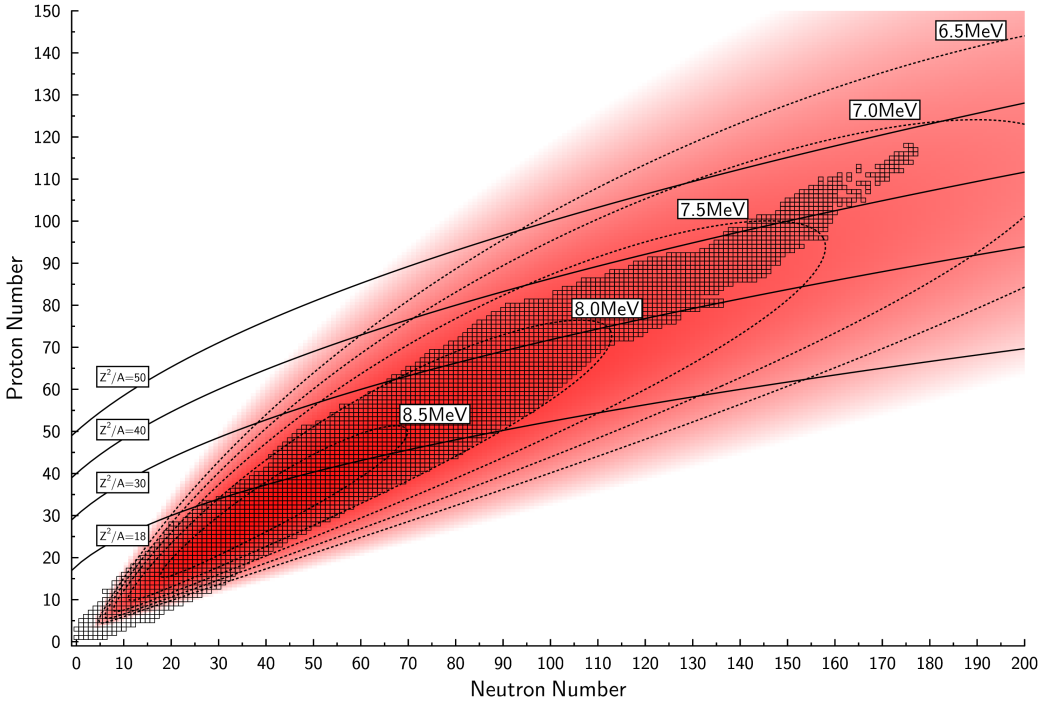

Figure 2.2: Chart of nuclides overlaid with the predicted binding energy per nucleon according to the liquid drop model, also line for various values of Z^2/A tracking the fissility [Sch13].

Figure 2.2 shows the binding energy per nucleon overlaid onto the chart of nuclides. Although the liquid drop binding energy cannot describe the limits of nuclear stability, it does track remarkably well. Also overlaid are the facilities for fission and it can be seen that $Z^2/A = 40$ tracks the upper limit of known nuclei to a neutron number of around 150 and a proton number of around 100. Above this, it can be seen that the LDM is breaking down.

2.2 Spherical Shell Model

The LDM can describe a number of the bulk properties of nuclei, but it fails at describing the quantal effects. The clearest of which is the existence of anomalously stable nuclei at certain configurations of nuclei, namely nuclei with nucleon numbers 2, 8, 20, 28, 50, 82, and also 126 for neutrons. The magic numbers form the strongest experimental motivation for the formulation of the shell model. Further to this are the discontinuities in the binding energy as a function of mass for these magic-number nuclei. The first excited 2^+ states in these magic-number nuclei are also significantly higher than in neighbouring nuclei [Cas01].

The spherical shell model makes the assumption that each nucleon moves independently within the nucleus. The nucleons move within a uniform potential resulting from the averaged interactions of all the nucleons.

The system can be described by the nuclear Hamiltonian H, defined as

$$H = \sum_{i=1}^{A} -\frac{\hbar^2}{2m}\bigtriangledown_i^2 + \sum_{ij}^{A} V(r_{ij}), \tag{2.4}$$

where the first term is the sum of the individual kinetic energies, and the second term describes the potential acting on all nucleons. This can be rewritten in the form

$$H = \sum_{i=1}^{A} \big[-\frac{\hbar^2}{2m}\bigtriangledown_i^2 + V(R_i)\big] + \big[\sum_{ij} v(r_{ij}) - \sum_{i} V_i(r_i)\big], \tag{2.5}$$

by adding and subtracting a one-body interaction. This can then be simpli-

fied to

$$H = \sum_{i=1}^{A} h_i + V_{res}, \tag{2.6}$$

where V_{res} is a small perturbation on the Hamiltonian for a system of nearly independent nucleons orbiting in a common mean field potential.

The shell model assumes that this residual interaction is significantly smaller than the central interaction [Cas01].

2.3 Nilsson Model

The Nilsson model was first proposed by Nilsson [Nil55] in 1955. Nilsson proposed that a deformed nuclear potential could be described by an anisotropic harmonic-oscillator potential. The model considers a single valence particle undergoing rapid orbital motion around a relatively stationary axially symmetric deformed core. The core has angular momentum $\underline{R}$, and the single particle has angular momentum $\underline{J}$. Thus to total angular momentum $\underline{I}$ can be written,

$$\underline{I} = \underline{R} + \underline{J}. \tag{2.7}$$

The projection of $\underline{I}$ onto the symmetry axis (z) is K as shown in Figure 2.3. When there are two single particles, their projections of $\underline{j_1}$ and $\underline{j_2}$ onto the symmetry axis are equal to Ω_1 and Ω_2, which sum to K. A single-particle orbiting a deformed core can be completely described by the Nilsson quantum numbers

$$\Omega^{\pi}[Nn_z\Lambda], \tag{2.8}$$

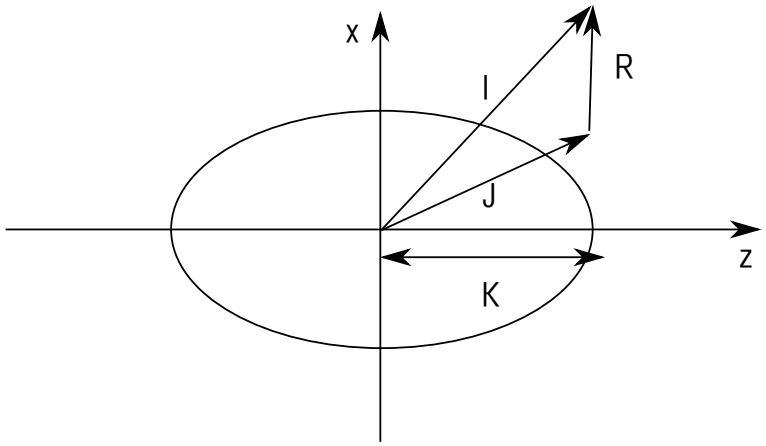

Figure 2.3: Schematic representation of angular momentum coupling of a prolate nucleus with a single particle orbiting.

where N is the principal quantum number, denoting the major shell, n_z is the number of oscillator quanta along the symmetry axis, Λ is the projection of the orbital angular momentum (l) onto the symmetry axis, and Ω is the projection of the total angular momentum j. Parity, π is (-1)^N.

The labels are used to identify single-particle states in the Nilsson diagram showing single-particle energy plotted against deformation. The Nilsson diagrams for proton ($Z \geq 82$) and neutrons ($N \geq 126$) are shown in Appendix A.

2.4 Nuclear Rotation

By considering the energy possessed by a rigid rotating body the energy levels of a rotational band are given,

$$E(I) = \frac{\hbar^2}{2J_0}(I(I+1)). \tag{2.9}$$

This equation defines the static moment of inertia, J_0. This assumes that the nucleus behaves like a rigid body under rotation, which is not the case as the moment of inertia changes with increasing rotation. To quantify this, the rotational frequency, ω, must be defined. It is classically defined as

$$\hbar\omega = \frac{dE}{dI_x}, \tag{2.10}$$

where I_x is the projection of the total angular momentum onto the rotation axis, given by $I_x = \sqrt{I(I+1) - K^2}$. Quantum mechanically ω becomes,

$$\hbar\omega = \frac{dE(I)}{d\sqrt{I(I+1) - K^2}}. \tag{2.11}$$

Note that in the even-even case, as $\underline{J}$=0 and $\underline{I}$=$\underline{R}$, thus K=0 and equation 2.11 simplifies to

$$\hbar\omega \sim \frac{E_\gamma}{2}, \tag{2.12}$$

where E_γ is the γ ray energy given by $E(I) - E(I-2)$.

The kinematic and dynamic moments of inertia J_1 and J_2 are the first and second order derivatives of Equation 2.9 and provide a useful perspective from which to examine rotational bands. Thus, in the case where $I \sim I_x$, the kinematic moment of inertia is defined as

$$J_1 = \left(\frac{2}{\hbar^2} \frac{dE(I)}{dI} \right)^{-1} = \hbar \frac{I}{\omega}, \tag{2.13}$$

and the dynamic moment of inertia is defined as

$$J_2 = \left(\frac{1}{\hbar^2} \frac{d^2 E(I)}{dI^2} \right)^{-1} = \hbar \frac{dI}{d\omega}. \tag{2.14}$$

When examining a rotational band, these quantities are related to the transition energies such that J_1 becomes

$$J_1 = \frac{\hbar^2 (2J - 1)}{E_{\gamma(J \to J-2)}}, \tag{2.15}$$

and J_2 becomes

$$J_2 = \frac{4\hbar^2}{E_{\gamma(J+2 \to J)} - E_{\gamma(J \to J-2)}}, \tag{2.16}$$

for a state with angular momentum I. The kinematic and dynamic moments of inertia are related via the expression

$$J_2 = J_1 + \omega \frac{dJ_1}{d\omega}. \tag{2.17}$$

2.5 Isomerism

There is no solid definition of what an isomer is, but it is generally considered to be a meta-stable excited state with a lifetime of greater than 1 ns [Wal99]. Shown in Figure 2.4, are three types of isomer: shape, spin trap, and K-trap. Shape isomerism occurs when there is a secondary energy minimum at large deformation of the nucleus; the primary energy corresponds to the ground-state. Spin trap isomerism is more common and depends on the spin selection rules whereby the decay to a lower energy state requires a

large change in nuclear spin. This means that an emission of radiation with high multipolarity is needed; these high multipolarity transitions are greatly hindered and so electromagnetic decay can take a long time to occur. K isomerism occurs in much the same way as shape isomerism though in this case it is a secondary minimum for the potential energy at a value of K, the spin projection. In Figure 2.4 the three described isomers are shown, on the left a nucleus is shown to have two local minima in the potential energy plot as a function of shape elongation. In the centre, a nucleus has a secondary minimum as a function of spin. Finally on the right, a nucleus has a secondary minimum as a function of spin projection.

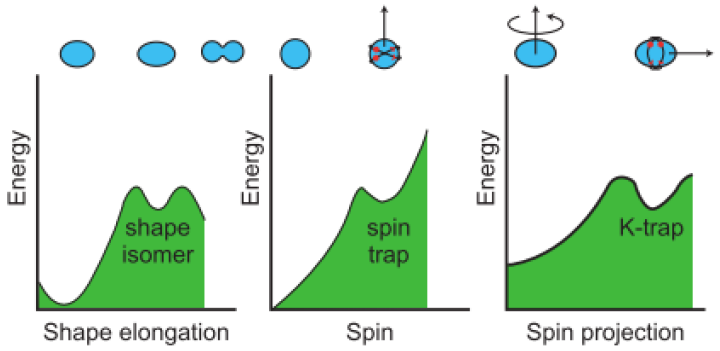

Figure 2.4: Illustration of different types of isomers taken from [Wal99].

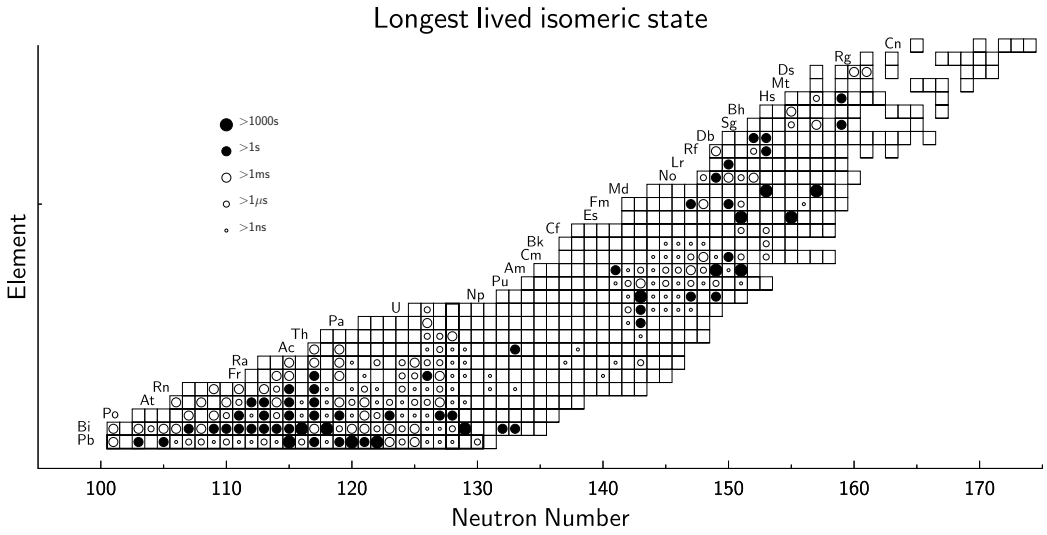

Figure 2.5: A section of Segré chart, showing the longest lived isomers Z≥82 [Her11].

Figure 2.5 details the currently known longest lived isomeric states above the closed shell at *Z=82*. It can be seen that there is a wealth of information on isomeric states with nuclei in the *Z∼95* region. Fewer isomeric states are known for higher-mass nuclei. However those that are known generally have half-lives in excess of 1 ms. These isomeric states are often caused by very pure single-particle states and can provide a great testing ground for nuclear theories.

2.6 Alpha Decay

Alpha decay is one of the main modes of decay for superheavy nuclei. This can be understood by looking at how the involved forces scale with the size of the nucleus. The repulsion of the Coulomb force increases with Z^2, whereas

the stabilisation of the nuclear binding force only scales with A. Alpha decay (emission of a ^{4}He nucleus) can be written in the form

$$ {}^{A}_{Z}X_N \rightarrow {}^{A-4}_{Z-2}X'_{N-2} + \alpha, \tag{2.18} $$

where X' is the nucleus after α emission. Applying conservation of momentum and energy to the α emission process, the energy emitted, the Q value, is given by

$$ Q = M_X - M_{X'} - M_\alpha = T_{X'} + T_\alpha, \tag{2.19} $$

where M_X, $M_{X'}$, and M_α are the nuclear masses of the mother, daughter and α particle, respectively. $T_{X'}$ and T_α are the kinetic energies of the daughter nucleus the α particle, respectively. From equation 2.19, it can be seen that Q is equal to the total kinetic energy of the fragments. It is also clear that α decay can only happen spontaneously should the Q value is positive. Although it should be noted that α decay does not become prominent until Q reaches the order of several MeV.

Due to its composition the α particle has spin and parity of 0^+ meaning it can only take orbital angular momentum l_α within the range $|I_i - I_f| < l_\alpha < I_i + I_f$. The angular momenta of the initial and final states of the mother and daughter nuclei are given by I_i and I_f respectively. The parity change after α emission is given by $(-1)^{l_\alpha}$. Additionally if the angular momentum of the emitted α particle is non-zero, the decay will be hindered by a centrifugal barrier effect.

The probability of α decay is given by

$$P_{\alpha\ decay} = P_{preformation} \times P_{tunnel} \tag{2.20}$$

where $P_{preformation}$ is the probability that an α particle will form in the nucleus and P_{tunnel} is the probability that this α particle will then tunnel out of the nucleus.

2.6.1 Fine Structure

Fine structure occurs when a nucleus emits α particles of more than one energy, possibly from more than one state, thus populating excited states in the daughter nucleus. In even-even nuclei, ground state to ground state decay is generally the most frequent. This is not necessarily true for odd nuclei. In odd nuclei, ground state to excited state, excited state to excited state and excited state to ground state can occur. The resulting fine structure can provide important information about both mother and daughter nuclei, such as information about single-particle structure when a populated state subsequently decays.

2.7 Electromagnetic Decay

When an excited state, with a spin I_i, decays to another state, with spin I_f, electromagnetic radiation in the form of a γ ray can be emitted. The energy of the γ ray, E_γ, is directly related to the energy of the initial and final states, $E_\gamma = E_i - E_f$. This also has the effect that the energy of the

γ rays is quantised, taking only certain values. This makes detecting and studying the γ-rays emitted incredibly useful in understanding the structure of nuclear matter. It should also be noted that the kinetic energy of the recoiling nucleus can be ignored in this case as this energy small compared to that of the γ rays of interest.

Gamma rays can be classified according to their electromagnetic character and multipolarity, L. Due to conservation of angular momentum and parity, π, selection rules arise, which determine whether the emitted radiation is electric (EL) or magnetic (ML) in nature, where L denotes the order of the multipole.

The emitted γ ray can carry away L units of angular momentum, measured in units of $\hbar$, which is limited by the selection rule

$$\begin{aligned} |I_i - I_f| \leq L \leq I_f i + I_f; \\ L \neq 0. \end{aligned} \tag{2.21}$$

The nature of the emitted γ ray is defined by conservation of parity rules,

$$\pi_i \pi_f = \pi_L, \tag{2.22}$$

where π_i is the parity of the initial state, π_f is the parity of the final state, and π_L is the parity of the emitted photon, where

$$\Delta\pi_{EL} = (-1)^L, \tag{2.23}$$

$$\Delta\pi_{ML} = (-1)^{L+1}. \tag{2.24}$$

For transitions between states π_i and π_f, $\Delta\pi = +1$ corresponds to no parity change, whereas $\Delta\pi = -1$ corresponds to a parity change. It can be seen that E1, M2, E3, and M4 transitions will induce a change in parity, whereas M1, E2, M3, and E4 transitions will not.

If the γ ray carries away the maximum amount of angular momentum, it is said to be a stretched transition. If a non-maximal amount of angular momentum is carried away, the transition is referred to as folded. Transitions can be formed of an admixture of different multipoles, though an electric transition will always dominate a magnetic transition of the same multipole value. M1 and E2 admixtures are reasonably common. When a transition is formed by the mixing of two components, the mixing ratio is denoted as δ, given by,

$$\delta^2_{E2/M1} = \frac{T(E2, I \to I-1)}{T(M1, I \to I-1)}. \tag{2.25}$$

2.7.1 Weisskopf Estimates

The total transition probability from a state with spin I_i to a state with spin I_f can be written as [Boh98]

$$T_{fi} = \frac{8\pi(L+1)}{\hbar L[(2L+1)!!]^2}(\frac{E_\gamma}{\hbar c})^{2L+1} B(\sigma L; I_i \to I_f), \tag{2.26}$$

where $B(\sigma L)$ is the reduced transition probability given by

$$B(EL, I_i \to I_f) = \frac{1}{2I_i+1}| < f\|\hat{Q}\|i > |^2, \tag{2.27}$$

for the electric case, and

$$B(ML, I_i \rightarrow I_f) = \frac{1}{2I_i + 1} | < f \| \hat{M} \| i > |^2, \tag{2.28}$$

for the magnetic case. Here $\hat{Q}$ and $\hat{M}$ are the electric and magnetic multipole operators, respectively.

To ease calculation of these terms, Weisskopf [Wei51] made a number of simplifying assumptions about the nucleus. Firstly a transition is assumed to be due to a single proton changing from one spherical single-particle state to another. Secondly, the radial part of the nuclear wavefunction is replaced with a constant within the nuclear interior, and assumed to be zero outside of the nuclear volume. Finally angular momentum coupling is neglected. From these assumptions the following can be obtained:

$$B(EL) = \frac{(1.2)^{2L}}{4\pi} (\frac{3}{L+3})^2 A^{\frac{2L}{3}} [e^2 (fm)^{2L}] \tag{2.29}$$

for the electric transitions and

$$B(ML) = \frac{10}{\pi} (\frac{3}{L+3})^2 A^{\frac{2L-2}{3}} [\mu_N^2 (fm)^{2L-2}] \tag{2.30}$$

for the magnetic transitions, where A is the atomic number.

Table 2.1 shows expressions for the single-particle estimates for transition probabilities as described in Equations 2.29 and 2.30.

Transition Probabilities T(s^{-1})	Weisskopf Units B_{sp}
T(E1)=$1.587 \cdot 10^{15} \cdot E^3 \cdot B(E1)$	$B_{sp}(E1) = 6.446 \cdot 10^{-2} \cdot A^{2/3}$
T(E2)=$1.223 \cdot 10^{9} \cdot E^5 \cdot B(E1)$	$B_{sp}(E2) = 5.940 \cdot 10^{-2} \cdot A^{4/3}$
T(E3)=$5.698 \cdot 10^{2} \cdot E^7 \cdot B(E3)$	$B_{sp}(E3) = 5.940 \cdot 10^{-2} \cdot A^{2}$
T(E4)=$1.694 \cdot 10^{-4} \cdot E^9 \cdot B(E4)$	$B_{sp}(E4) = 6.285 \cdot 10^{-2} \cdot A^{8/3}$
T(M1)=$1.779 \cdot 10^{13} \cdot E^3 \cdot B(M1)$	$B_{sp}(M1) = 1.790$
T(M2)=$1.371 \cdot 10^{7} \cdot E^5 \cdot B(M2)$	$B_{sp}(M2) = 1.650 \cdot A^{2/3}$
T(M3)=$6.387 \cdot 10^{0} \cdot E^7 \cdot B(M3)$	$B_{sp}(M3) = 1.650 \cdot A^{4/3}$
T(M4)=$1.899 \cdot 10^{-6} \cdot E^9 \cdot B(M4)$	$B_{sp}(M4) = 1.746 \cdot A^{2}$

Table 2.1: Transition probabilities T (s^{-1}) for Weisskopf single particle estimates expressed as B(EL) and B(ML). The energies E are measured in MeV [Rin04]

2.7.2 Internal Conversion

An excited nucleus can decay to a lower energy state by the emission of a γ ray. There are other processes that compete with γ-ray emission, one of which is the emission of a conversion electron. Conversion-electron emission is a process whereby the nucleus interacts with a bound atomic electron, causing this electron to be ejected from the atom. This process is completely separate from β decay, in which an electron is emitted from the nucleus via the decay of a neutron into a proton, an electron, and an electron anti-neutrino.

As this process is the result of a two-body interaction with a transition between two well defined states, the energy imparted on the electron will be well defined. This is not the case in β decay, where the emitted electron has a range of allowed energies owing to the three bodied nature of the interaction.

Atomic electrons are in bound states; the strength of this binding depends on the shell which they occupy. This means that the total kinetic energy

Electron Shell	B (keV)
K	152.970
L_1	30.038
L_2	29.103
L_3	22.359
M_1	7.930
M_2	7.474
M_3	5.860
M_4	5.176
M_5	4.876

Table 2.2: Table of atomic electron binding energies for the innermost transitions in lawrencium [Fir99]

of the electron will not be the same as the γ ray resulting from the same transition. The kinetic energy of the emitted electron, T_e, can be described by

$$T_e = \Delta E - B. \tag{2.31}$$

The binding energy B, will depend on the shell from which the electron is ejected, i.e. the K, L, M, ... shells. Table 2.2 shows the binding energies for the innermost transitions in lawrencium. The difference in strength between the competing γ-ray emission and conversion-electron emission can vary dramatically; one process may dominate or they can be much closer in strength. The probability of each decay mode occurring, for a given transition, is described by the internal conversion coefficient, α, which is defined as the relative probabity of the decay occuring via conversion-electron emission versus γ-ray emission.

$$\alpha = \frac{N_e}{N_\gamma} = \frac{\lambda_e}{\lambda_\gamma} = \alpha_K + \alpha_{L_1} + \alpha_{L_2} + \alpha_{L_3} + \alpha_{M_1} + \ldots, \tag{2.32}$$

where λ denotes the decay probability of the respective decay mode. From, this the total electromagnetic decay rate can be written as

$$\lambda_t = \lambda_\gamma(1+\alpha) = \lambda_\gamma(1+\alpha_K+\alpha_{L1}+\alpha_{L2}+\dots). \tag{2.33}$$

Internal conversion coefficients for a point nucleus can be defined as

$$\alpha(EL) \cong \frac{Z^3}{n^3}\Big(\frac{L}{L+1}\Big)\Big(\frac{e^2}{4\pi\epsilon_0\hbar c}\Big)^4\Big(\frac{2m_ec^2}{E}\Big)^{L+5/2}, \tag{2.34}$$

for electric multipoles and

$$\alpha(EL) \cong \frac{Z^3}{n^3}\Big(\frac{e^2}{4\pi\epsilon_0\hbar c}\Big)^4\Big(\frac{2m_ec^2}{E}\Big)^{L+3/2}, \tag{2.35}$$

for magnetic multipoles [Kra87].

Some general trends of internal conversion coefficients can be drawn from Equations 2.34 and 2.35.

- Internal conversion increases rapidly with nuclear charge (atomic number Z).
- Internal conversion decreases with increasing transition energy (E).
- The probability for internal conversion increases for higher L transitions (L).
- The probability for internal conversion decreases for higher atomic shells (n).

For high multipole, low-energy transitions in heavy nuclei, such as ^{255}Lr, conversion coefficients can be very high, of the order $\sim$1000. This means that

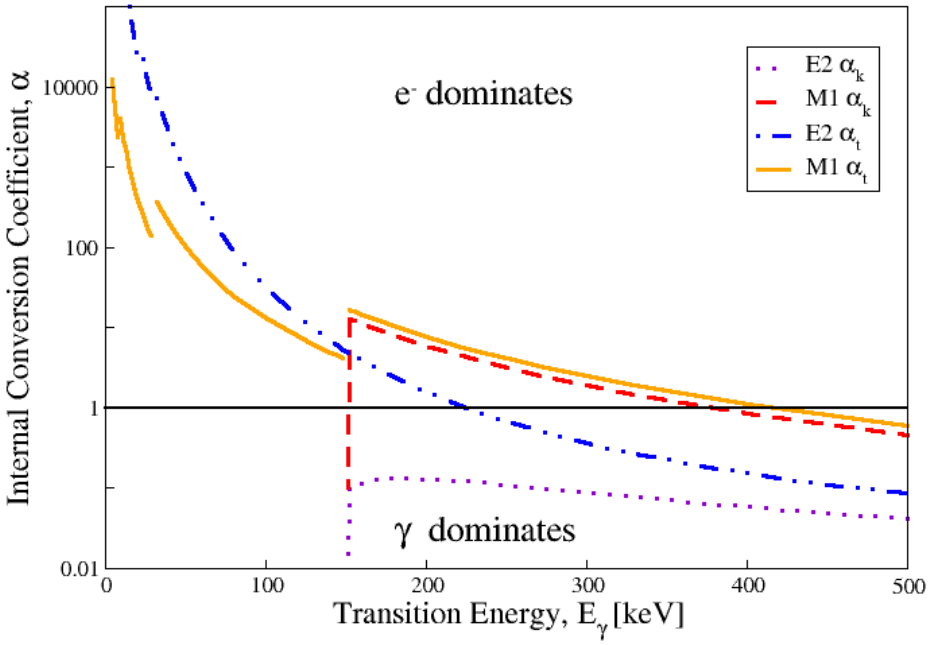

Figure 2.6: Internal conversion coefficients α_k and α_{tot}, as a function of energy for E2 and M1 transitions in lawrencium.

transitions could be completely unseen in γ-ray spectroscopy but strong in electron spectroscopy.

Figure 2.6 details the conversion coefficients as a function of energy for M1 and E2 transitions, for both K and total conversion. It is interesting to note that K conversion cannot occur below the K binding energy of the given nucleus, in this case lawrencium. It is also clear how strongly low energy transitions will be converted.

Chapter 3

Experimental Methods

3.1 SAGE Spectrometer

The SAGE spectrometer [Pap10] consists of the JUROGAM II germanium detector array coupled to a solenoidal magnet which transports conversion electrons to the SAGE silicon detector.

3.1.1 JUROGAM II array

The JUROGAM II array [Bea96] consists of 24 fourfold segmented Clover dectors [She99], and 15 EUROGAM Phase I type Compton-suppressed germanium detectors [Nol94, Bea92], though to accommodate the solenoidal magnet of SAGE, 5 of these Phase I detectors need to be removed leaving 10 Phase I's.

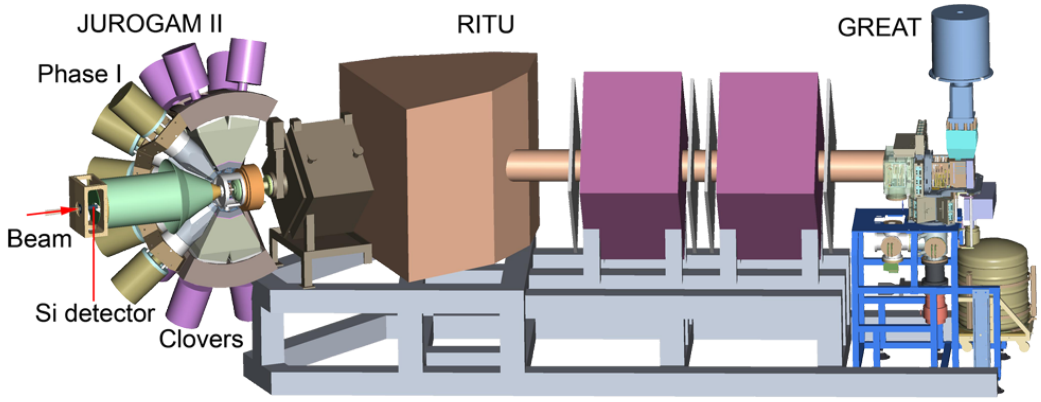

Figure 3.1: Schematic Diagram of the setup at Jyväskylä, showing JUROGAM II and the SAGE silicon detector along with RITU and GREAT [Pap09].

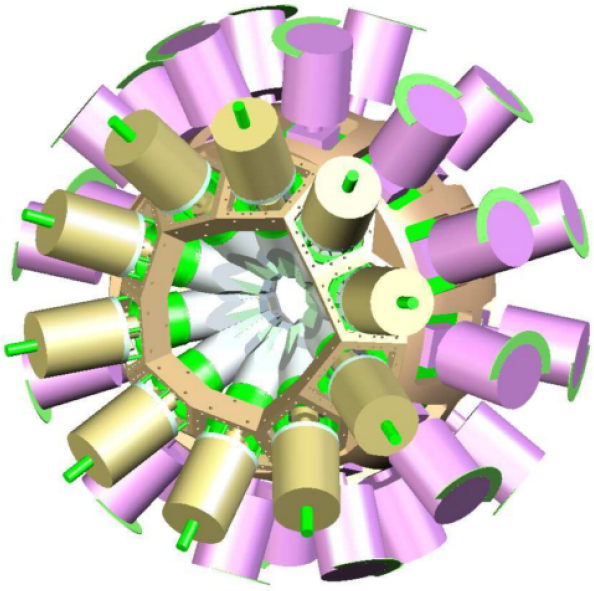

Figure 3.2: The JUROGAM II array, purple dewars indicate Clover detectors, the golden dewars, Phase I's. At the front the hexagonal gap can be seen where the 5 Phase I detectors have been removed to make space for the solenoidal magnet.

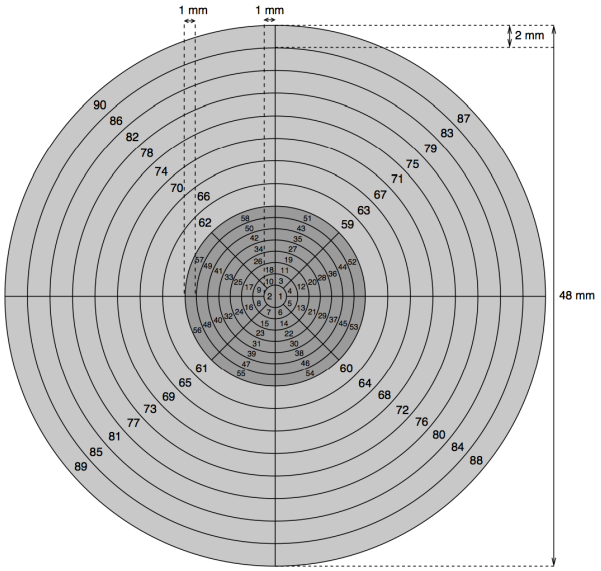

Figure 3.3: Schematic drawing of the SAGE silicon detector showing the arrangement of the pixels.

3.1.2 SAGE silicon Detector

The SAGE silicon detector is a highly segmented detector made up of 90 pixels. The detector is 48 mm in diameter with a thickness of 1 mm. Figure 3.3 shows the arrangement of the pixels along with dimensions and the numbering scheme used.

3.1.3 SAGE Solenoidal Magnet and High Voltage Barrier

The SAGE solenoidal magnet consists of three separate solenoids, two upstream of the target position and a third downstream. The upstream solenoids are at an angle of 3.2° to the beam axis, whilst the downstream solenoid is on the beam axis. This near-collinear geometry was chosen to minimise the

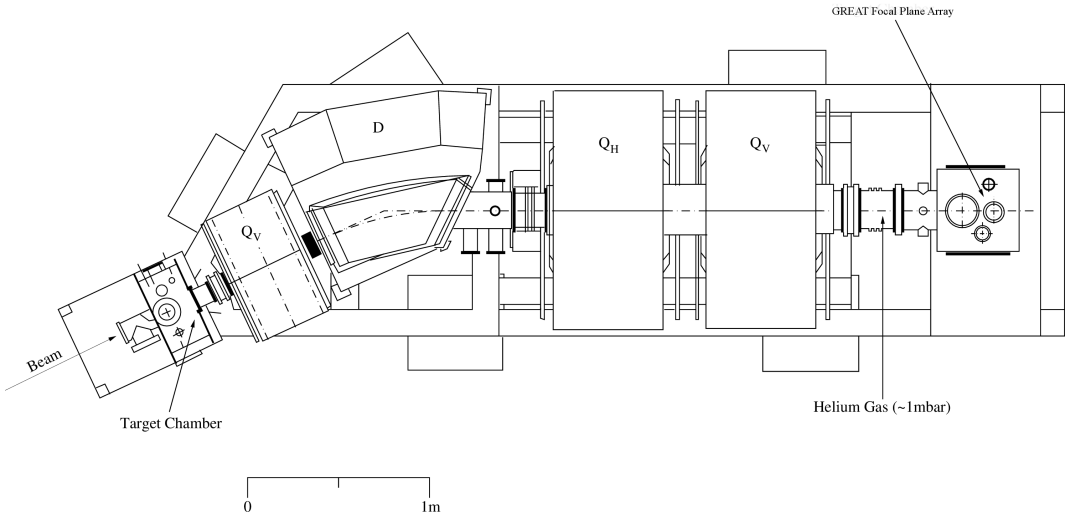

Figure 3.4: Schematic of the RITU gas filled separator.

Doppler broadening of the electron peaks, along with reducing the amount of delta electrons incident of the detector, which are emitted with a heavy forward focus. The solenoid magnets transport electrons from the target position to the detector, which is positioned upstream just off beam axis and at a distance of $\sim$95 cm. Further to the solenoidal magnet, there is a high voltage barrier in position between the target and the detector. When a negative voltage is applied to this, it has the effect of suppressing the transmission of low energy electrons, further reducing the background from delta electrons.

3.2 RITU Gas-filled Recoil Separator

RITU is a gas-filled recoil separator [Lei95], consisting of three quadrupole magnets and one dipole magnet in a QDQQ configuration. This differs to the standard configuration of DQQ, by the addition of an extra vertically focussing quadrupole which provides increased acceptance to the dipole. Fig-

ure 3.4 shows a schematic plan of the RITU gas filled separator, showing the target chamber, the four magnets, and the GREAT focal plane array.

3.3 GREAT Focal Plane Array

The GREAT Focal Plane Array [Pag03], is a combination of silicon, germanium, and gas detectors, for detecting the arrival and subsequent decay of reaction products. It is sensitive to α particles, β particles, γ rays, X-rays, as well as electrons from processes such as internal conversion and β decay. GREAT consists of a number of separate detector systems that will be expanded upon in the following subsections. At the entrance to GREAT is the multi-wire proportional counter (MWPC), next are the dual-sided silicon strip detectors (DSSDs), 11.4 mm behind this is the planar detector. In a box configuration around the DSSDs are the PIN diodes. Originally behind, but now above this, is the GREAT Clover detector, further to this another two fourfold segmented Clover detectors are placed either side. Figure 3.5 shows a schematic view of the GREAT focal plane spectrometer. Visible are the DSSD, PIN diodes, planar and the GREAT clover. Not shown are the MWPC and the additional two Clover detectors.

3.3.1 Multi-wire proportional counter

The MWPC, is positioned at the entrance of GREAT. All products passing through RITU to the focal plane, pass through it, allowing for identification based on energy loss in the gas along with time of flight in conjunction with the DSSD. The aperture of the MWPC is 131x50 mm with a vertical 1 mm

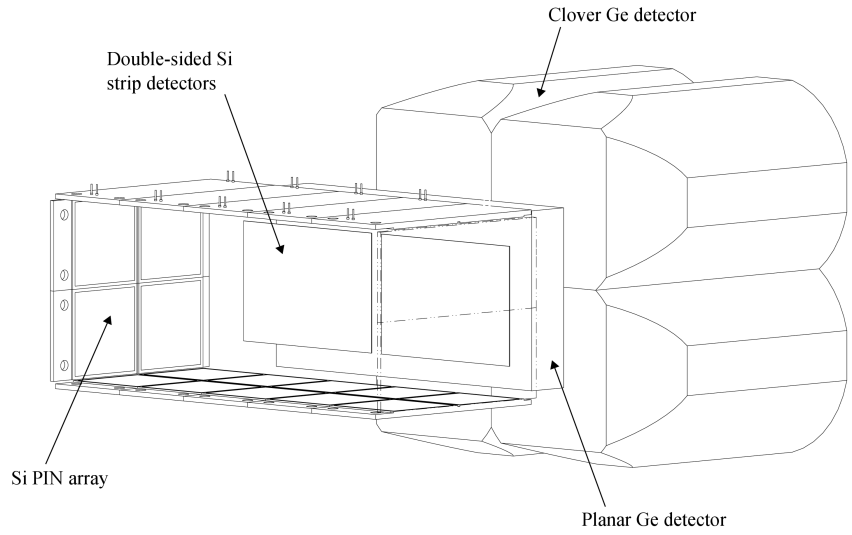

Figure 3.5: Schematic of the GREAT Focal Plane Array [Pag03].

wide strut in the centre to support the thin mylar foils, used as the anode, with the wires acting as the cathode. The MWPC is filled with isobutane gas, this facilitates a small amount of energy loss by particles passing through it. Particles can then be differentiated depending on their energy loss. This ability to identify recoils passing through the MWPC allows for distinction between these and their subsequent radioactive decays.

3.3.2 Double-sided Silicon Strip detectors

The DSSDs, are the implantation detectors, each DSSD is 60 × 40 mm in size with a thickness of 300 μm, with a strip width of 1 mm. Two of these DSSDs are placed adjacent to each other, giving a total of 120 vertical strips

on one side and 40 horizontal strips on the other, giving a total of 4800 pixels. The two DSSDs are mounted 4 mm apart on a hollow block through which coolant is circulated, cooling the DSSDs to -20°C. The detection efficiency for recoils is ∼85%. Further to detecting recoils with a high efficiency the DSSDs can detect α particles with an efficiency of ∼50% and conversion-electrons depending on the gain settings used.

3.3.3 Planar detector

The planar detector is a double-sided germanium strip detector, for measuring low energy γ-rays and X-rays. The detector has an active area of 120 × 60 mm and a thickness of 15 mm. The width of the strips on both sides is 5 mm. The efficiency of the Planar detector, along with the Clover detectors is shown in Figure 3.6. These efficiencies are based on the GEANT4 simulation from Andreyev *et al.* [And04].

3.3.4 Silicon PIN photodiode detectors

An array of 28 silicon PIN photodiode detectors are mounted in a box arrangement around the DSSDs, in the backwards direction relative to the beam direction. Each of these PINs has an area of 28 × 28 mm and a thickness of 500 μm. This arrangement has an efficiency of ∼20% [And04].

3.3.5 Clover detectors

The GREAT clover detector is made up of four crystals, each with a diameter of 70 mm and a length of 105 mm. The first 30 mm of each crystal is

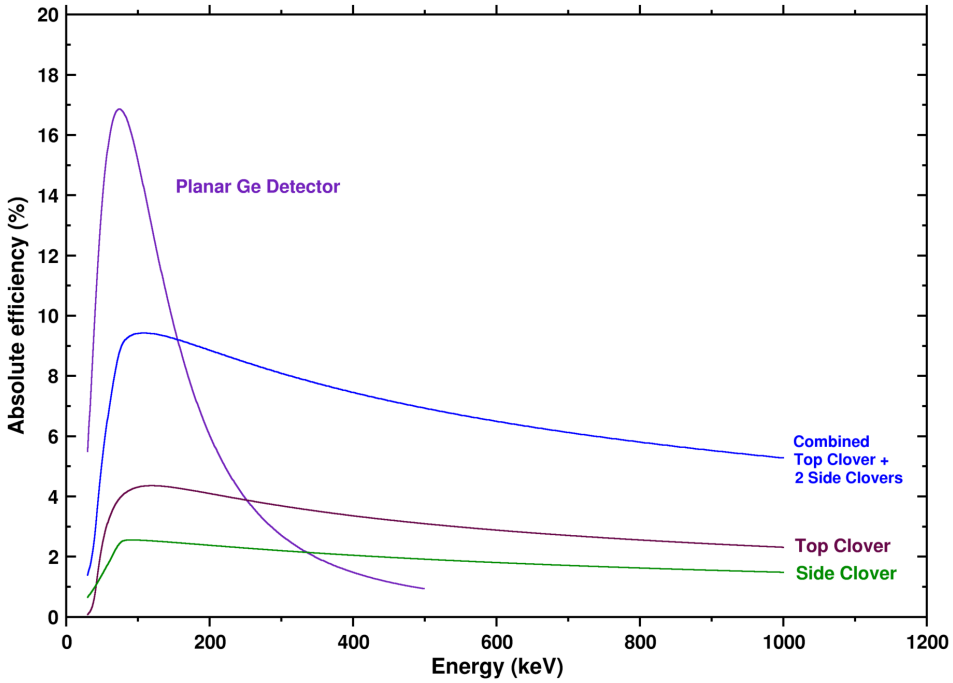

Figure 3.6: Efficiency curve for various components in the GREAT focal plane array - obtained from [GJ08].

also tapered by an angle of 15° on the outside surface. Each crystal has a further four fold segmentation. There is also a suppression shield of bismuth germanate crystals surrounding the detector to improve peak-to-total ratio. Further than the GREAT clover detector there are two more four fold segmented clover detectors placed to the left and right of the DSSDs.

Chapter 4

Simulation of the SAGE spectrometer in GEANT4

4.1 Justification of Simulation

As with any new detector setup, understanding its behaviour is a large part in analysing any experiment performed with it. A comprehensive simulation not only allows better understanding of the performance of the setup, but can be used as a tool to help in the tuning of such things as the electromagnetic fields with the aim of increasing electron transmission efficiency.

During the design and construction phase of the SAGE spectrometer, simulations were carried out using the SOLENOID code [But96]. These simulations were limited to two dimensions with cylindrical symmetry and focussed only on electron transport. The SOLENOID code did have the ability to specify an angle between the beam axis and the field axis, but not the angle between the magnets themselves, which result in a non-cylindrically

symmetric field.

GEANT4 [Ago03] is a toolkit for the simulation of the passage of particles through matter. It has a large range of functionality including reproduction of complex geometry and materials alongside detailed physics models for the interactions of particles with matter over a wide range of energies. The toolkit is implemented in the object-oriented programming language C++ and has been used in a wide range of applications in fields such as high energy physics, nuclear physics, space engineering and medical physics.

A GEANT4 simulation overcomes the restrictions of the previous simulation by being fully three dimensional and can also be expanded to include the JUROGAM II array. This allows for a more realistic simulation and a more detailed view of electron motion within SAGE and the volumes where electrons are being lost [Pap12, Cox13].

4.2 Construction of the Geometry

The accuracy to which the geometry is reproduced is of great importance for the usefulness of the simulation. Figure 4.1 shows the simulated geometry.

The Phase I and Clover Ge detectors have been reproduced from design specifications, including the bore hole, Li contacts, Ge crystals, BGO crystals, Heavymet collimators, and supports. Figure 4.2 shows a cross section view through two Clover and one Phase I Ge detectors.

Figure 4.3 shows the comparison between the simulated Si detector and the real detector. In the left image, visible as black lines, the inactive areas between pixels can be seen. Between each pixel there are 70 μm wide inactive

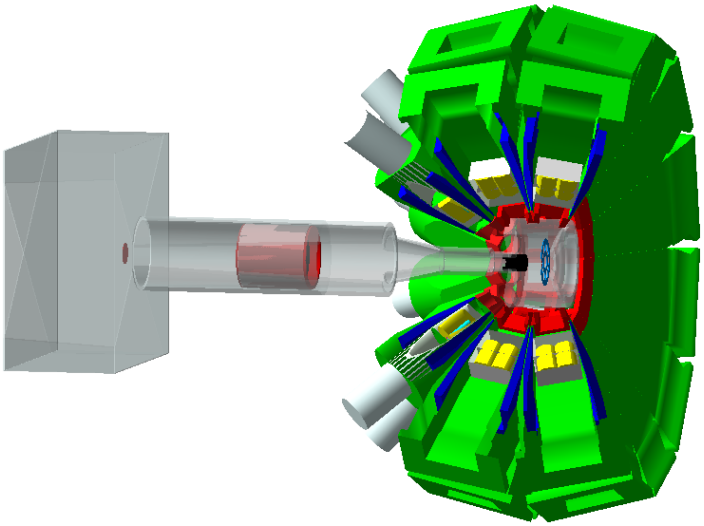

Figure 4.1: Complete Simulation of SAGE spectrometer, with the SAGE silicon detector to the left and JUROGAM II array to the right.

strips. This leads to a total inactive area of around 4%. For more in depth discussion on the SAGE silicon detector see [Pap10].

Figure 4.4 shows a comparison between the simulated high voltage barrier and the real one. The real high voltage barrier did not have the horseshoe connector, which is used to charge the high voltage barrier, fitted in this photo, but it is shown in the simulation.

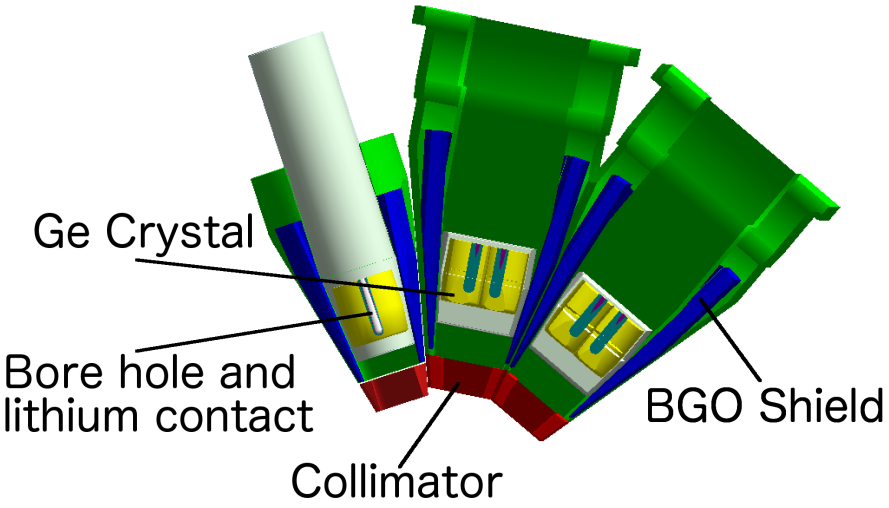

Figure 4.2: Cross section view of two Clover(centre, right) and one Phase I (left) Ge detectors.

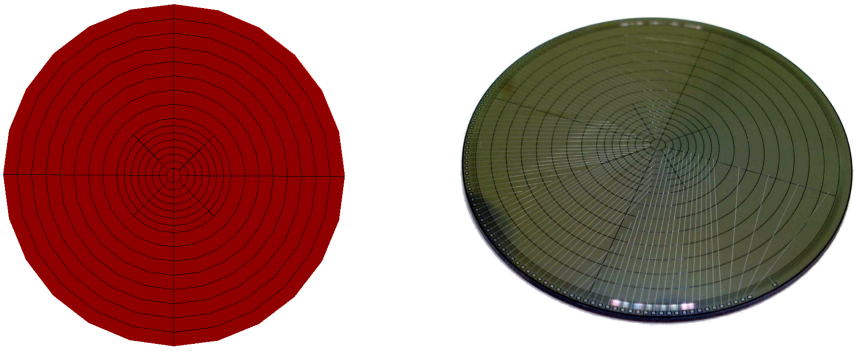

Figure 4.3: Comparison of simulated and real Si detectors.

Figure 4.4: Comparison of simulated and real high voltage barriers, note the horseshoe is not shown in real image.

4.3 Analysis of Simulation Data

The ROOT data analysis framework [Bru97] has been used for the extraction and analysis of data from the simulation. Within the simulation a ROOT tree is built containing relevant details about each event. These details are mainly focussed on the values that are measurable in the real setup, namely the energy deposition within detectors, but also include quantities that cannot be measured such as,

- initial energies of particles
- initial momentum vector, for analysis of angular emission
- energy deposition in non-detector volumes, e.g. target wheel. This allows for in depth analysis of where efficiency losses occur, see section 4.5
- information of particles generation, i.e. primary particle, secondary particle generated from some physical process such as pair-production.

Once this ROOT tree has been generated all subsequent analysis can be performed afterwards with the use of ROOT codes much faster than running the simulation. This is done as the tracking of several million electrons in electromagnetic fields can take many hours, whereas generating a histogram filled with the electrons detected in a certain volume, such as a single pixel from a ROOT tree can be done in a fraction of the time. By this method

techniques such as Compton suppression and add-back can be implemented also.

4.4 Tuning electromagnetic fields

GEANT4 has a number of models to describe charged-particle motion in an electromagnetic field depending on the kind of motion, the accuracy of simulation needed and the type of field in question. Further to this there are a number of parameters used to describe the required accuracy of the particle motion in a given field. Here there is a trade-off between the accuracy of the simulation and the speed at which it can be performed. The initial simulation and generation of the electromagnetic field map was performed using the OPERA simulation package [Fie07]. This simulation was performed to an accuracy of 1 cm in a 3D grid setup. The field map used covered an area of 30 cm $\times$ 30 cm $\times$ 150 cm containing all volumes that electrons could be located within. More details on the field simulations can be found in [Pap10]. This meant that the field did not extend for the full simulation, rather only where the electrons of interest are likely to be affected by it. Further to this, outside of the vacuum, where the Ge detectors are located, necessarily had to be a low field region as the Ge detectors are highly sensitive to electromagnetic fields. To this end, a large number of shielding configurations were tested, in simulations before construction, with the final setup, and finally in GEANT4. Figure 4.5 shows a schematic view of the final shielding configuration.

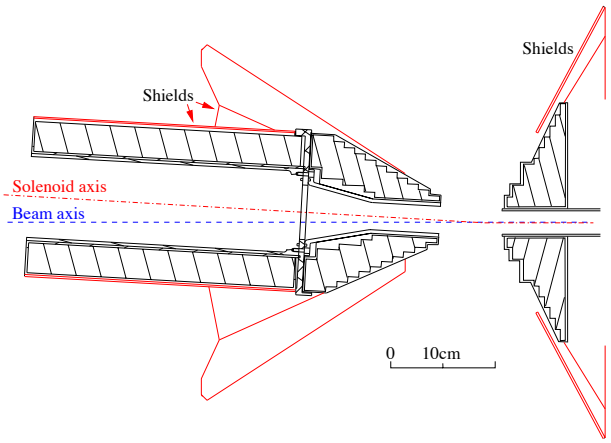

Figure 4.5: Schematic view of the magnetic coils and shielding within SAGE.

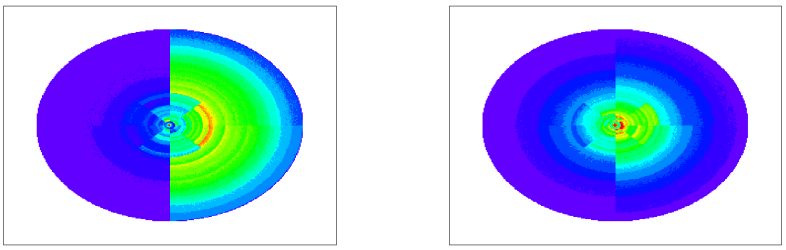

Figure 4.6: Comparison of electron distribution for original detector position (left) and detector moved by 10 mm towards the beam axis (right).

Initially the effect of the 3.2° angle between the upstream and downstream coils, as can bee seen in Figure 4.5, was underestimated. This caused the focus of the electrons to be off centre on the detector. This was reproduced in GEANT4, as can be seen in Figure 4.6 where the initial distribution and the final distribution of electrons can be seen.

The electron distribution is of great importance since the maximum SAGE silicon detector count rate is a major limiting factor to the maximum beam

intensity. To this end, the size and arrangement of the pixels within SAGE was chosen with the aim of giving an even count-rate across the whole detector, with central, smaller pixels experiencing a higher intensity than outer, larger pixels, which in turn detect more electrons due to their size.

The smallest aperture that electrons pass through in the SAGE spectrometer is the carbon foil unit, which is necessary for separating the high vacuum needed for operation of the high voltage barrier from the He gas used in RITU, which has an inner diameter of 31 mm. The field map has been interpolated from a $1\,\mathrm{cm}^3$ grid. From this scale it can be seen that using greater than millimetre accuracy would not give a gain in accuracy and would only increase the time taken for the simulation considerably.

In GEANT4 the motion of a charged particle in an electromagnetic field is tracked by integration of it's equation of motion. This is done using a Runge-Kutta method, there are other methods for specific types of fields depending on their level of uniformity and whether they are wholly magnetic in nature. The integration method is described by the stepper in GEANT4. [1]

A number of parameters are used to describe how accurately the path of a particle is tracked in GEANT4. A curved path of motion is broken down into a series of linear chord segments, of length set by the user, that closely approximate the curved path. The distance of closest approach between a volume boundary and a linear chord segment is known as the miss distance or chord distance. If this chord distance is below a certain value, again set by

[1] The 4CashKarpRKF45 stepper was chosen for the best balance between reproduction of realistic motion and speed of simulation.

the user, the path of motion will be recalculated with shorter steps, limited in size by another parameter, to see if the particle will cross the boundary. At which point if the particle is found to cross the boundary the interaction will be calculated. These various parameters were all set to a value of 1 mm due to the accuracy of geometry and field values, anything greater than this would increase significantly the computational time required without meaningful change to accuracy.

4.5 Detection Efficiency

The most important aspect of the simulation is the accuracy with which it reproduces the real experimental efficiency. For the real detector ^{133}Ba and ^{209}Bi are used for calibration as these give a spread of electron energies up to $\sim$1 MeV, see Section 5.1 for more on calibration of the SAGE silicon detector. With the simulation, it is a simple task to generate a given number of electrons with a definite energy. For a detailed analysis of the detection efficiency electrons are generated with energy divisions of 10 keV from 10 to 1000 keV. Through the use of ROOT, electrons with a given initial energy can then be selected. As can be seen from Figure 4.7 electrons with initially identical energies will lose varying amounts whilst being transported to the detector. This can be caused by energy loss in the carbon foils for instance.

Figure 4.7 shows all electrons detected for an initial energy of 100 keV. Of these a significant fraction have lost a large amount of their initial energy. The specific structure of this peak can be explained by the source geometry used. To best match the real data points, the ^{133}Ba source geometry was re-

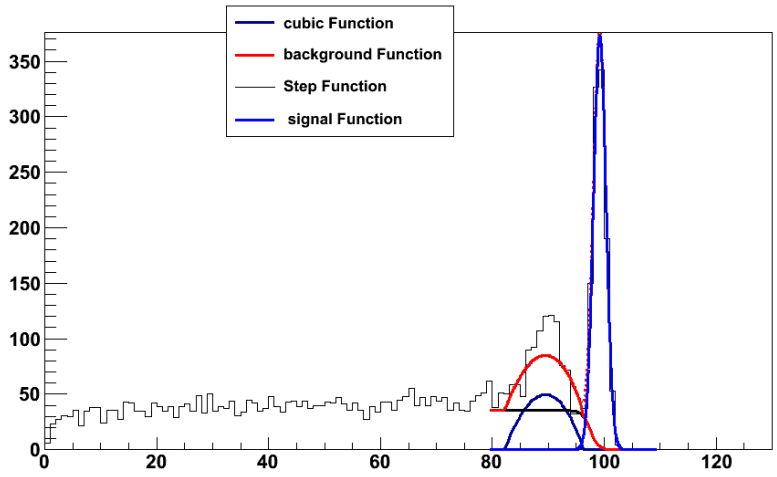

Figure 4.7: Simulated electrons in the SAGE silicon detector with an initial energy of 100 keV.

produced. This consists of a thin mylar window on the face pointing towards the detector and a thicker acrylic backing pointing away. Electrons emitted towards the detector lose a small amount of energy exiting the source and are found in the main peak, electrons emitted at a backwards angle which are reflected by the magnetic field lose a larger amount of energy and make up the second lower energy peak. If only the number of electrons detected was taken as a measure of the efficiency, it would be a great overestimation, and in a realistic case where there would be more than one energy peak and it would not be possible. Ideally all the electrons in the peak would be counted and those that would be considered background if it were real data would be discounted. To achieve this a fitting algorithm was developed combining a Crystal Ball Function [Gai82] to fit the peak with a combination of a quadratic and a step function to fit the background. It can be seen that the blue line is a good match to the full energy deposition peak. The solid red

line shows the combined step function and the quadratic. This is close to what would be expected for fitting a real peak with this kind of background.

The need for this background subtraction diminishes as the energy of the emitted electron increases, and is required even less for γ rays, but for consistency purposes all fits are done using the same algorithm.

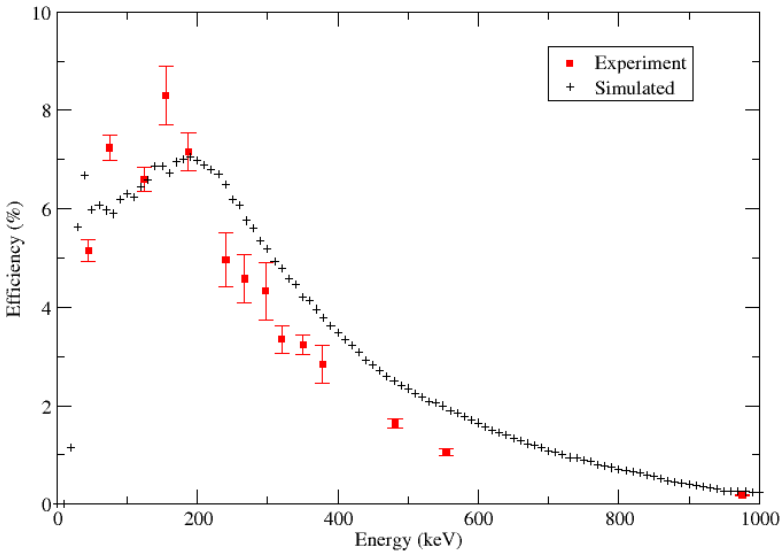

Figure 4.8: Simulated efficiency curve for the SAGE silicon detector compared to measured values for peaks in ^{133}Ba and ^{207}Bi.

Figure 4.8 shows a simulated efficiency curve for electrons of energies from 0 to 1000 keV. It can be seen that for energies below 200 keV this simulation underestimates the electron efficiency, but for higher energies there is a good agreement. The source of this discrepancy is not yet understood and it may be due to missing geometry as detailed in Section 4.9 or to some other reason.

Figure 4.9 details the efficiency as a function of high voltage barrier set-

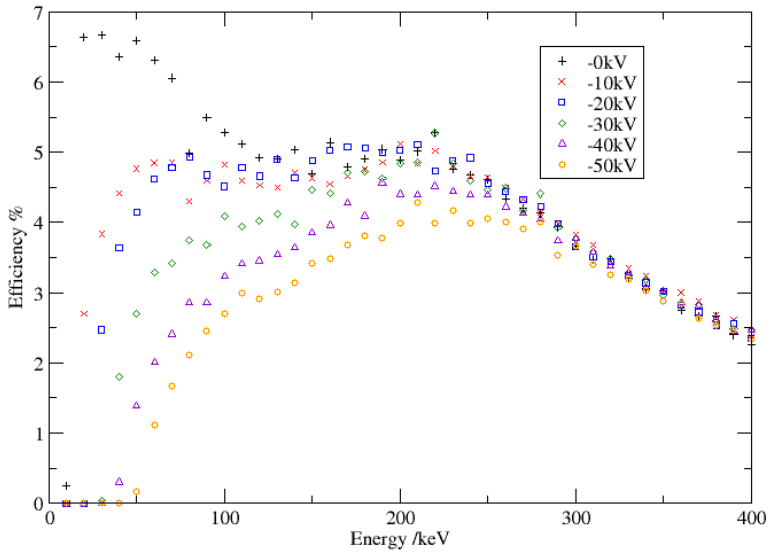

Figure 4.9: Simulated SAGE silicon detector efficiency as a function of high-voltage barrier setting.

ting. It can be seen that the efficiency below 200 keV is affected by the high-voltage barrier settings. The effect of the high-voltage barrier is predictable and proportionate to the barrier setting.

Figure 4.10 shows a comparison of simulated and measured efficiency for a barrier setting of -30kV. Here it can be seen that there is a good agreement with measured efficiency for energies above 200 keV, below this there is still some difference between simulation and measured values, though from 50 keV downwards there is once again good agreement between simulation of measurement.

Alongside the detection efficiency of electrons with the SAGE silicon detector the detection efficiency for γ rays with the Jurogam II array is an

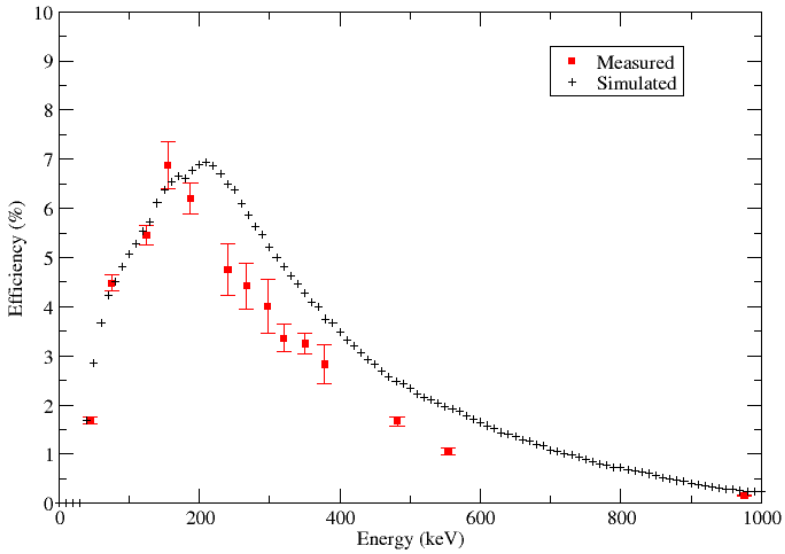

Figure 4.10: Comparison of measured and simulated SAGE silicon detector efficiency for a high voltage barrier setting of -30kV.

important part of this simulation. Figure 4.11 shows a comparison of simulated and measured efficiency for the JUROGAM II array. It can be seen that there is a very good agreement in shape between simulation and measured efficiency, though in the simulation the efficiency is between 1-2 % higher at all points. The reason for this is likely to do with a combination of geometry not yet included in the simulation, namely the aluminium holder the target wheel sits in, the motor used to rotate the wheel and tin and copper absorber foils on the faces of the Phase I and Clover detectors, and inaccuracies in crystal size and position. Though the effect seems too pronounced for such a small amount of missing geometry to be the only cause. One further affect on low energy efficiency for both silicon and germanium detectors

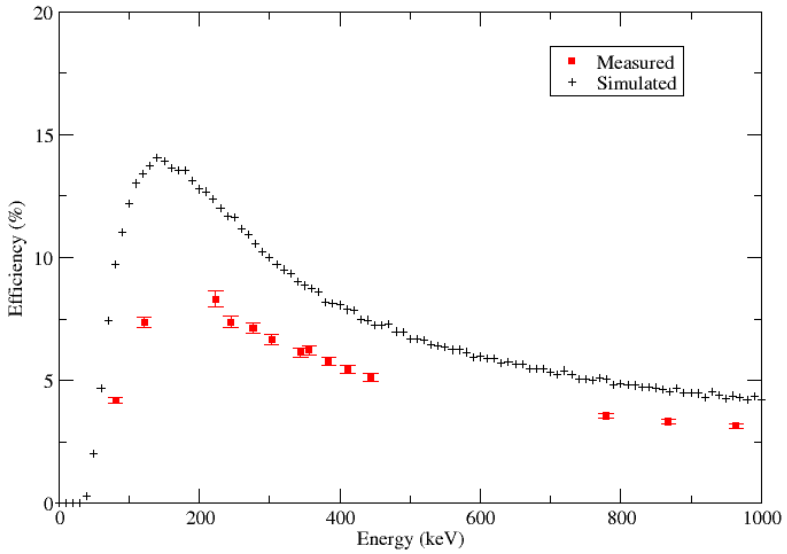

Figure 4.11: Simulated efficiency of the Jurogam II array also shown in blue is a calculated efficiency curve.

that has not been taken into account is the effect of low energy noise. For real detectors a threshold signal limit has to be set to stop excessively high count rates. The effect this has on low energy efficiency could account for the discrepancies seen here.

4.5.1 Efficiency Losses

The SAGE spectrometer has a number of apertures between the target position and the silicon detector, through which electrons must pass. This is illustrated in Figure 4.12. Table 4.1 details the volumes that electrons deposit energy in.

Along with the narrowest of the apertures, the carbon foil unit, there is

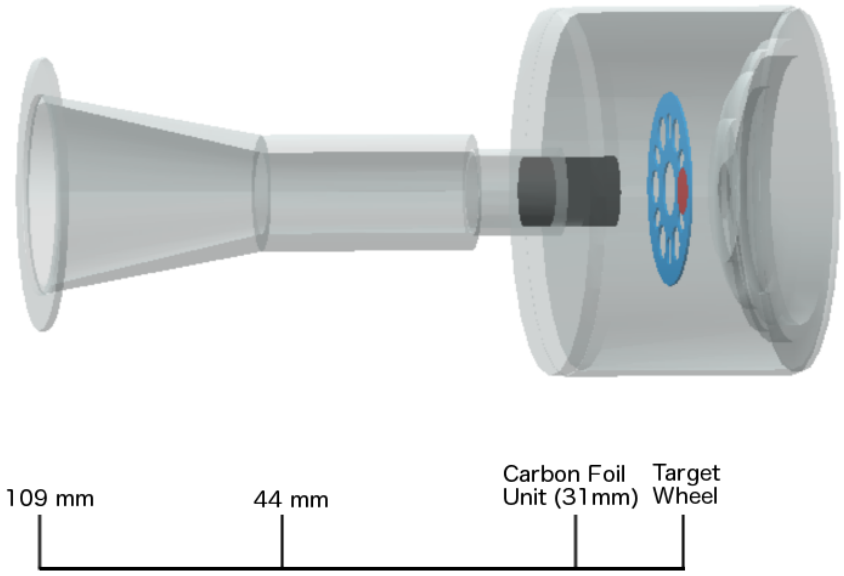

Figure 4.12: Simulation detailing the geometry near to the target position in SAGE, visible are the carbon foil unit, target wheel, target, and the detector chamber.

the target wheel, shown in Figure 4.12, that are the main volumes for absorbing electrons. The target also shows a very high number of interactions, though it should be noted that these are generally of a very small energy and most electrons that interact here will go on to deposit most of their energy in either the target wheel, carbon foil unit, or detector. Inversely, the target chamber, detector chamber, and high-voltage barrier all account for a very small number of electrons.

Volume Name	Electron Interactions
Detector	81000
Carbon Foil Unit	105000
Target	908000
Target Wheel	326000
Target Chamber	2300
Detector Chamber	0
High-Voltage Barrier	7

Table 4.1: Number of electrons from one million generated at 100 keV interacting with different parts of the geometry, rounded to the nearest thousand. For the detector, only full energy deposits are considered, for all other volumes any energy deposit is counted. Note that an electron can deposit energy in multiple elements.

4.6 Sensitivity to delayed electron emission

One potentially interesting use for SAGE is the detection of delayed electron emissions, an example of this is ^{177}Au, which is believed to have have an isomer with a lifetime less than 17 ns [Kon01]. In the time this isomer takes to decay, the recoiling nucleus will have travelled a number of centimetres downstream towards RITU. This makes the detection of γ rays difficult owing to shadowing effect of the JUROGAM II array, whereby, any γ rays emitted after the recoiling nucleus has left the target chamber would have to pass through a significantly larger amount of material to be detected as they would have to enter the germanium detectors side on.

Due to the magnetic field arrangement of SAGE however, conversion electrons of transitions such as this could still be transported to the silicon detector by the solenoid coils. Simulations suggest that not only could this be possible but the higher magnetic field region downstream could improve the focussing of the electrons and increase the detection efficiency in this

case.

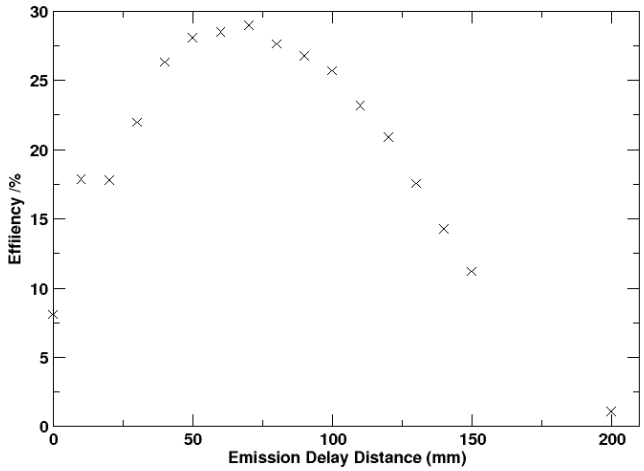

Figure 4.13: Detection efficiency as a function of distance downstream of the target position for emission of electrons of energy 100 keV.

In Figure 4.13 the detection efficiency is shown as a function of the distance downstream of the target position that the electron is emitted. It can be seen that the efficiency increases through to around 70 mm, and then tails off as the distance increases. This effect opens up the exciting possibility that short lived isomers (with lifetimes of a few ns) can be detected near to the target position via the emitted electrons. This is especially fortunate as transitions out of isomeric states often have high multipolarity and therefore ought to be highly converted.

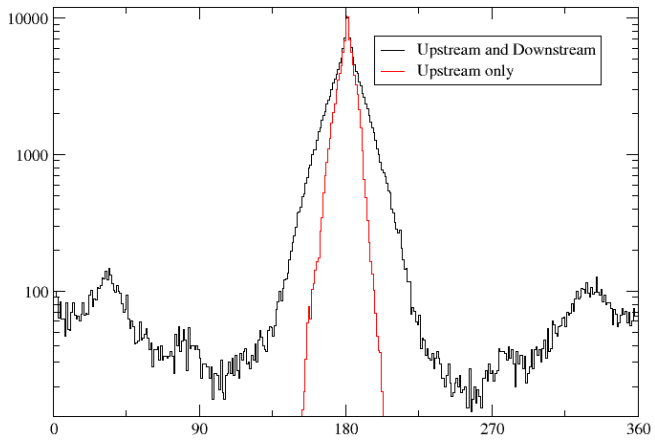

Figure 4.14: Electrons detected as a function of emission angle.

4.7 Emission angle of electrons

Figure 4.14 shows the electrons detected as a function of their initial emission angle in the horizontal plane with 0° being emission directly forward. The black line shows electrons detected for a solenoid current of 800A in both upstream and downstream coils. The highest detection is for electrons that are emitted with an angle of 180°. It can also be seen that there are secondary peaks at 35° and 325° these can be explained as electrons being reflected by the downstream coil. Shown in red is the electrons detected for a solenoid current of 800A in only the upstream coils. It is clear that without the downstream coil there is no reflection of electrons and so only electrons emitted at backwards angles are detected. It should also be noted that for when using all the coils the number of electrons detected is approximately 168,000, whereas for only the upstream coils 77,000 electrons are detected.

4.8 New data format for simulation of experiments

GEANT4 has in-built methods of producing radioactive decays though there are a number of problems with the methods. Firstly there have been inconsistencies with internal conversion electron emission. Secondly there is only support for nuclei of Z<100. Finally, even for the nuclei that can currently be simulated, if one were to change a decay in some way, for testing new levels or altering level schemes for instance, this would require editing within the source code of GEANT4.

Fortunately GEANT4 is highly versatile when it comes to generation of particles, so it possible to write a class to generate decays by reading in the relevant information from text files.

A new primary generator action was written that can more completely simulate the radioactive decay of nuclei such as ^{255}Lr. This primary generator action requires three files to simulate the decay, these are a level scheme file, an ICC file, and an intensity file. See Tables 4.2, 4.3 and 4.4 for examples.

The level scheme file follows the format of the ENDSF data format, with the hopes of later expansion to allow more complex decays to be simulated. Table 4.2 shows an example level file for a test nucleus. In this nucleus it can be seen that there are 11 levels linked by 10 E2 transitions. Within this file a number of relevant values are also read into the simulation. There is a line at the start of the level scheme file that has the following structure;
L T K L1 L2 L3 M1 M2 M3 M4 M5 N O P Q. Where L and T refer to the number of levels and transitions respectively and K through to Q are the

binding energies of the simulated nucleus.

The ICC file is created using BrIcc [Kib08], this includes the internal conversion coefficients for K through to Q conversion and all their associated subshells, a script then extracts the relevant numbers to a more readable format shown in Table 4.3. Table 4.3 shows the conversion coefficients for each shell up to Q and each subshell in the case of L and M. The reason for including subshells for L and M conversion is that the energy difference between these is larger than the resolution of SAGE and so, for example an L1 and an L3 electron, in ^{255}Lr are separated by 7 keV and can be differentiated. For N conversion or higher the differences are so small, $<$1 keV, that they are indistinguishable.

The intensity file is generated from the conversion coefficients in the ICC file and another file detailing the γ-ray intensities of the transitions.

To accurately reproduce the intensities of transitions within the simulation, without knowing the initial populations of states is complex. The chosen approach is to compare the intensities for the given transitions. By comparison of the intensity of transitions into a state and out of a state, the amount of decays starting at each level can be inferred.

In the case detailed in Table 4.4 it can be seen that the first excited state has a total intensity of 1333, the next state has an intensity of 985, from this, it can be inferred that if there were 1681 transitions in total, 985 of them would begin in the second excited state and 348 would begin in the first excited state. This would reproduce the given intensities of 1333 and 985 respectively.

The level scheme detailed in Figure 4.15 is for a rotational band where

there is only one transition out of any given state. If there were to be two or more transitions from a state, as is the case with the strongly coupled rotational band simulated in Subsection 4.8.1, then based on the intensities of the two given transitions and by comparison to a randomly generated number, a transition is chosen. This process of choosing transitions will continue until the level energy, read in from the Level file, reaches zero.

4.8.1 Test nucleus simulation

Excited nuclei can decay through a large number of states through many different structures. Attempting to simulate any possible decay chain from any nucleus is a massive undertaking. The first goal was to simulate the individual structures, such as those seen in ^{255}Lr, see Section 6.6.

Shown in Figure 4.15 is an ideal rotational band. For the purposes of generating conversion coefficients, this nucleus has been set to have Z=103, the same as lawrencium.

Figure 4.16 shows the γ-ray and electron spectra generated from 1 million decays of this test nucleus. It is clear that even with this simple structure the electron spectrum is complex. This is one of the great difficulties of electron spectroscopy of superheavy elements. With lighter nuclei the spread in the subshells is smaller. For a transition of 100 keV being emitted from a nucleus of Z=50, the energy difference between an electron emitted from the L1 subshell and the L3 subshell is 0.53 keV, whereas for the same energy in Z=103 the difference is 7.73 keV. This leads to a larger number of resolvable peaks in the electron spectrum compared to the γ-ray spectrum.

The second structure seen in ^{255}Lr is a strongly coupled rotational band.

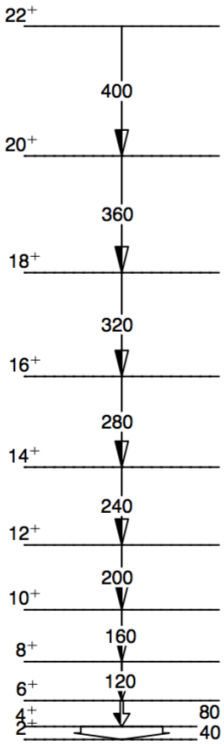

Figure 4.15: An example rotational band to be simulated.

An idealised case of this kind of structure is shown in Figure 4.17, in this the signature partner bands are well spaced and the differences in the γ-ray energies are all resolvable, in real life this is unlikely to be the case.

An important indicator of the state that such a coupled band structure is built on is the strength of the M1 transitions. For example in Figure 6.31 the difference in a strongly coupled band built on the $7/2^+$ [633] or the $7/2^-$ [514] states would look similar in the γ-ray spectrum but with the different M1 strengths at the bottom of the band, would be distinguishable with the use of SAGE.

This can been seen in Figures 4.18 and 4.19 where γ-ray spectra look

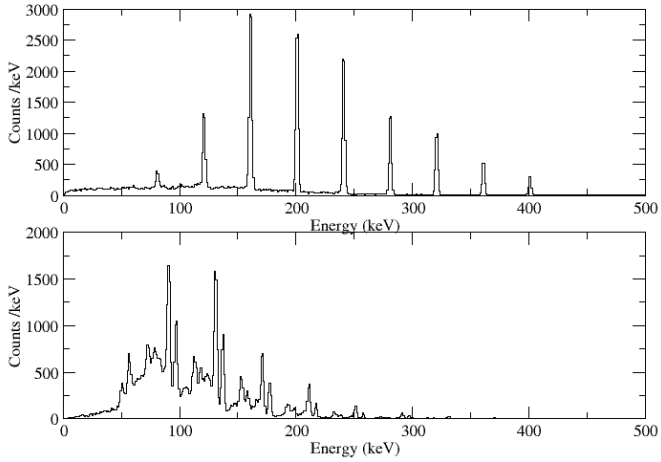

Figure 4.16: Upper:γ-ray spectrum, lower:electron spectrum produced by simulation of 1 million decays of level structure shown in Figure 4.15.

largely the same, and the differences are seen in the electrons. Here it can be seen that there are significantly more counts in the case of high M1 intensity. The L electrons of the transitions at 107 and 137keV are much stronger in the case of high M1 intensity, but are still weak in the γ-ray spectrum.

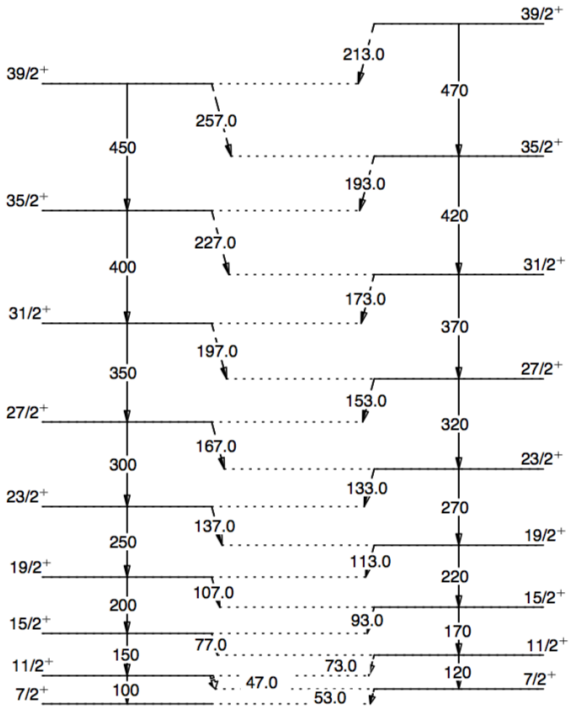

Figure 4.17: An example strongly coupled rotational band to be simulated.

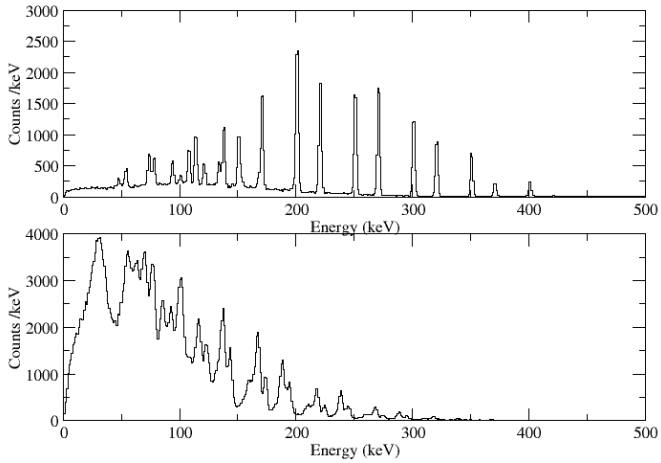

Figure 4.18: Upper γ-ray spectrum, lower electron spectrum produced by simulation of 1 million decays of level structure shown in Figure 4.17 with low intensity M1 transitions.

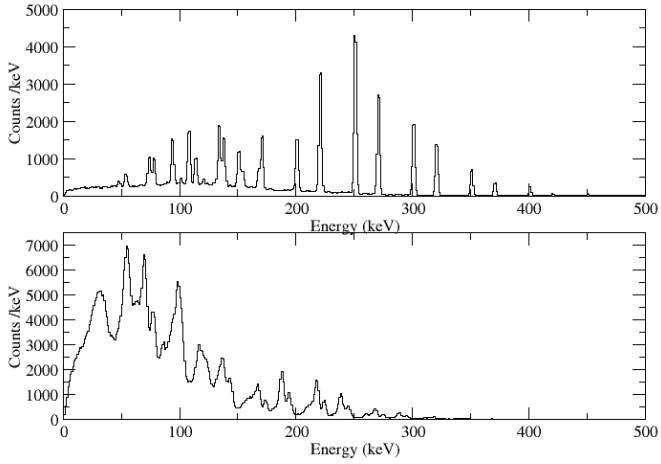

Figure 4.19: Upper γ-ray spectrum, lower electron spectrum produced by simulation of 1 million decays of level structure shown in Figure 4.17 with high intensity M1 transitions.

Type	Energy	Multipolarity
L	0.0	
L	40.0	
G	40.0	E2
L	120.0	
G	80.0	E2
L	240.0	
G	120.0	E2
L	400.0	
G	160.0	E2
L	600.0	
G	200.0	E2
L	840.0	
G	240.0	E2
L	1120.0	
G	280.0	E2
L	1440.0	
G	320.0	E2
L	1800.0	
G	360.0	E2
L	2200.0	
G	400.0	E2

Table 4.2: Example of level scheme file used for generation of radioactive decays. L and G denote whether an entry is for a level or a γ ray, respectively.

Subshell	Coefficient	Error
K	0	
L1	4.110E+01	5.754E-01
L2	1.052E+03	1.473E+01
L3	8.067E+02	1.129E+01
L-tot	1.900E+03	2.660E+01
M1	1.395E+01	1.954E-01
M2	2.961E+02	4.145E+00
M3	2.400E+02	3.360E+00
M4	4.144E+00	5.802E-02
M5	1.885E+00	2.639E-02
M-tot	5.560E+02	7.785E+00
N-tot	1.607E+02	2.250E+00
O-tot	4.165E+01	5.831E-01
P-tot	6.723E+00	9.412E-02
Q-tot	1.818E-02	2.546E-04
Tot	2.665E+03	3.731E+01

Table 4.3: Example of one transition in an ICC file used for generation of radioactive decays (E=40 keV, Z=103)

Energy	Total intensity
40.0	1333.0
80.0	985.3
120.0	799.0
160.0	419.5
200.0	270.4
240.0	148.1
280.0	119.4
320.0	65.9
360.0	48.9
400.0	11.6

Table 4.4: Example of Intensity file used for generation of radioactive decays.

4.9 Expansions to the current simulation

There are still a number of additions that could be made to the simulation to increase its accuracy. These will be briefly detailed here.

Currently the SAGE silicon detector is modelled at 90 pixels of silicon arranged as shown in Figure 3.3 with the inter-pixel inactive areas included. The dead layers on the front face of the detector have not yet been included into the simulation but will likely cause some slight change in the efficiency of the detector. Along with this the printed circuit board the detector is mounted on has not been simulated. With respect to the simulation of experimental data, the high flux of low energy delta electrons has not been reproduced. There are a number of approaches possible here, delta electrons can be generated by simulating the collision between a heavy ion and the target material. This would be a highly time intensive method owing to the large number of particles that would be generated and require subsequent tracking. A simpler approach would be to generate a statistical distribution of delta electrons that could then be added to any electron spectrum. Some combination of these with electrons being generated by a statistical approach and then tracked with GEANT4 would seem optimal, in terms of speed and preservation of coincidences in the data. Another aspect that is still missing from the simulated data are X-rays. A similar approach to that of delta electrons is likely best, with a statistical distribution of X-rays being produced and then tracked by GEANT4, though a more complex analysis may

be possible with the emitted electrons determining which X-rays are emitted. The reproduction of more complicated structures is also a future goal, following the relatively simple structures seen within ^{255}Lr combining these structures along with inter-band transitions, as detailed in Figure 6.28 would be very useful in understanding experimental data. After this reproducing more complex single-particle structures, such as those seen in ^{133}Ba for instance would be very useful in both better characterising the detector setup and from this more complicated nuclei could be simulated for comparison to experiment.

Finally there is another GEANT4 simulation for the detectors at the focal plane, as detailed in Section 3.3. It would be a very useful tool if this could be combined with the simulation detailed here. This would allow a much fuller simulation of entire experiments performed at JYFL.

Chapter 5

Analysis Techniques

The experiment to create and study ^{255}Lr was performed at the University of Jyväskylä in two parts, with a high intensity (110pnA) focal plane part to study α and isomeric decay, and a lower intensity (10pnA) part to study in-beam γ ray and conversion electron emission from excited states. The reaction used was ^{209}Bi(^{48}Ca,2n)^{255}Lr at a beam energy of 219(2) MeV. This section will detail a number of techniques used in the analysis of this experiment.

5.1 Calibration

Owing to the different sensitivities and energy ranges of the various detectors mentioned in Chapter 3, a number of methods were employed to calibrate these detectors. All calibrations were performed by fitting individual peaks in the software program TV [The93] to obtain the raw channel numbers for the centroid of the peaks. These centroids along with the given energies for the electrons and γ rays from [Fir99], were used to calculate the gain coefficients

using a gnuplot script.

5.1.1 Internal calibration of DSSD

Normally the DSSD would be calibrated using a triple-α source (^{239}Pu, ^{241}Am, ^{244}Cm), the energies of the α particles from these three elements are between 5-6 MeV, this is far away from the region of interest in this experiment, 8-8.5 MeV. It should also be noted that using an external source for calibration of the DSSD would result in a shifted energy spectrum, due to the dead layer on the detector. Owing to this and also the interest in studying the fine α structure it was decided that a calibration closer to the region of interest was needed.

Over the course of the experiment three different reactions were used for the purposes of calibration, these were, ^{164}Dy(^{48}Ca^{10+},5n)^{207}Rn, ^{208}Pb(^{48}Ca^{10+},2n)^{254}No, and ^{173}Yb(^{48}Ca^{10+},5n)^{216}Th. Using these reactions one side of the DSSD could be calibrated to be sensitive to α decays. The other side of the DSSD was calibrated using a ^{133}Ba source to be sensitive to electrons of energies up several hundred keV.

5.1.2 Calibration of silicon & germanium detectors

Calibration data was taken both before and after the experiment by placing the ^{152}Eu and ^{133}Ba sources of known intensity at both the target position and focal plane. The sources were used to obtain the efficiency the SAGE silicon detector and the JUROGAM II array.For the germanium detectors a number of peaks were used for the calibration with energies ranging from

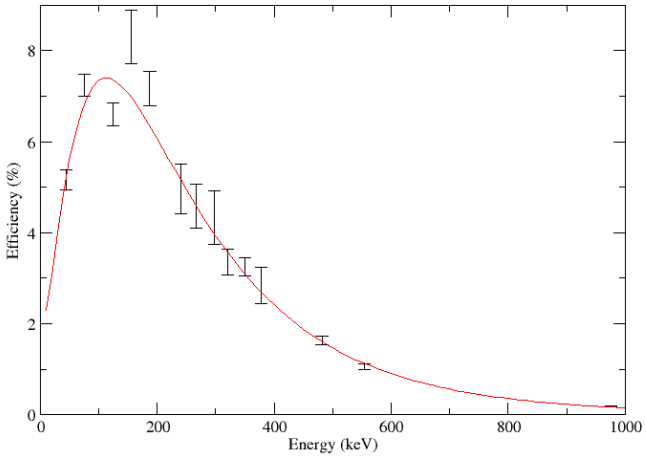

Figure 5.1: Relative efficiency curve for the SAGE silicon detector as a function of electron energy.

81 keV to 1408 keV. For the SAGE silicon detector, the electron sensitive side of the DSSD and the PIN diodes electron peaks between 75 keV and 350 keV from Ba were used. Owing to the energy response of the planar being suited to detection of lower energy γ rays, only the Ba source placed inside the GREAT vacuum chamber was used with peaks over the range 80 keV to 383 keV.

$$E_{fit} = exp[A + B(log(x/E_0) + C(log(x/E_0)^2 + D(log(x/E_0)^3 + E(log(x/E_0)^4] \tag{5.1}$$

Equation 5.1.2 was used to calculate the efficiency curve for the JUROGAM II array along with the SAGE silicon detector, Figures 5.2 and 5.1 show this curve fitted to data, with Table 5.1 detailing the coefficients in each case.

Figure 5.1 shows the efficiency response of the SAGE silicon detector as

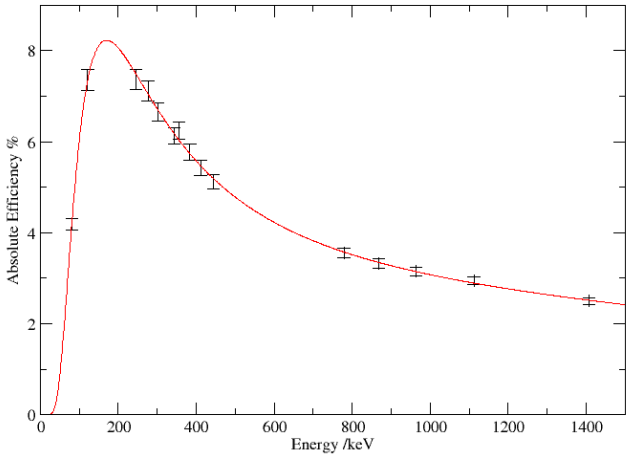

Figure 5.2: Absolute efficiency curve for the JUROGAM II array as a function of γ-ray energy.

a function of electron energy. Figure 5.2 shows the efficiency response of the JUROGAM II array as a function of γ-ray energy.

5.1.3 Doppler Correction

Recoiling nuclei are travelling at relatively high velocity. Due to this both γ rays and electrons that are emitted will undergo a Doppler shift according

Coefficient	JUROGAM II	SAGE
A	1.866	1.273
B	-0.627	-1.541
C	-0.201	-0.943
D	0.246	-0.128
E	-0.0779	0.00137
E_0	320*	320*

Table 5.1: Coefficients used for the fitting of the efficiency curve shown in Equation 5.1.2. Parameter denoted by * was held constant

to their emission angle, as described by Equation 5.2 [Kan04],

$$E = \frac{E' + m - \beta cos\theta' \sqrt{E'^2 + 2mE'}}{\sqrt{1 - (\frac{v}{c})^2}} - m, \tag{5.2}$$

where E is the energy of the particle when emitted in the rest frame of the recoil, E' is the detected energy, m is the mass of the particle, v is the velocity of the particle, c is the speed of light and θ is the angle of emission
For γ rays $m = 0$ and $v = c$, so Equation 5.2 simplifies to

$$E_\gamma = E(1 + \frac{v}{c} cos\theta). \tag{5.3}$$

For γ rays the emission angle is known from the detector angle, with the detectors in the JUROGAM II array being arranged in rings at the angles 76°, 105°, 133.6° and 157.6° relative to the beam direction. This means the detected energy, E_γ, can directly be converted to the unshifted energy, E, using Equation 5.3. In this experiment the recoil velocity was calculated to be 0.0186 c.

For electrons, this situation is more complicated. All information of emission angle is lost owing to being transported by the solenoidal magnetic field to the detector. This means that the unshifted energy of electrons cannot be calculated for every electron as is done for γ rays. An average emission angle for detected electrons can be found using the SOLENOID code. This allows an average Doppler shift correction to be applied to the electron energies. For example a 320 keV electron would be shifted up in energy to 325.6 keV by taking an average emission angle of 160°.

5.2 Data Acquisition

An efficient data acquisition with as little dead-time as possible is crucial to the studies such as this. To this end the Total Data Readout (TDR) triggerless data acquisition system has been developed [Laz01].

5.2.1 Total data readout

A major stumbling block for nuclear structure studies, especially those of isomeric decay studies, is the long dead time caused by conventional recoil decay tagging techniques because of long correlation times. TDR was developed to overcome the flaws of a common dead time data acquisition setup as has been used in the past. The idea behind TDR is that every detector channel is run independently and each data item is time stamped with a rate of 100 MHz, meaning a 10 ns precision on each data item. Using this method, events can then be reconstructed in software and the spatial and temporal constraints of the specific setup can then be used to define correlation of events.

5.2.2 GRAIN analysis system

To analyse the TDR data the GRAIN analysis system [Rah08] was developed. GRAIN's usefulness is threefold. Firstly it has the ability to form physically meaningful events from the data stream. Secondly it provides a relatively simple way for an "analysis code" to be applied to the data to extract results. Finally it gives the user a way to visualise the data in one and two dimensional histograms through its GUI.

5.2.3 Use of TUPLES for sorting data

In many experiments the amount of useful data compared to the total data is relatively low. This is especially true for experiments with lower cross sections, such as this one. Whilst analysis is ongoing there are many time consuming tasks, such as the optimisation of 1 and 2-dimensional gates. Often once a gate has been changed a subset of the data can be "resorted" to determine whether this new gate is an improvement. This iterative process is a time consuming one. In the case of low cross-section experiments, where sorting of most, if not all, of the data is required to determine any improvement, this can be an extremely time intensive process. This can be mitigated by the use of increased computer power but this is not always feasible and cannot be increased indefinitely.

Another possible approach is the use of TUPLES in the initial sorting of the data. A TUPLE is essentially an n-dimensional hypercube. Within this can be entered the various parameters often used for gating, such as time of flight, energy loss in the gas detector, and recoil energy, alongside relevant values such as energy deposited in JUROGAM II or SAGE on an event by event basis.

Using this method, a single sort of the data can be performed with very wide gates that only cut out noise but not relevant events. Then any gating conditions can be applied to these data without the need for resorting.

This method can reduce the time taken in optimising gating conditions in most situations. A secondary advantage of using this method is the rebinning of data without the need to resort. This is especially useful in cases such as

^{255}Lr where isomeric and α decaying states have significantly different half-lives.

Chapter 6

^{255}Lr Analysis Results and Discussion

As mentioned previously ^{255}Lr was produced in the fusion-evaporation reaction ^{209}Bi(^{48}Ca, $2n$)^{255}Lr. The study was performed in two separate runs in April 2011 and April 2012. The cross section for this reaction has been calculated to be of the order 200 nb.

The ^{48}Ca^{10+} ions were produced in the ECR ion source, then the ions were transported to the K130 cyclotron where they were accelerated to form a beam of energy 219(2) MeV. The target used for the first part of the experiment was a 450 μg/cm^2 ^{209}Bi at 99.8% enrichment, sandwiched with 10 μg/cm^2 (upstream) and 40 μg/cm^2 (downstream) carbon foils. The targets for the second part of the experiment were two self supporting ^{209}Bi targets of thickness 215 μg/cm^2 and 525 μg/cm^2, and a 300 μg/cm^2 ^{209}Bi with a carbon backing.

For the first part of the experiment only RITU and GREAT were used.

	JYFL 2011	JYFL 2012
Beam Time (days)	14	10
Average Beam intensity (pnA)	105	10
Number of α decays	11800	1170
Number of recoil-gated γ rays	-	7100
Number of recoil-gated conversion electrons	-	5300
Number of ^{255}Lr-tagged γ rays	-	990
Number of ^{255}Lr-tagged conversion electrons	-	770

Table 6.1: Experiment details.

In the second part of the experiment, RITU and the GREAT spectrometer were used in conjunction with the SAGE spectrometer. The high voltage barrier within SAGE was set to -38kV.

Table 6.1 details experimental yields of α decays, γ rays and electrons for both parts of the experiment.

6.1 Previous Work

Lawrencium was first observed in 1961 by Ghiorso *et al.* [Ghi61]. Lawrencium-255, along with several other lawrencium isotopes were first studied by Eskola *et al.* [Esk71] in 1971, where they measured one α decay of energy 8.37(2) MeV with a half-life of 22(5) s. This α decay is likely to be the 8.365(2) MeV, 31.1(13) s one later seen in [Cha06]. Owing to the significantly lower statistics and impurity in the first experiment, the other α decays would not have been seen.

More recently ^{255}Lr has been studied on a number of occasions, see [Cha06, Ket09, Hau08, Jep09]. Alpha spectroscopy was performed by Chatillon *et al.* [Cha06], isomeric decay studies were performed by Hauschild *et*

al. and Jeppesen *et al.* [Hau08, Jep09], whereas only Ketelhut *et al.* [Ket09] studied prompt γ-ray data in-beam.

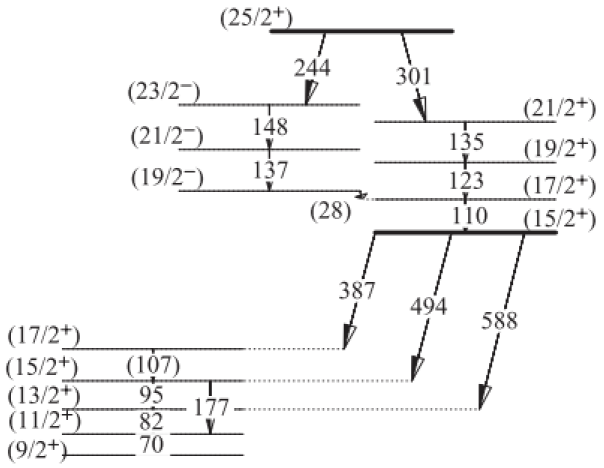

Figure 6.1: Level scheme taken from [Jep09].

Figure 6.1 shows a proposed level scheme from below the isomeric state at $(25/2^+)$ denoted by a bold line. Note there is a second proposed isomeric state at spin $(15/2^+)$.

Figure 6.2 shows a proposed α decay scheme from Chatillon *et al.* [Cha06], here 4 α decays are shown from two states in ^{255}Lr into 3 states in ^{251}Md.

Figure 6.3 details the results of the only in-beam study to date. The upper panel shows a recoil-gated γ-ray singles spectrum, the lower two panels detail summed coincidence spectra gating transitions believed to be from a rotational band and a second strongly coupled rotational band.

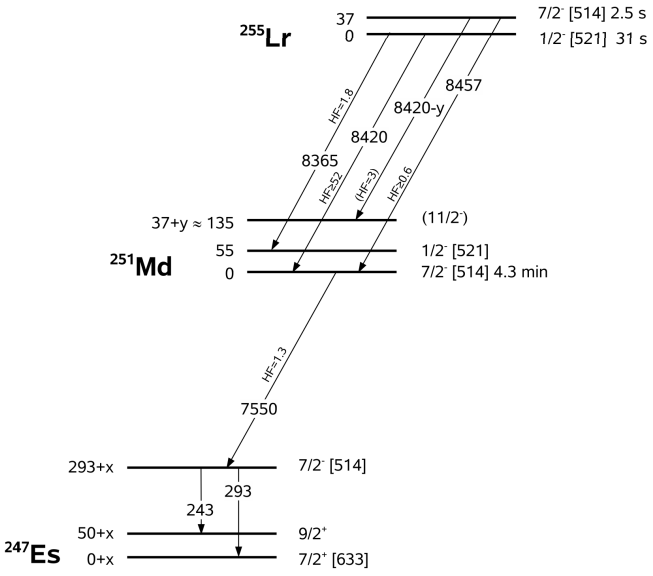

Figure 6.2: Alpha decay scheme taken from Chatillon *et al.* [Cha06]

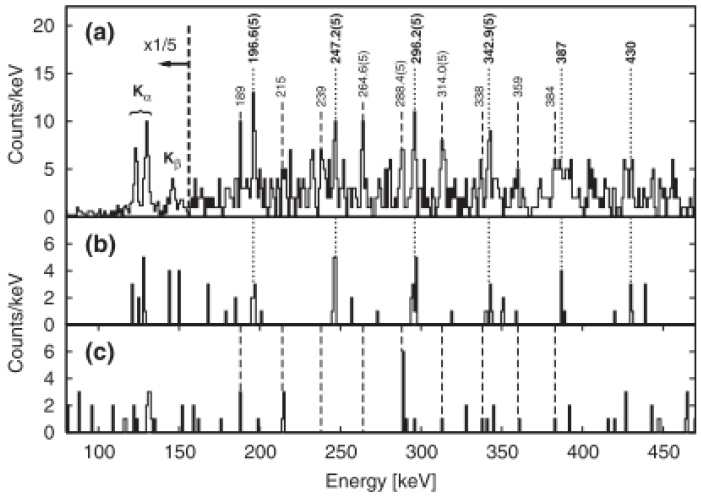

Figure 6.3: γ-ray spectra taken from Ketelhut *et al.* [Ket09], (a) Singles spectrum in delayed coincidence with recoil implantation (b) $\gamma-\gamma$ projection in coincidence with the sum of the gates of the transitions marked by dotted lines (c) same as (b) but for transitions marked with dashed lines.

6.2 Decay Spectroscopy

As mentioned in Chapter 5, the experiment was performed in two parts, the first part focussed solely on decay spectroscopy investigating the α decay and also the isomeric decay.

6.2.1 Alpha Spectroscopy

There are two strong α decaying states in ^{255}Lr, at energies of 8265(2) MeV and 8420(10) MeV. These states have half-lives of 31.3(1.3) s and 2.53(13) s and are from the ground state at spin $1/2^-$ and the excited state with spin $7/2^-$ [Cha06]. These can be seen in Figure 6.4 which shows, all events in the DSSD that are anti-coincident with a signal in the MWPC which would indicate an incoming recoil. Also visible is the α decay daughter of ^{255}Lr, ^{251}Md. There is also contamination from ^{255}No, and ^{215}Th left over from calibration.

The α spectrum can be significantly cleaned by the use of recoil decay tagging (RDT) whereby a recoil is required within the same pixel in the DSSD as the α decay within a time window of 100 s before the α particle gives the spectrum shown in Figure 6.5, alongside ^{255}Lr and ^{251}Md a small amount of the contaminant ^{255}No can be seen. This method can also be used to associate γ rays and conversion electrons with a specific recoil and decay.

When a further subsequent α decay is required, with the initial search time being 100 s and a larger time window of 900 s for a second α decay the

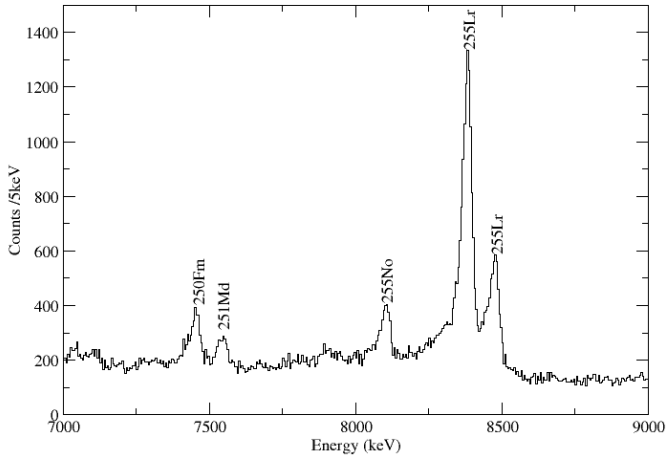

Figure 6.4: An α spectrum of ^{255}Lr, vetoed with the MWPC, visible are two peaks from ^{255}Lr, along with the α decay daughter, ^{251}Md and contamination from ^{255}No.

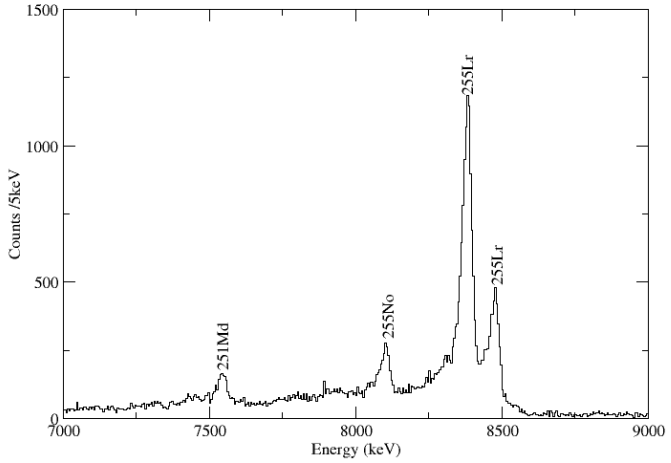

Figure 6.5: A recoil-decay correlated α-decay spectrum of ^{255}Lr, requiring the detection of a recoil nucleus in the 100 s prior to the α detection. Peaks from the daughter nucleus ^{251}Md and contaminant ^{255}No are also seen.

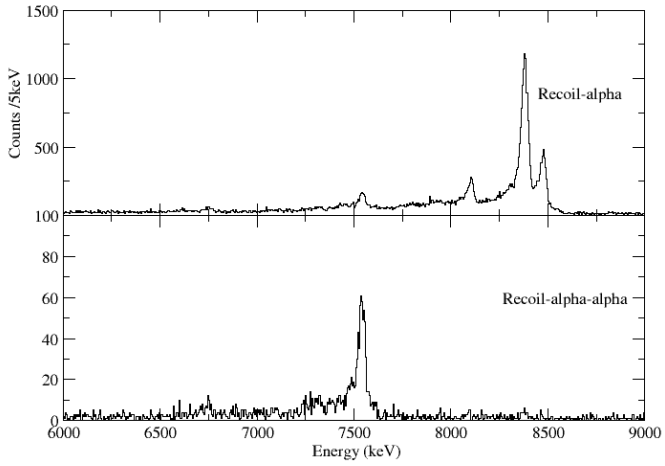

Figure 6.6: Upper, recoil-α correlated spectrum of ^{255}Lr with a correlation time of 100 s, lower recoil-α-α correlated spectrum showing the daughter ^{251}Md with a correlation time of 900 s.

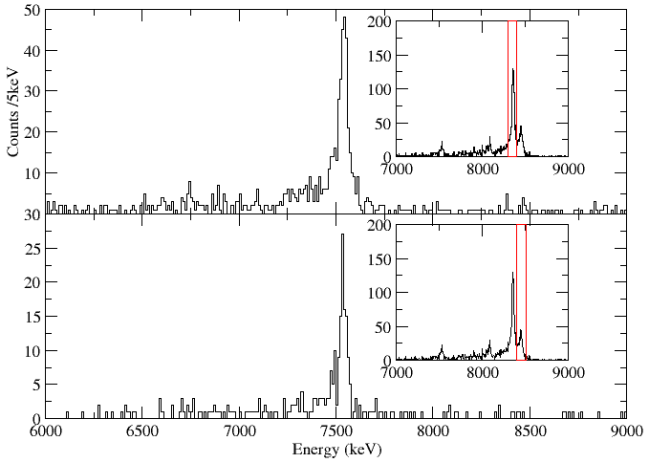

Figure 6.7: Two recoil-$\alpha - \alpha$ correlated spectra inset with gating conditions on the α energy from the mother nucleus.

spectrum shown in the lower panel of Figure 6.6 is produced. Here ^{251}Md is the only peak in the spectrum.

By gating on the first α decay energy in recoil-α-α correlation, it can be seen that gating on either of the strong α decay peaks in ^{255}Lr that they are both correlated to the 7550 keV α decay in ^{251}Md, this is shown in Figure 6.7 where it can be seen that both ^{255}Lr peaks are correlated with the ground state α decay of ^{251}Md [Cha06]. Unfortunately the statistics were not high enough to perform α-γ correlations and gain any information about excited states in ^{251}Md.

6.2.2 Half-life measurement

Implementing the RDT method it is possible to calculate the half-life of ^{255}Lr. When a recoil is detected in the DSSD and is then followed by an α-decay in the same pixel the time between these two events can be measured. Owing to the relatively long correlation time required for measurement of half-lives there is the problem of random correlation, due to a second recoil implanting within the same pixel as a previous recoil before the latter has decayed.

To overcome this discrepancy a double exponential is fitted to the decay curve with components τ_{short} and τ_{random}, which can then be related to the true lifetime by

$$\tau_{true}^{-1} = \tau_{short}^{-1} - \tau_{random}^{-1}. \tag{6.1}$$

The double exponential used for fitting is of the form

$$N(t) = Ae^{-\lambda_{random}t} + Be^{-\lambda_{short}t}. \tag{6.2}$$

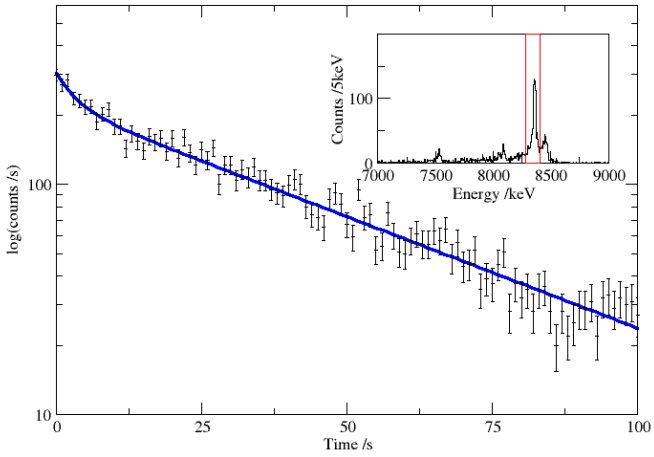

Figure 6.8: Decay curve for correlated α decays in 31 s half-life peak. Inset shows the gating conditions with respect to α-particle energy.

The search time between recoil implantation and α-decay was set to 3 half-lives [Cha06], 100 s, to ensure that all ^{255}Lr nuclei were detected. It should be noted that for the shorter half-life, 2.5 s, measurement a single exponential was fitted to the data, this can be seen in Figure 6.9. For the longer half-life decay, 32 s, a double exponential was used, as there is a significant proportion of the shorter decay within the gate due to the low-energy tail of the shorter decay this can be seen in Figure 6.8. The half-life for the two decays was extracted from the fits and found to be $t_{1/2} = 31.93(53)$ s for the longer decay, and $t_{1/2} = 2.577(50)$ s for the shorter decay. These values are consistent with previously published values of $t_{1/2} = 2.3(10)$ s and $t_{1/2} = 31.1(13)$ s [Cha06].

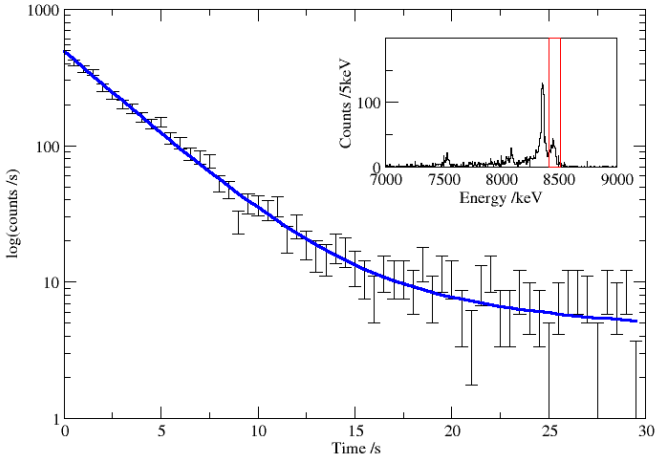

Figure 6.9: Decay curve for correlated α decays in 2.5 s peak. Inset shows the gating conditions with respect to α-particle energy.

6.2.3 Isomeric decay

Using the RDT method detailed in Section 6.2.1, isomeric decays can also be measured. Isomeric states can decay through a combination of γ-ray and conversion-electron emission. The correlation time between recoil implantation and isomeric decay is limited at 10 ms, which should be sufficient to allow all isomeric states to decay based on the known isomeric state with a half-life of 1.7 ms [Jep09]. Approximately 5200 electron showers were detected in the DSSD which are correlated with a recoil implantation within the aforementioned time condition. Of these, approximately 92% have a half-life of 1.73(4)ms and the remaining 8% decay with a half-life of 118(7)μs. This first isomeric decay has been seen and is consistent with published values [Jep09]. This shorter isomeric state is due to contamination from ^{206}Pb created by

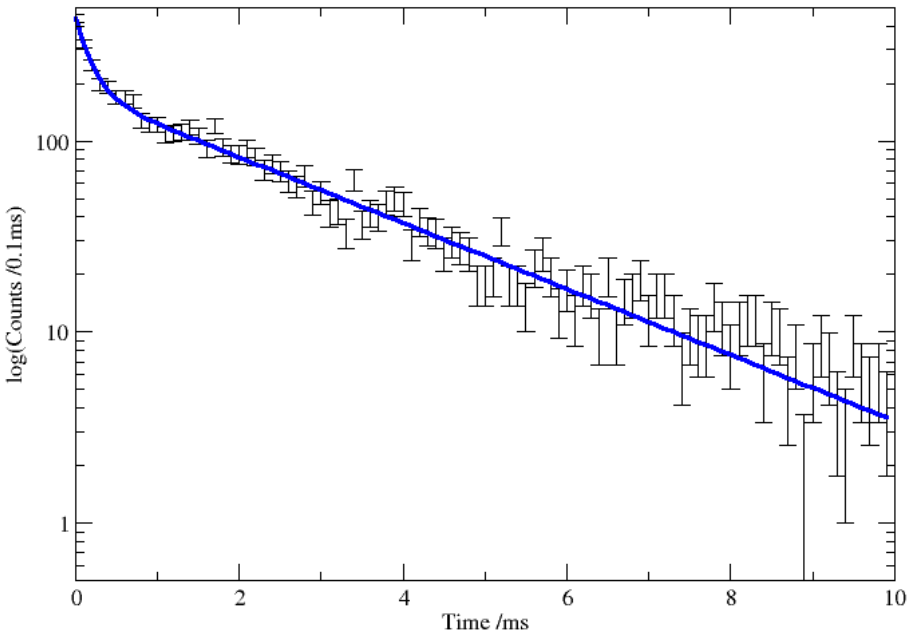

Figure 6.10: Decay curve for correlated isomeric decays, the short half-life component is due to contamination from ^{206}Pb.

transfer reactions in the target.

The decay of isomeric states within ^{255}Lr is explored through observation of a recoil implantation in the DSSD followed by an lower energy signal in the same pixel indicating electrons generated in the isomeric decay. The γ rays coincident with this can then be extracted. This is achieved using the planar detector, the GREAT focal plane Clover and two further Clover detectors. The planar detector has higher efficiencies at lower energies and is more suited to detecting low energy γ-ray and X-rays. The three Clover detectors are more efficient at higher energies.

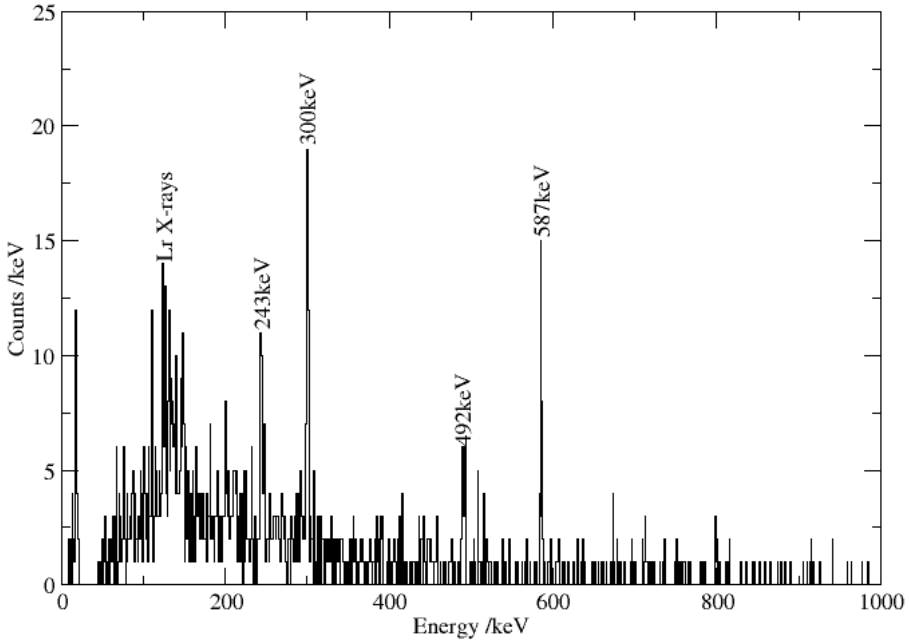

Figure 6.11: Recoil-electron tagged γ-ray spectrum from the focal plane Clover detectors.

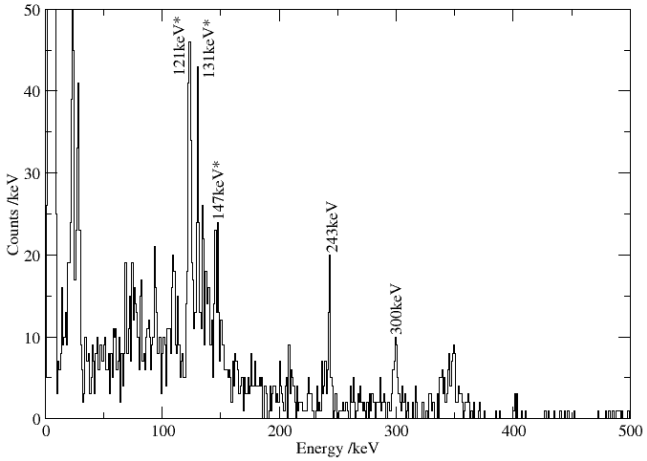

Figure 6.12: Recoil-electron tagged γ-ray spectrum from the focal plane planar detector, peaks marked with an * are known lawrencium X-rays.

	Jeppesen *et al.*	This work
Beam time	5 days	14 days
Beam intensity	200 pnA	105 pnA
Number of α decays	2.2×10^4	1.2×10^4
Number of electron bursts	4.9×10^3	5.2×10^3

Table 6.2: Comparison of experimental details between Jeppesen *et al.* and this work.

Figure 6.11 and Figure 6.12 show the recoil-electron γ-ray spectra. There are a number of peaks visible that have been observed previously by [Jep09].

Table 6.2 compares some values relating to the study performed by Jeppesen *et al.* and the one performed here. It can be seen that, the number of α decays detected was significantly higher, whereas electron bursts were comparable, though Jeppesen *et al.* saw less contamination from ^{208}Pb, so detected more ^{255}Lr isomeric decays. Even with lower statistics, this experiment should be more sensitive to γ rays with three Clover detectors compared

to one in the previous study. Though the spectrum obtained is missing many peaks, including the 387 keV transition out of the proposed short isomeric state. The intensities of the 492 and 587 keV transitions are also completely different to the 494 and 588 keV transitions seen previously. Finally no time delay could be measured between the two states depopulating the higher isomeric state and those depopulating the lower isomeric state. Which was the justification for the existence of this state by Jeppesen *et al.*.

6.3 Discussion of Decay spectroscopy

Figure 6.2 shows a proposed α decay scheme for ^{255}Lr to ^{251}Md and subsequent decay to ^{247}Es. Whilst it was possible to perform a recoil-α-α analysis, see Section 6.2.1 the statistics were insufficient to differentiate the four proposed α decays shown in Figure 6.2. Furthermore there were insufficient α-γ coincidence data to distinguish the states being populated in ^{251}Md.

It has been suggested by Chatillon *et al.* [Cha06] that the shorter half-life α decaying state also decays into the ground state owing to an observed short period increase in the α decay rate before the exponential decay. As can be seen in Figure 6.13, this effect has not been observed here.

The presence of an isomeric state in ^{255}Lr has been previously identified [Hau08, Jep09]. Jeppesen *et al.* [Jep09] proposed the level scheme shown in Figure 6.1 with two isomeric states of half-lives 1.70(3)ms and tens of nanoseconds. Hauschild *et al.* [Hau08] alternatively proposed a half-life of 1.4(1)ms for a single isomer but an isomer with a half-life of tens of nanoseconds was not present.

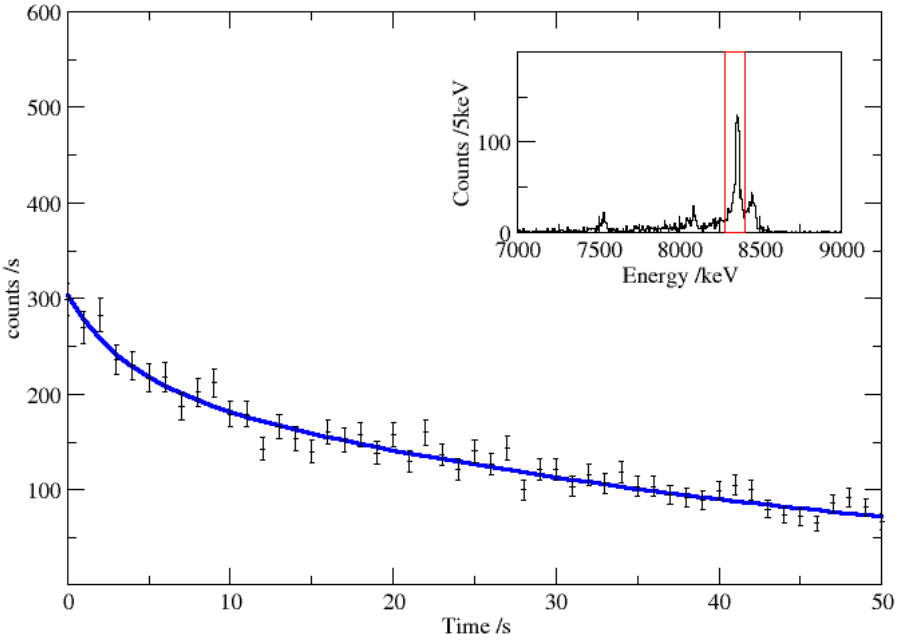

Figure 6.13: α decay curve for correlated α decay in longer lived peak, inset shows gating conditions.

In this work an isomer of half-life, 1.73(4)ms has been measured, which is in close agreement with the previously measured value [Jep09]. However, where Jeppesen *et al.* detected a second shorter lived isomer there is no evidence for it here. This second isomer was suggested owing to a time delay seen between the emission of the γ rays at 244, and 301 keV compared to the three transitions depopulating the isomer 387, 494 and 588 keV. This effect cannot be seen here.

Unfortunately, the amount of γ-ray data collected here is lower than the previous study [Jep09]. There was insufficient data to perform γ-γ coinci-

dence analysis and using the RDT method where the decay of the isomeric state is signified by an electron shower [But02] detected in the DSSD to detect γ-rays from transitions below the isomeric states was not possible.

6.4 In-beam spectroscopy

The second, in-beam, part of the experiment employing the SAGE spectrometer, consisting of the JUROGAM II array and the SAGE silicon detector, placed around the target position to both prompt γ rays and conversion electrons. Events at the focal plane are used to identify relevant radiation at the target position. When there is a ^{255}Lr recoil implantation event at the focal plane, this means that a ^{255}Lr nucleus was created $\sim 0.9\,\mu$s earlier at the target position. This correlation allows for the selection of γ ray and electron emissions coincident with the creation of the ^{255}Lr nucleus.

6.4.1 Gamma-ray spectroscopy

Owing to the low production cross-section of ^{255}Lr and the large amount of background, the γ-ray statistics are rather meagre and can do little to expand upon the results already presented by Ketelhut *et al.* [Ket09].

Figure 6.14 shows the γ-ray data gained by requiring a recoil-like event in delayed coincidence. The strongest features are the X-rays associated with lawrencium and bismuth. Furthermore the rotational band and strongly coupled band structures detailed by Ketelhut *et al.* [Ket09] are hard to discern without prior knowledge. For simplicity the structures described by Ketelhut *et al.* [Ket09] will be referred to as the rotational band, containing

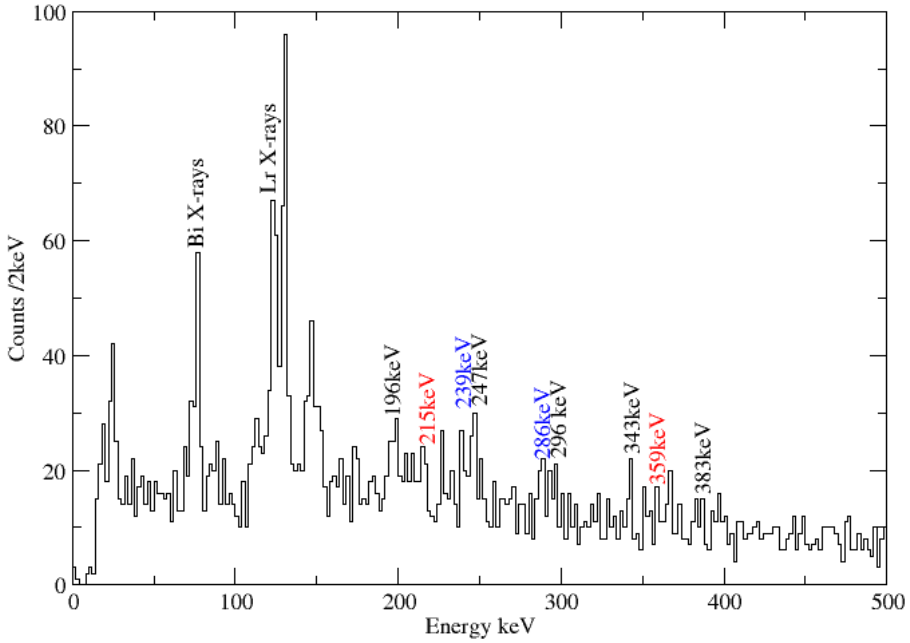

Figure 6.14: Recoil-gated γ-ray spectrum from the JUROGAM II array. Black labels indicate transitions in rotational band, red and blue indicate the two signature partner bands in the strongly coupled band.

the transitions 197,247, 296, 343, 386, and 430keV, and the strongly coupled rotational band, or first and second signature partner bands, which contain the transitions 189, 239, 288, 338, and 384keV and 215, 264, 314, and 359keV respectively.

Figure 6.15 shows the $\gamma\gamma$ coincidence data generated by summing coincidences of gates on all known transitions in the structures suggested by Ketelhut *et al.* [Ket09]. From these data alone there are no strong coincidences and nothing further to be extracted about the level structure of

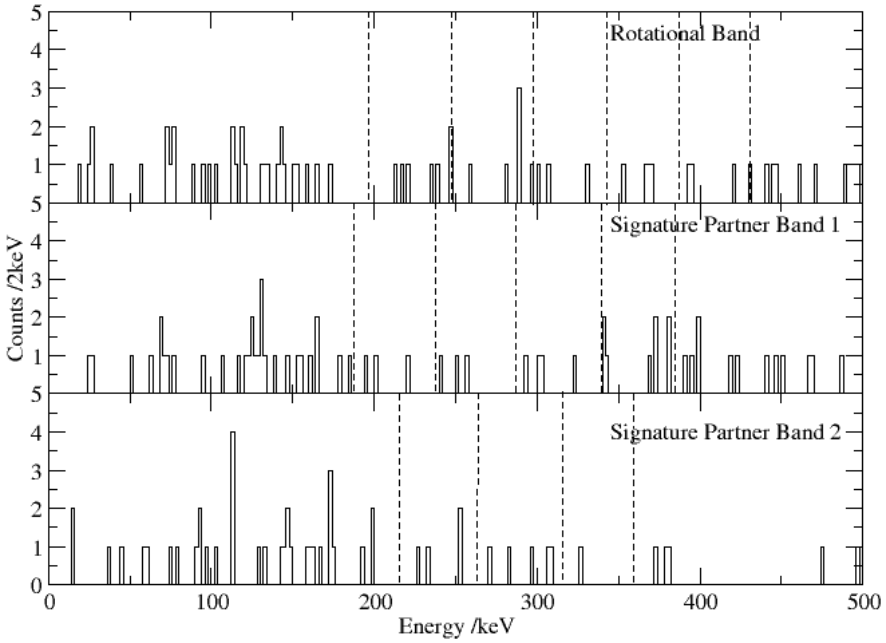

Figure 6.15: Recoil-gated $\gamma\gamma$ coincidence spectra, gating on a) known γ rays in the rotational band b) known γ rays in the first signature partner band c) known γ rays in the second signature partner band.

^{255}Lr.

6.4.2 Conversion-electron spectroscopy

For the first time, alongside the measurement of γ-ray data, conversion-electron emission has been measured for ^{255}Lr. This has potential to provide a greater insight into the nuclear structure, as the combination and interplay of these two probes of nuclear structure can offer a wealth of information.

Figure 6.16 shows the conversion-electron spectrum gained by requiring

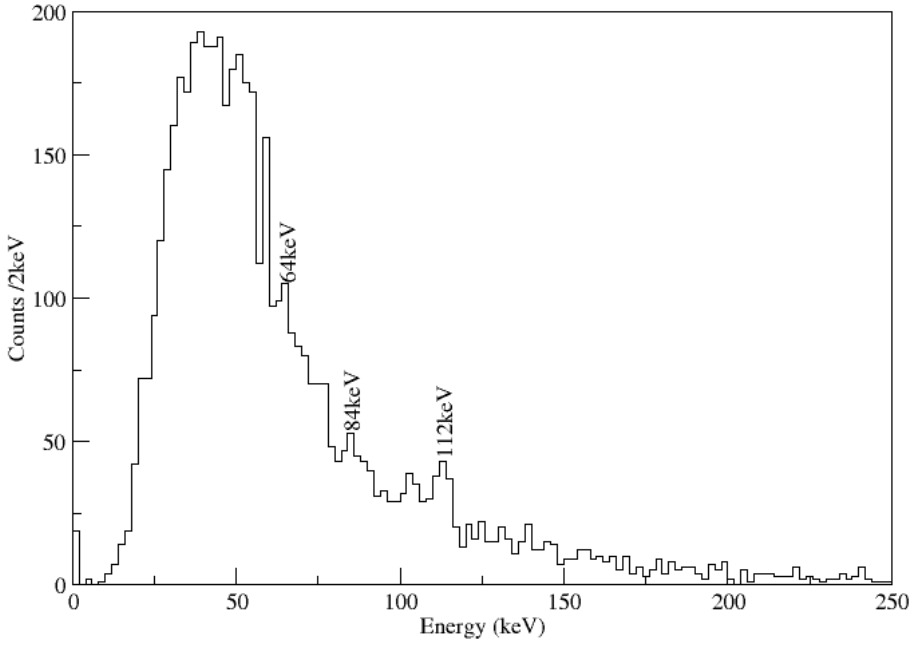

Figure 6.16: Recoil-gated conversion electron spectrum from the SAGE silicon detector, a number of prominent peaks are labelled, energies are uncorrected for binding energy.

a delayed coincidence with a recoil-like event.

There are a number of notable features in Figure 6.16. Firstly it should again be noted that the high voltage barrier potential was set to -38kV for the majority of the experiment, though it was altered between -35kV and -40kV at times. This is responsible for the significant decrease in counts for energies below $\sim$35 keV. Labelled are a number of potentially interesting transitions.

Further requiring a ^{255}Lr decay within the same pixel as a recoil nucleus

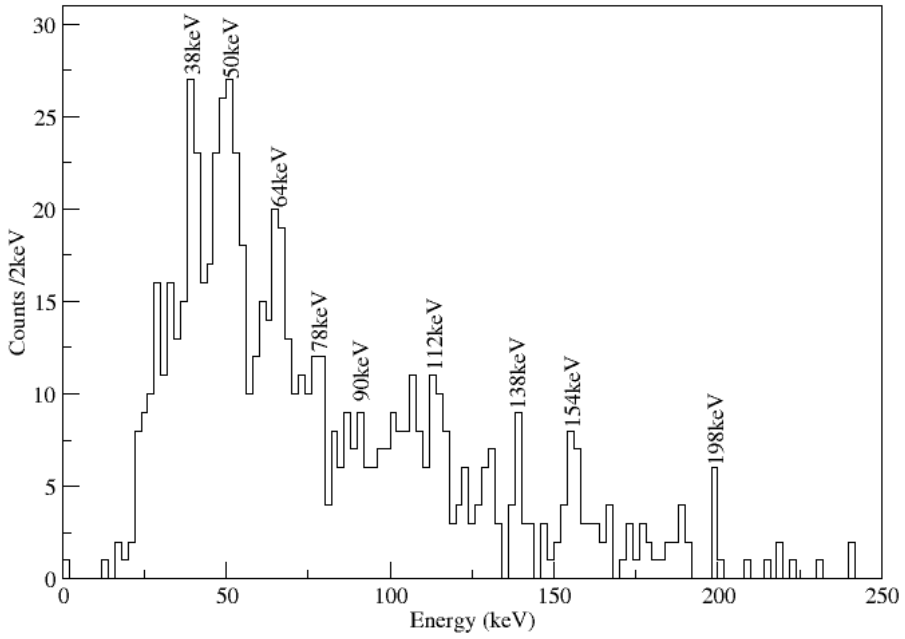

Figure 6.17: Recoil-α-gated conversion electron spectrum from the SAGE silicon detector, a number of prominent peaks are labelled, energies are uncorrected for binding energy.

allows for a cleaner electron spectrum to be produced. This can be seen in Figure 6.17, where additional peaks have been marked.

Figure 6.18 shows the recoil-gated γ-electron coincidence data summed from all known transitions in the structures suggested by Ketelhut *et al.* [Ket09].

As can be seen in Figures 6.19, 6.20, and 6.21, by gating on the electron peaks visible in Figures 6.16 and 6.17 in the γ-electron coincidences there is little to strongly indicate which electrons are coincident with which

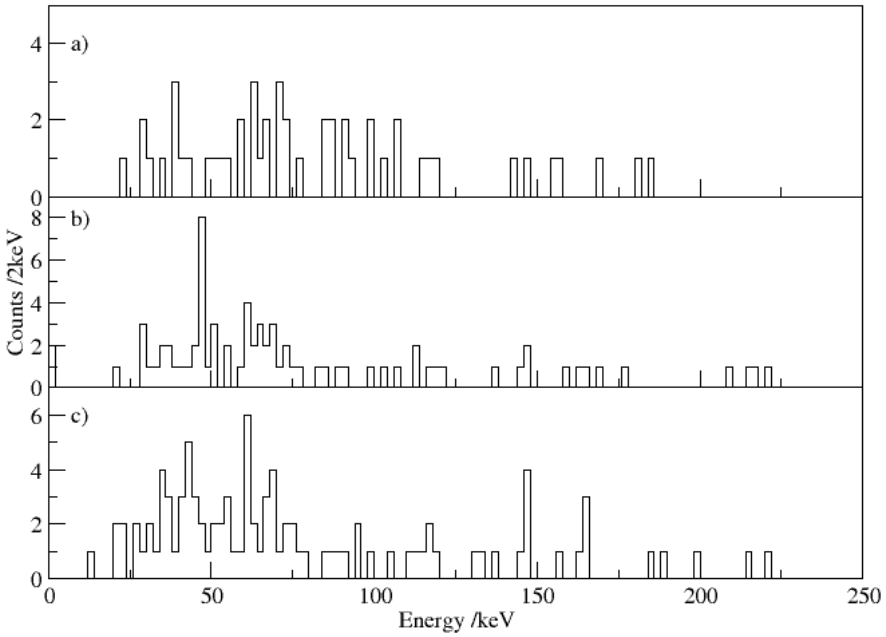

Figure 6.18: Recoil-gated γ-electron coincidence spectra, gating on a) known γ rays in the rotational band b) known γ rays in first signature partner band c) known γ rays in second signature partner band.

band. Overlaid onto each spectrum are the previously known transitions from Ketelhut *et al.* [Ket09].

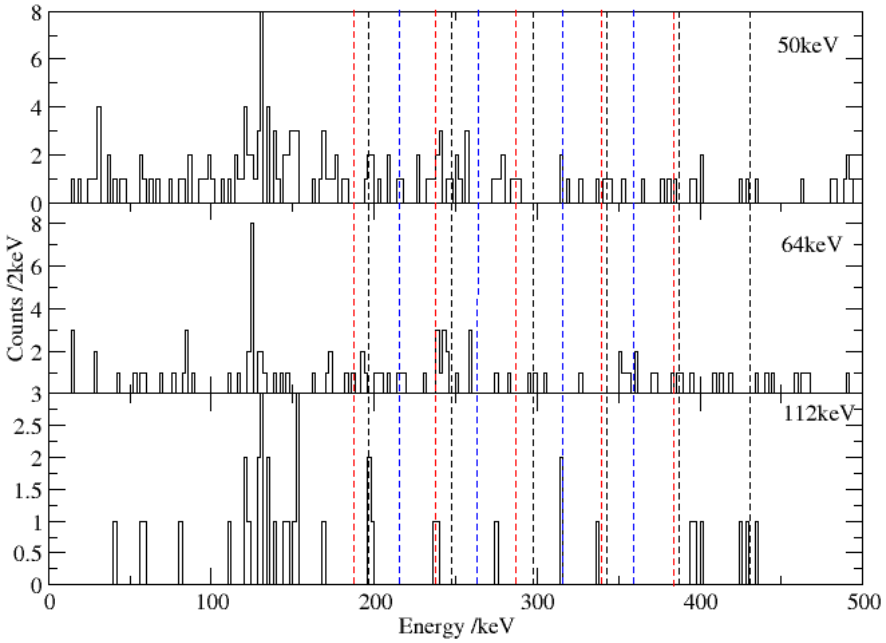

Figure 6.19: Recoil-gated γ-ray spectrum gating on electrons at (upper) 50 keV, (middle) 64 keV, and (lower) 112 keV transitions. Shown in black, blue, and red, are the transitions in the rotational band, first signature partner and second signature partner bands, respectively.

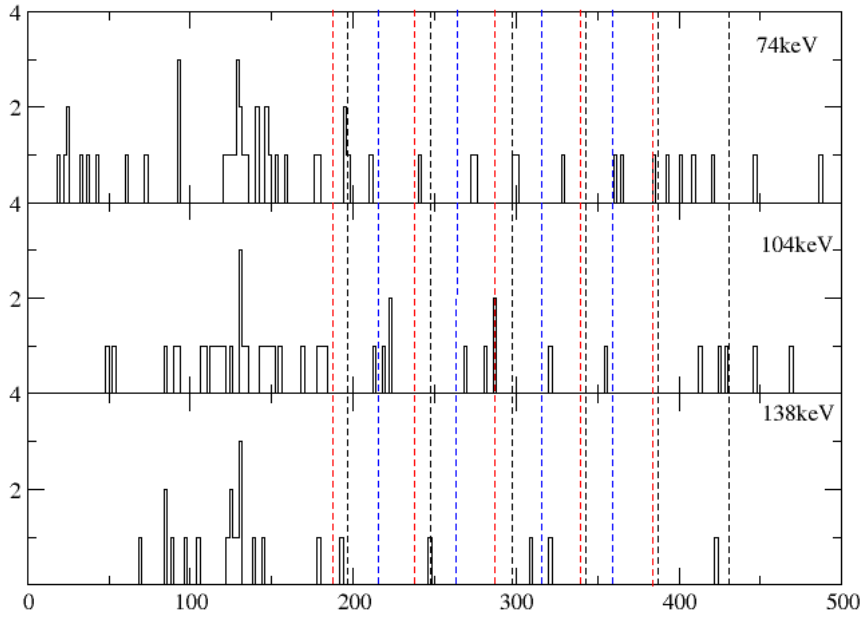

Figure 6.20: Recoil-gated γ-ray spectrum gating on electrons at (upper) 76 keV, (middle) 104 keV, and (lower) 138 keV transitions Shown in black, blue, and red, are the transitions in the rotational band, first signature partner and second signature partner bands, respectively.

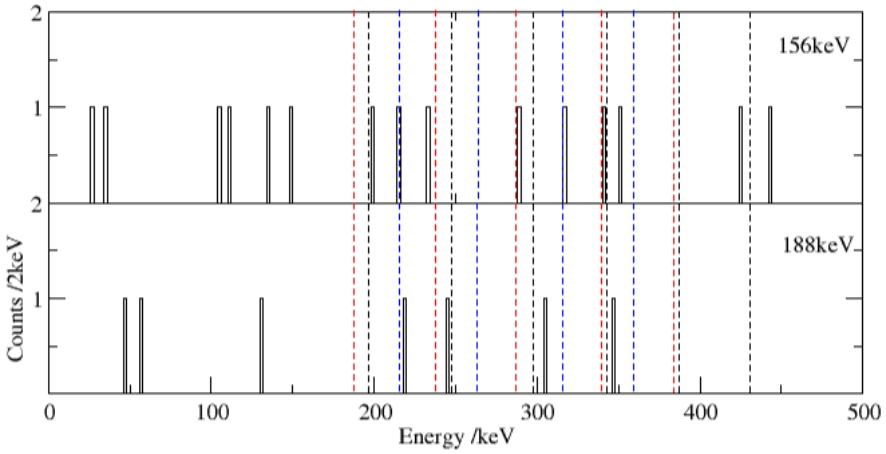

Figure 6.21: Recoil-gated γ-ray spectrum gating on electrons at (upper) 156 keV, and (lower) 188 keV transitions Shown in black, blue, and red, are the transitions in the rotational band, first signature partner and second signature partner bands, respectively.

6.5 Discussion of Recoil-Gated in-beam spectroscopy

The previously known states in ^{255}Lr are detailed in Figure 6.22 [Ket09]. Further to this, there are expected to be a series of M1 transitions linking the coupled bands built upon the [514] configuration. There are also expected to be M1 transitions connected this band with the ground-state band built upon the [521] configuration. Ketelhut *et al.* [Ket09] previously examined the dynamical moment of inertia for comparison with ^{251}Md and theoretical values.

6.5.1 Spin assignment of 1/2- [521] band

It has previously been shown by Chatillon *et al.* [Cha06] that the ground state of ^{255}Lr is of spin and parity $1/2^-$. The rotational band structure detailed in Section 6.4 has been tentatively assigned to be built on the $1/2^-$ ground state.

Figure 6.23 details the kinematic moment of inertia (J_1) for different values of the spin of the lowest known state in the 1/2- band. In the superheavy region, few nuclei have many, if any, excited states known. So it can be useful to look at other, better known regions of the nuclear chart to find systematic trends to inform the interpretation of results. In ^{255}Lr much of the structure is believed to be built upon the single particle states $1/2^-$[521] and $7/2^-$ [514] owing to the single unpaired proton. Potentially useful nuclei for com-

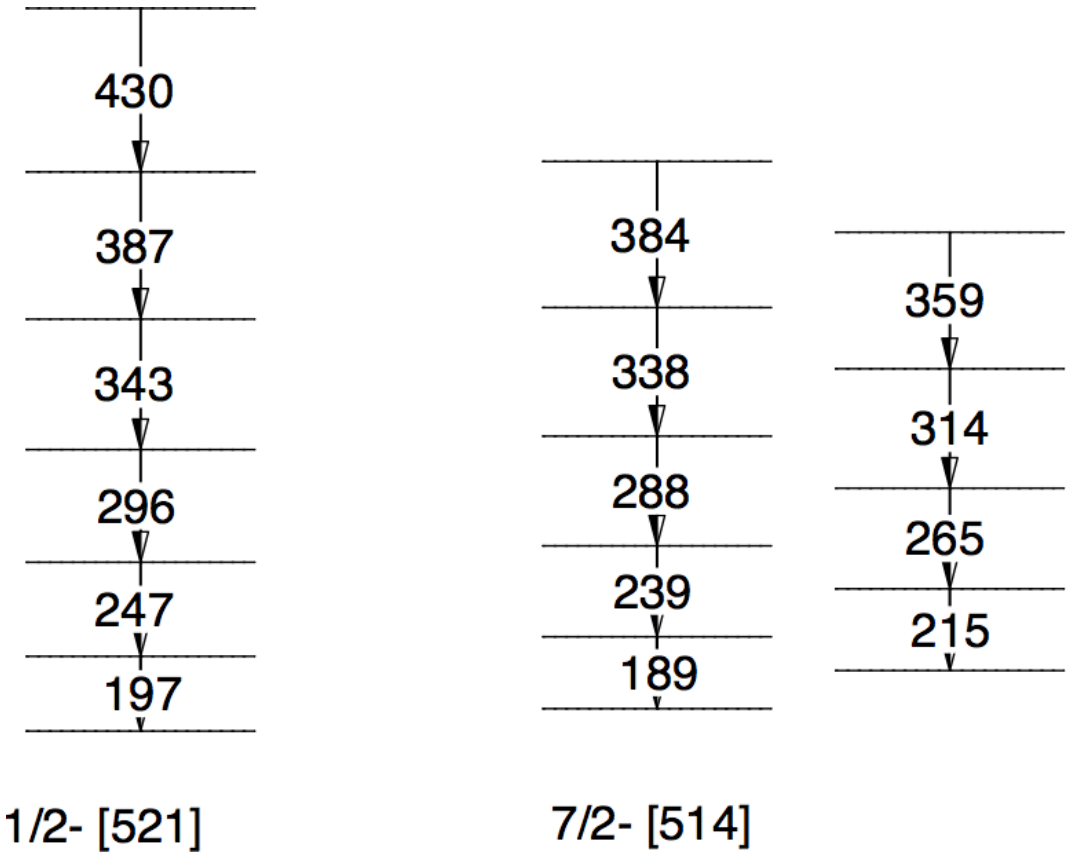

Figure 6.22: Previously known bands from [Ket09].

parison are those with 103 neutrons, as a number of these have been studied extensively. The two nuclei ^{179}Os and ^{181}Pt have 103 neutrons each, and have structure built upon the same single particle states. Figure 6.24 shows the comparison between different values for the lowest unknown spins in ^{255}Lr compared to the same structures in ^{179}Os and ^{181}Pt. The absolute values differ, however the overall trend is the same.

It can be seen that, based on systematics, the assignment for the spin of the lowest known state of $17/2^-$ is the most likely. This would give three transitions between the lowest known state in the $1/2^-[521]$ band and the

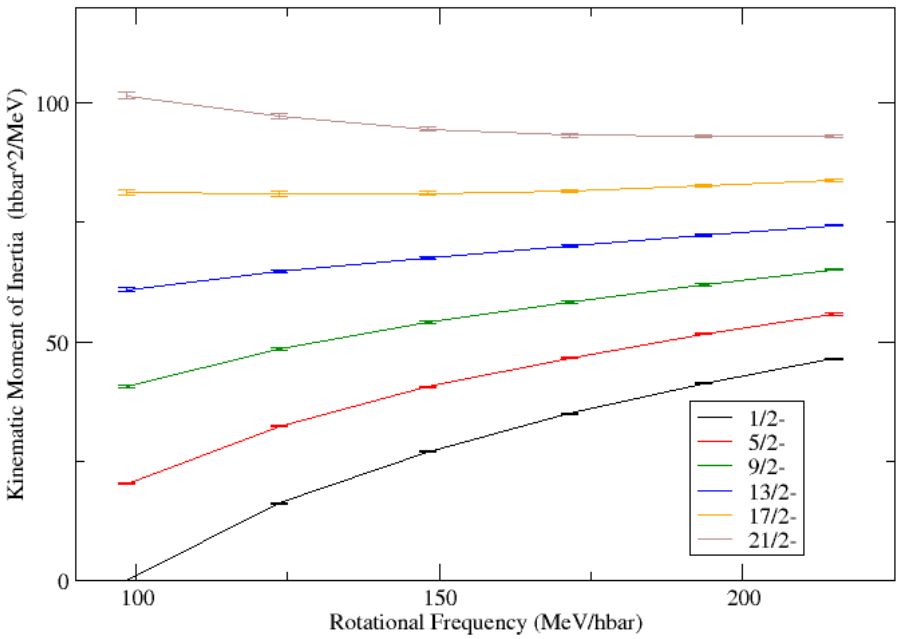

Figure 6.23: Kinematic moment of inertia for different values of spin of lowest known level in $1/2^-$ band.

ground state.

Figure 6.25 shows the J_1 and J_2 for both ^{255}Lr and ^{179}Os, note here a lowest known state spin value of 17/2 has been used. It can be seen that the relation between J_1 and J_2 follows the same trend in both cases, further supporting this assignment.

6.5.2 Spin assignment of 7/2- [514] band

Figure 6.26 shows different J_1 for different values of spin for the lowest known state built upon the 7/2- state. Also included is J_2 for comparison.

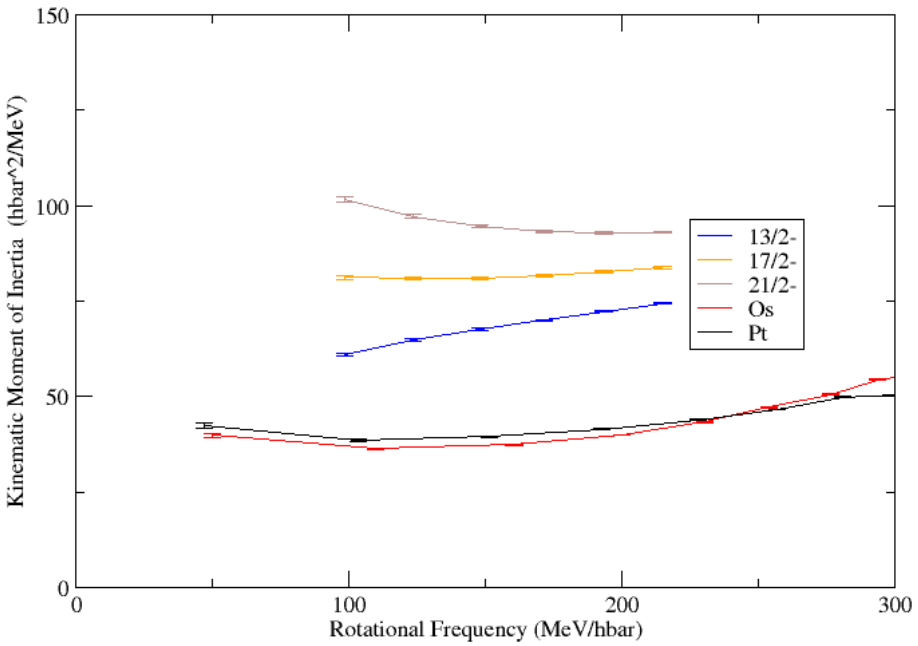

Figure 6.24: Comparison of kinematic moment of inertia for different values of spin of the lowest known level in the $1/2^-$ band of ^{255}Lr with ^{179}Os and ^{181}Pt.

As in the previous section, inspection of J_1 and J_2, and comparison to another nucleus with 103 neutrons, ^{181}Pt, shown in Figure 6.27 can be used to find a probable value for the lowest known spin. It can be seen that the most likely candidates for the spin of the lowest known state are $15/2^-$ or $19/2^-$, which would mean there are two or three unknown states at the bottom of each of the coupled bands.

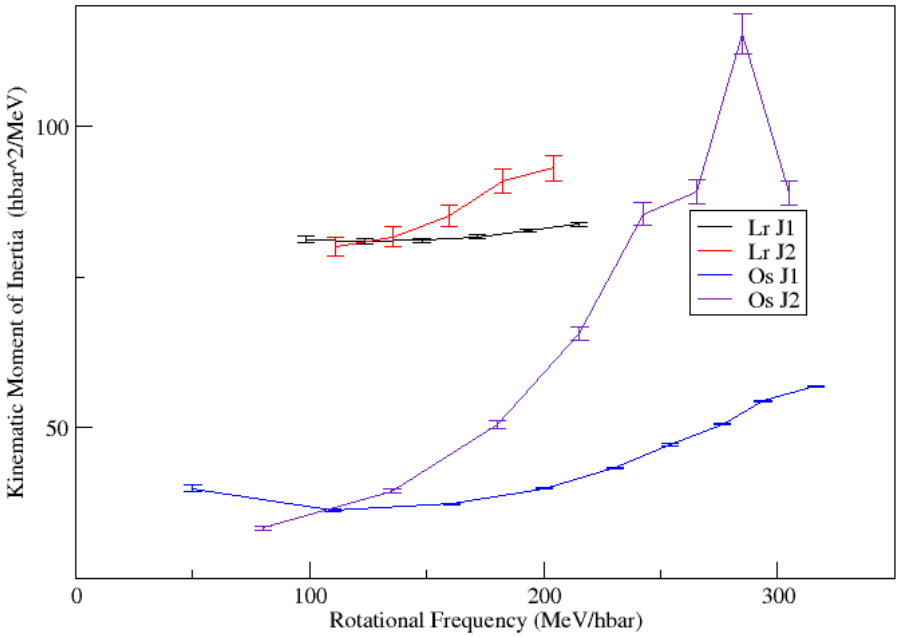

Figure 6.25: Comparison of the kinematic and dynamic moments of inertia for ^{255}Lr and ^{179}Os for excited states built upon the $1/2^-$ state.

6.5.3 Expansion upon known levels

From the in-beam data, two potential new transitions can be seen in the $1/2^-$ band, with energies of 91 and 140 keV. From analysis of the MoI in Sections 6.5.1 and 6.5.2, the unseen low-spin transitions in the level scheme can deduced by extrapolation.

Figure 6.28 shows a possible level scheme expanded to include all transitions down to the ground state. Likely energies based upon the energy change between known transitions have been chosen for the unseen low-energy tran-

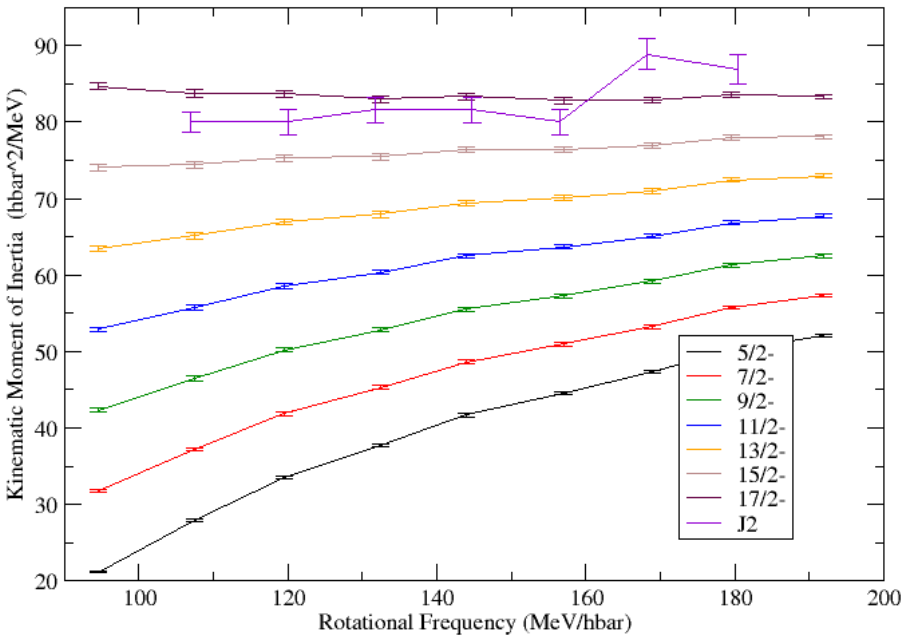

Figure 6.26: Kinematic moment of inertia for different values of spin of lowest known level in the $7/2^-$ band, also shown is the dynamic moment of inertia for comparison purposes.

sitions. Also shown are expected M1 transitions between the coupled bands and feeding into the ground state band. It should be noted that the spin assignment for the lowest known state in the coupled bands has been taken to be $15/2^-$ in this case. But an additional two transitions would be a good case for simulation and comparison in the future.

As has already been detailed in Section 6.4, the statistics in this experiment were not sufficient to perform any kind of meaningful coincidence analysis. The statistics were also so low that it is not possible to confidently

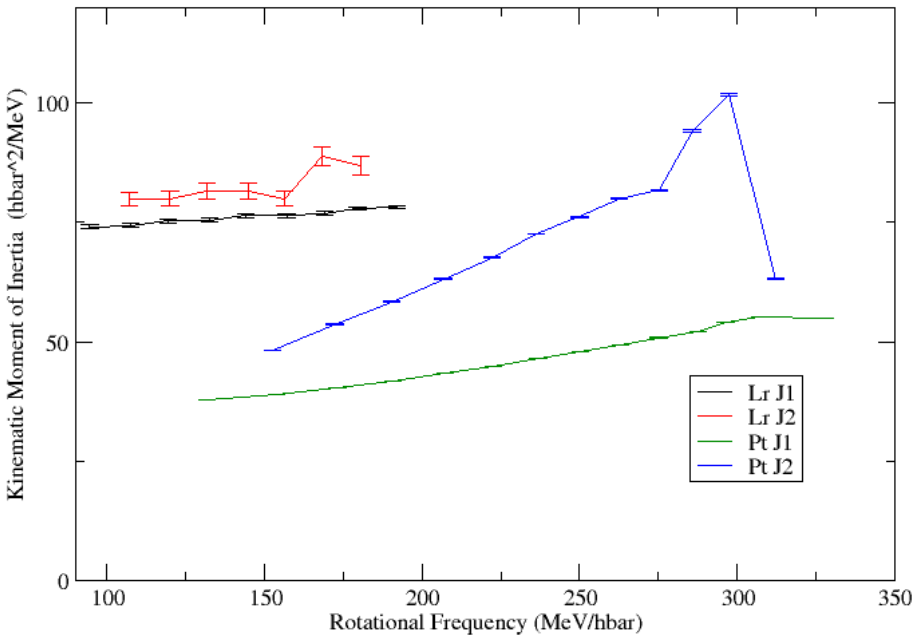

Figure 6.27: Comparison of the kinematic and dynamic moments of inertia for ^{255}Lr and ^{181}Pt for excited states built upon the $7/2^-$ state.

assign any linking transitions between the structures built on top of the $1/2^-$ states and $7/2^-$ states. It is also not possible to identify any inter-band M1 transitions between the strongly coupled bands.

Two relatively strong conversion electron transitions seen at 64 keV and 112 keV seen in Figure 6.16 correspond to γ-ray transitions of 91 keV and 140 keV respectively. It is possible that these are the two transitions at the bottom of the rotational band of the same energy in Figure 6.28.

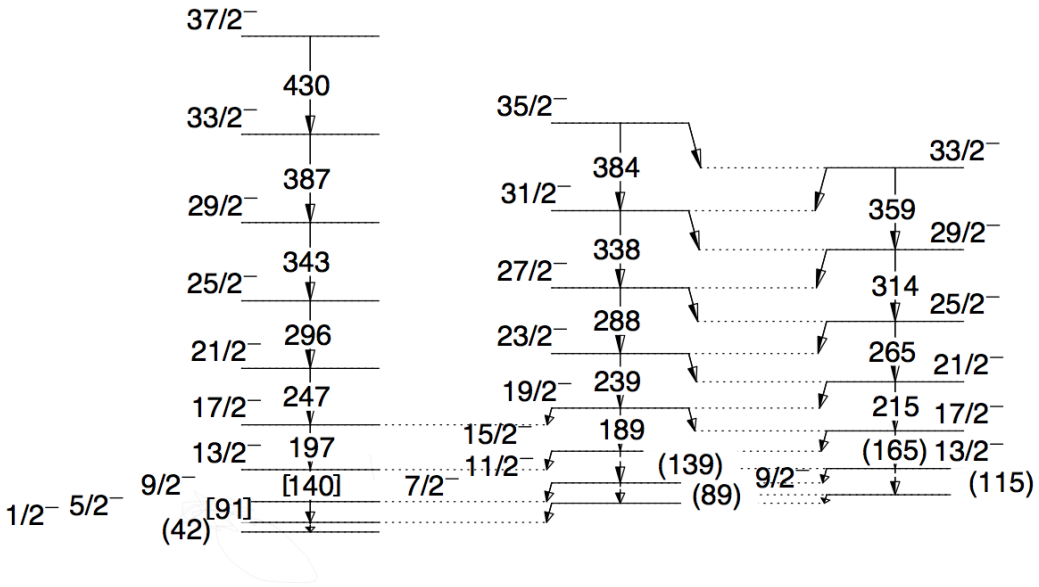

Figure 6.28: Proposed additional transitions based upon in-beam data and analysis of MoI, including expected M1 transitions. Unbracketed transitions have previously been seen, transitions in brackets are new to this work, transitions in parentheses have not been seen but are expected.

6.6 Comparison to simulated data

In a low cross section experiments such as this any firm coincidences are difficult to achieve, so any conclusions are hard to draw. Here the GEANT4 simulation detailed in Chapter 4 is useful. Possible level configurations can be simulated with much higher statistics than are currently possible experimentally. These different structures can then be compared to what is seen experimentally and the likelihood of different level structures can be assessed.

The complicated level structure shown in Figure 6.28 cannot be simulated fully though it is hoped that eventually it will be possible.

Currently the best approach available is to break this down into three

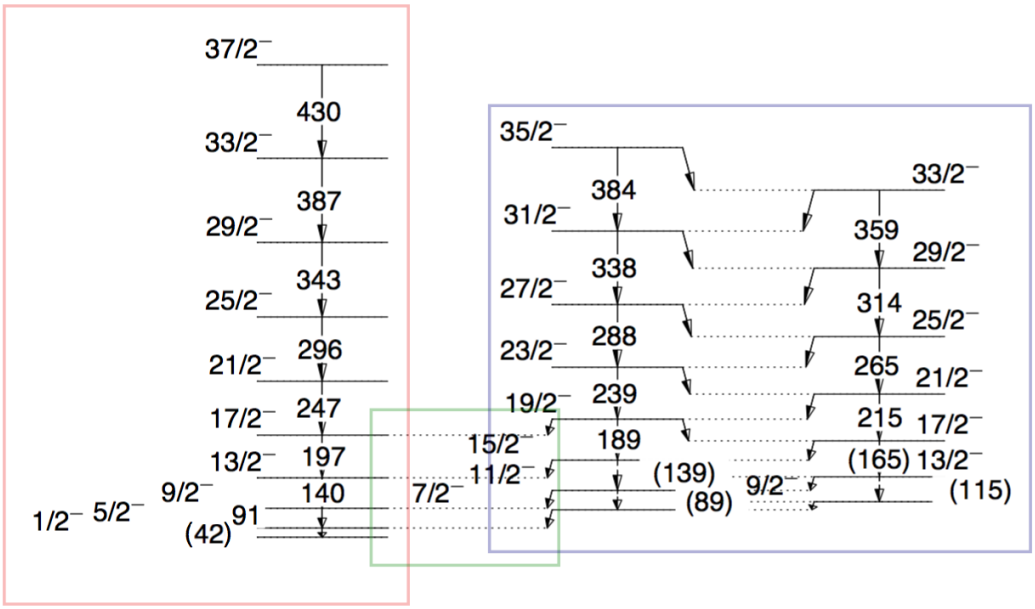

Figure 6.29: Proposed level scheme for ^{255}Lr broken down in the separate sections to be simulated.

separate structures as detailed in Figure 6.29. Firstly the rotational band is simulated, secondly the strongly coupled bands are simulated, finally the M1 transitions are simulated. Afterwards these can be combined. Unfortunately this method breaks any kind of inter-band coincidence analysis though, that ability is built into the code and intra-band coincidences can already be achieved. Further to the lack of complete coincidence analysis, the intensities of each of the three structures have to be tuned by hand, to match what would be expected if the complete structure had been simulated. Both of these shortcomings should be overcome in the future.

In such a structure as detailed in Figure 6.28, the M1 transitions from the coupled bands to the ground state band would be strong and highly converted. Inspection of the ^{255}Lr electron spectrum in Figure 6.17 shows

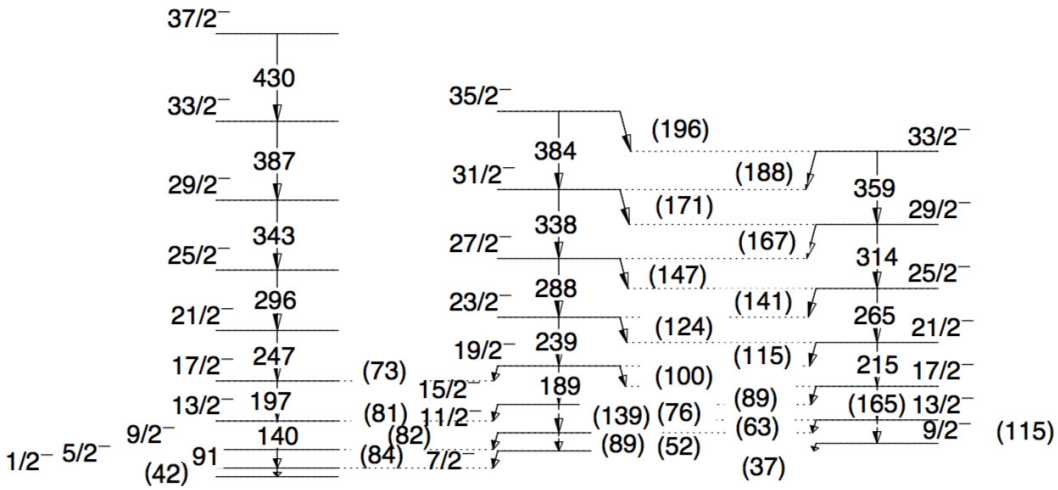

Figure 6.30: Level scheme of ^{255}Lr to be simulated in GEANT4, including all energies of M1 transitions, energies are in keV.

the strongest of the peaks at 50 keV, which would match the energy of and L electron emitted from a converted transition of energy 80 keV. By inspection of the energy differences between the levels in the ground-state band and the strongly coupled bands, one possible configuration gives energies of 84, 82, 81, and 74 keV for the transitions as the energy is increased. For the intra-band M1 transitions, there is less of a cue from the experimental evidence. Though there are still unassigned transitions seen in the electrons at energies of 104, 134, 168, 186, and 215 keV, it is not simple to assign these to the M1 transitions. One possible configuration which has transitions at 100, 141, 167, and 188 keV is shown in Figure 6.30. These of course do not completely match with what is seen, but with low statistics comes a large margin for error. Figure 6.31 shows three possible level structures built upon three different states expected to be close to the Fermi surface in ^{255}Lr: $1/2^-$ [521], $7/2^-$ [514], and $7/2^+$ [633]. The $1/2^-$ state is differentiable by the lack

of a signature partner band. For the two 7/2 states it can be seen from the transition rate ratios, T(M1)/T(E2), show that the band built upon the $7/2^-$ state would decay mainly through E2 transitions, whereas the band built upon the $7/2^+$ state would be significantly stronger in the M1 transitions. Taking the structures and simulating them separately allows for a clearer look into their features. Figures 6.33 and 6.34 show γ-ray and electron spectra for levels built upon the $7/2^-$ and $7/2^+$ configurations, respectively. Figure 6.32 shows the γ-ray and electron spectra generated by decays of the rotational band structure in ^{255}Lr. As can be seen by comparing Figures 6.34 and 6.33, if the levels were indeed built upon the $7/2^+$ configuration, the M1 transitions would be of comparable intensity to the strongest E2 transitions in the γ-ray spectrum. Referring back to Figure 6.14 this is not the case. Also in the electron spectrum, the structure would be noticeably different with the E2 transition conversion electrons being noticeably weaker, than potential M1 transitions, which is not the case in Figure 6.17. This provides further evidence that the structure is indeed built upon the $7/2^-$ state. Different amounts of decays through each of the structures can be combined, along with a representative amount of the M1 transitions that connect them to get a first estimation of a complete simulated spectrum. Taking the relative intensities of the strongest transitions in the ground-state band and the strongly coupled bands, 247 keV and 238 keV, respectively, gives a good first estimate to the ratio between decays proceeding through the ground-state band and decays proceeding through the coupled band is 3:2. It can also be assumed that every decay that proceeds through the strongly coupled band must end in one of the M1 transitions linking it to the ground state.

Taking these rough assumptions and combining the relevant amounts of each decay generates γ-ray and electron spectra given in Figure 6.35. Another current shortfall is that once a decay has proceeded through the coupled bands, the level at which it enters the ground-state band has not been taken into consideration. So the intensity of the transitions at 42, 91, 140 and 197 keV are underestimated.

Figure 6.36 shows direct comparison between simulation and ^{255}Lr-tagged electron spectra. Although intensities are not accurately reproduced, for reasons already detailed, there are still some conclusions that can be drawn.

It should be noted that for lower energies there is a slight discrepancy in the energy between simulated and measured electron spectra, most notably at 109 keV. In the simulation, there is a strong peak at 104 keV, which is generated by the L-conversion of the 140 keV transition. The actual energy of this peak should be around 109 keV. The reason for this is that energies measured in the simulation are uncalibrated and are absolute detected energies. In the experimental data, any energy lost in geometries such as carbon foils and dead layers will be cancelled out in calibration.

The peak at an energy of 50 keV in the experimental data spectrum is reproduced in the simulation by the peak generated by the linking M1 transitions with energies between 74 and 82 keV. So it is possible that these are roughly the energies of these inter-band M1 transitions.

Figure 6.37 shows a direct comparison between measured and simulated γ-ray spectra. It can be seen that the γ rays coming from the linking M1 transitions lie at approximately the same energy as the X-rays coming from bismuth and by inspection of the relative intensities these peaks would likely

not be visible at this level of statistics.

Another interesting feature is the similarity in intensity between the transitions at 238 and 247 keV and the 288 and 296 keV. The former of these two was used to tune the amounts of each structure that was used in the simulation, and so a similarity is to be expected. In the latter, the 296 keV transition is significantly weaker than the simulation would suggest, which hints at some discrepancy in the intensities. This highlights the sensitivity within the simulation of the intensity of transitions and so much care will need to be taken to ensure accuracy.

One feature missing from the measured data that the simulation would suggest would be prominent is the transition at 140 keV, especially with a contribution from the expected 139 keV transition in the strongly coupled rotational band. Though this effect could be small depending on where the strongly coupled rotational band depopulates to the ground-state rotational band. Nevertheless, the absence of this transition in the γ-ray spectrum is puzzling.

This comparison has focussed on only one possible level structure within ^{255}Lr due to time constraints. Now however it is possible to simulate any number of possible level structures for direct comparison to experimental data.

Figure 6.31: Possible structures built on various states in ^{251}Md[Cha07].

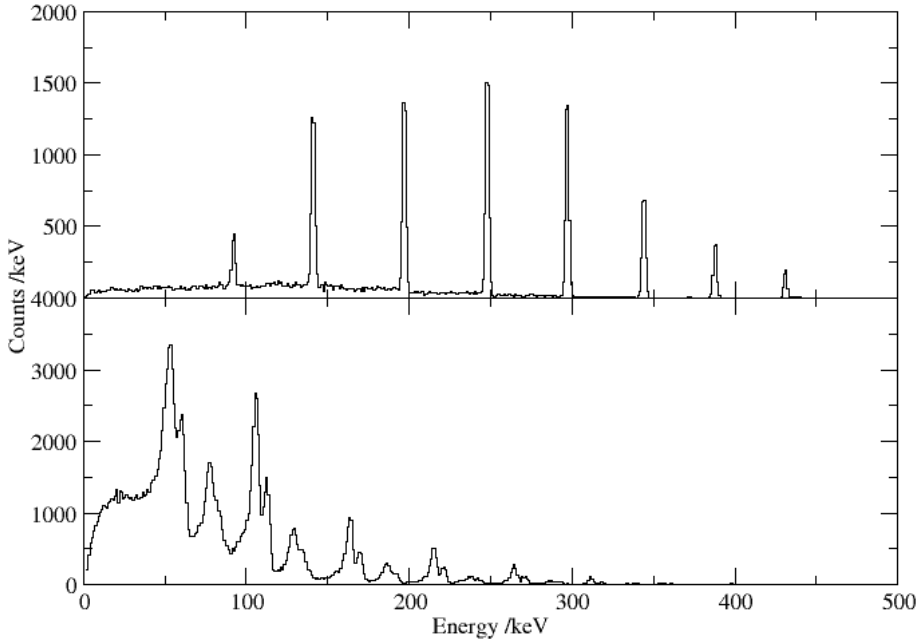

Figure 6.32: 1 million event simulation of rotational band built upon the $1/2^-$ configuration from ^{255}Lr.

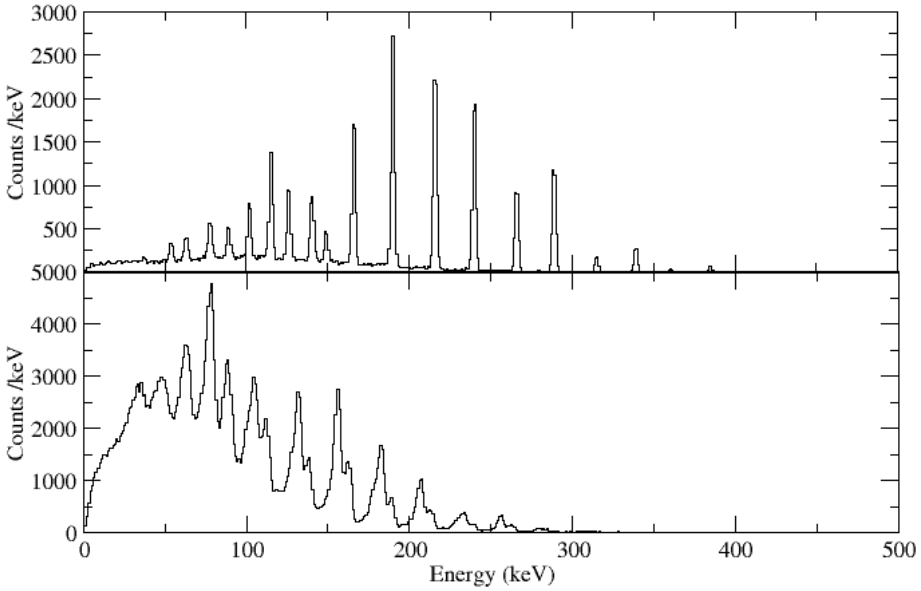

Figure 6.33: 1 million event simulation of coupled band from ^{255}Lr taking M1/E2 ratios for $7/2^-$ configuration.

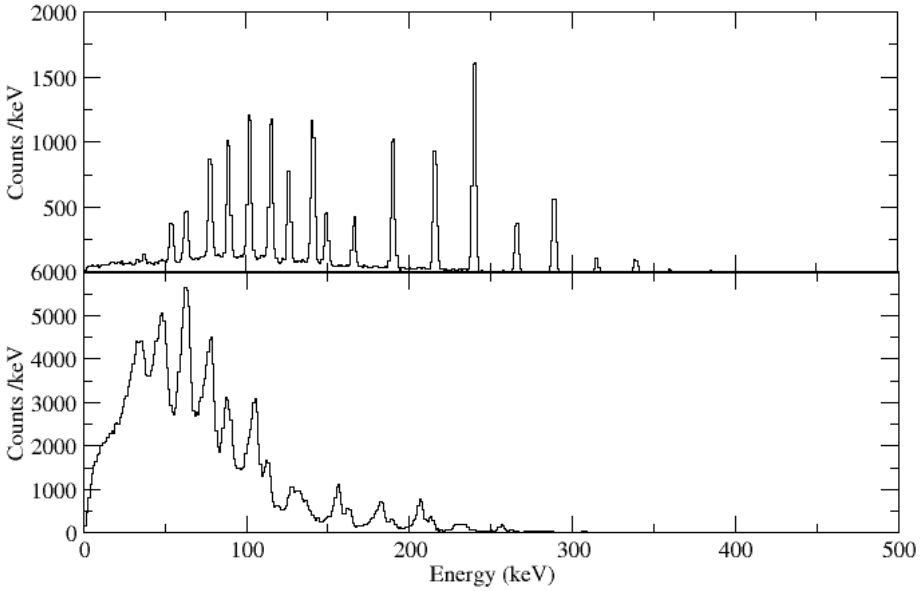

Figure 6.34: 1 million event simulation of coupled band from ^{255}Lr taking M1/E2 ratios for $7/2^+$ configuration.

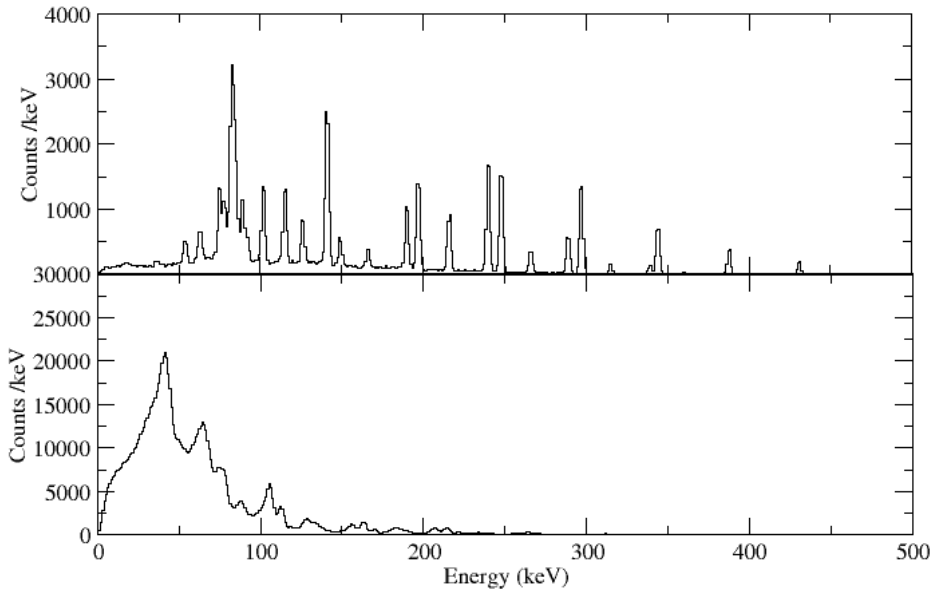

Figure 6.35: Combined simulated spectra for decay of ^{255}Lr.

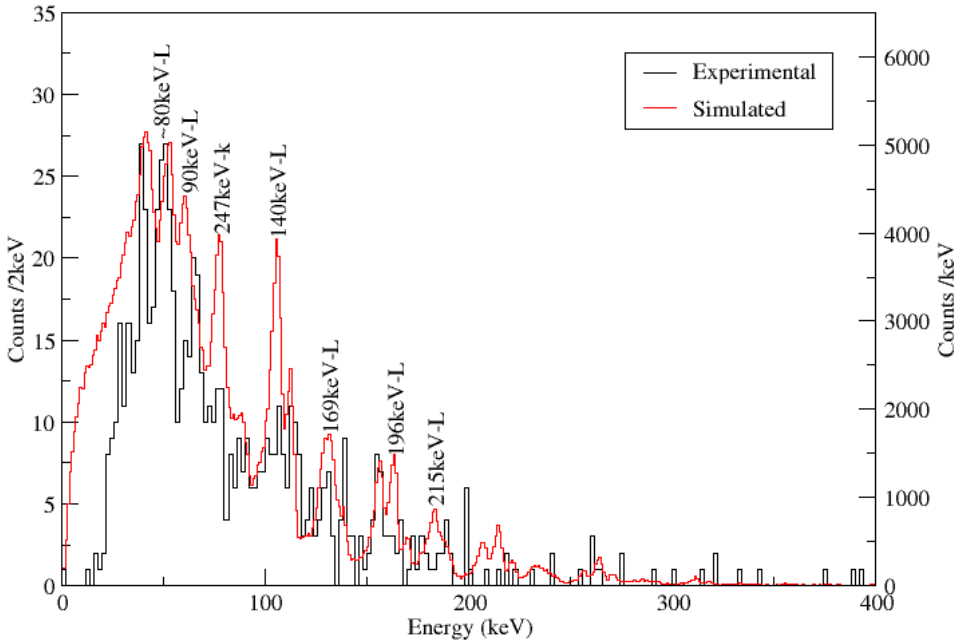

Figure 6.36: Comparison of simulated and measured ^{255}Lr-tagged electron spectra for ^{255}Lr Left axis shows experimental values, right simulated.

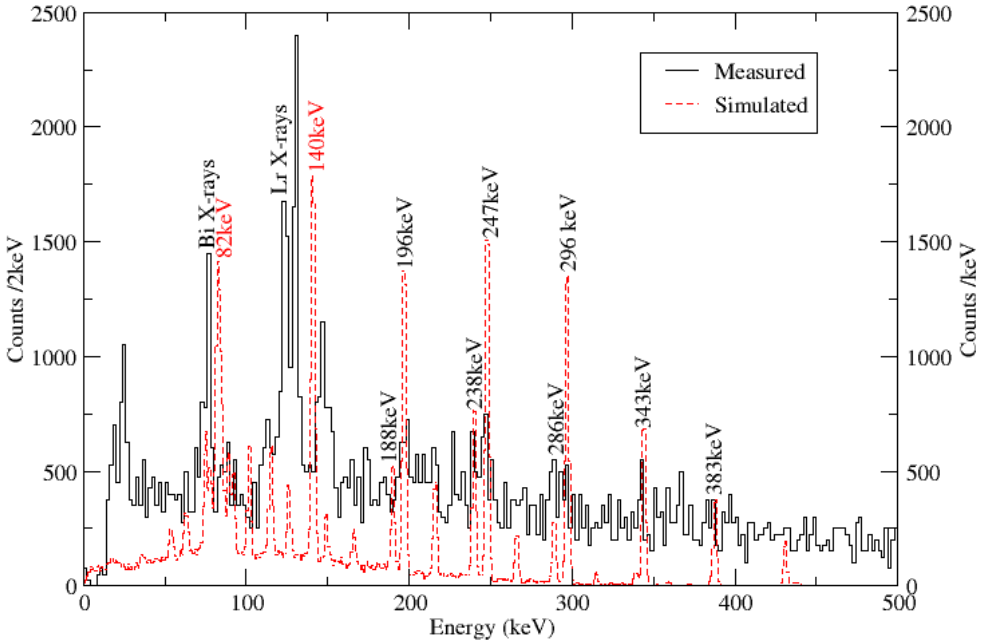

Figure 6.37: Comparison of simulated and measured electron spectra for ^{255}Lr Left axis shows experimental values, right simulated.

Chapter 7

Summary

7.1 Summary

The combination of the SAGE spectrometer with RITU and GREAT has been used to further the spectroscopic study of ^{255}Lr. The comprehensive GEANT4 simulation that has been developed alongside this study, has already proven invaluable in improving both the understanding of the experimental setup and directly improving the understanding of data from a number of experiments.

With respect to the focal plane component study of ^{255}Lr, there is further confirmation of an isomeric state previously seen. Unfortunately the statistics acquired were not sufficient to allow $\gamma - \gamma$ or $\alpha - \gamma$ coincidences that would allow confirmation of the level scheme proposed in [Jep09].

The in-beam study of ^{255}Lr for the first time combined both γ-ray and conversion-electron spectroscopy on the heaviest odd-mass nuclei ever studied. This has led to two new transitions at the bottom of the ground-state

band being tentatively assigned.

The GEANT4 simulation has proven to be a highly valuable tool in both the running of an experiment and the subsequent analysis. This study has shown its potential for use in subsequent experimental studies to take a potential level scheme and generate a large sample of simulated data for direct comparison to what is experimentally observed.

7.2 Outlook

^{255}Lr remains a highly interesting nucleus to study. Being an odd-mass nucleus it can be a highly sensitive probe for informing the next generation of shell models. A higher statistic experimental campaign for this nucleus could yield very interesting results that have as of yet only been hinted at.

The GEANT4 simulation package is now at a stage where it can be used to inform future experiments and subsequent analyses.

Appendix A

Nilsson Diagrams

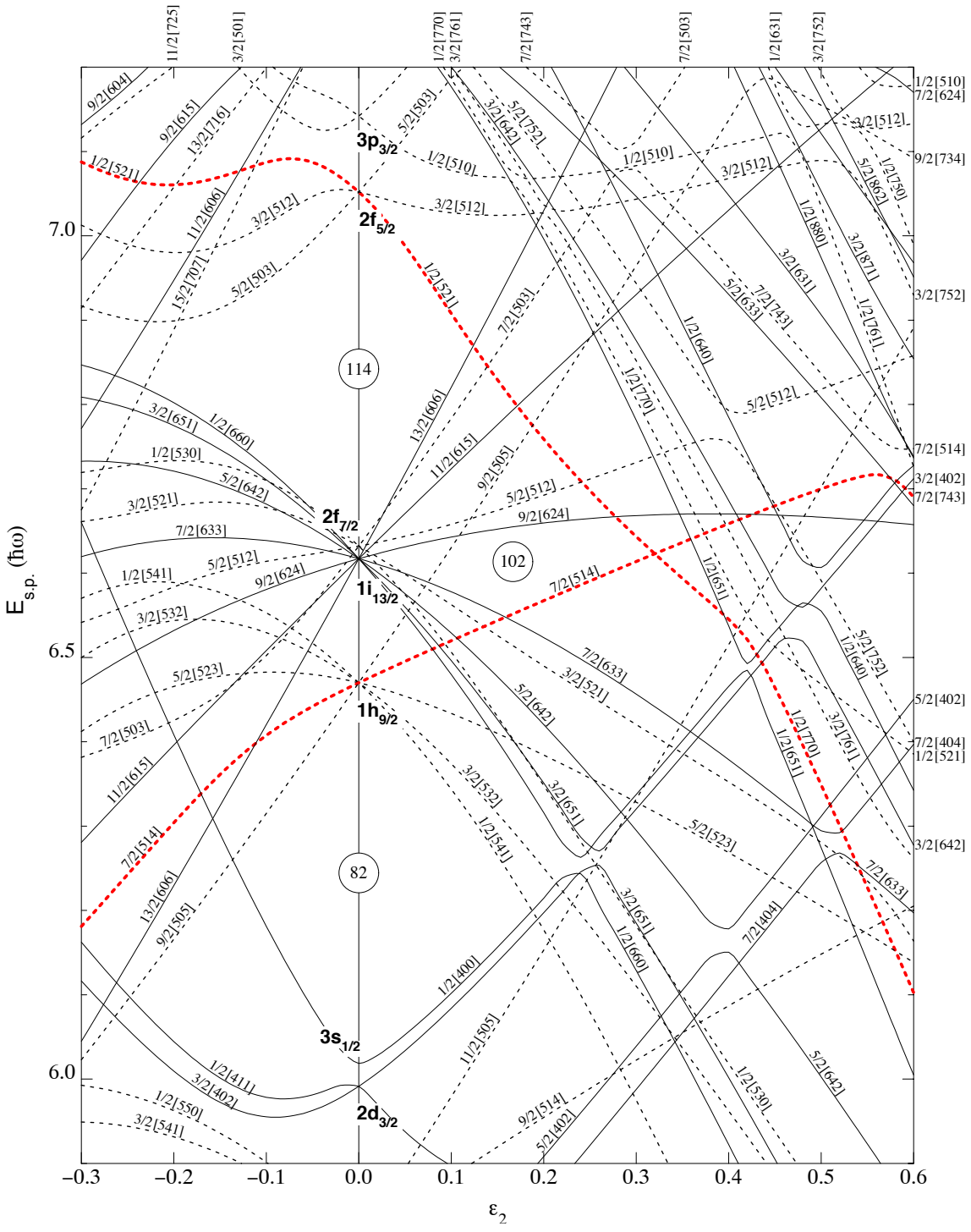

Figure A.1: Nilsson diagram for Z≥82, taken from [Fir99]

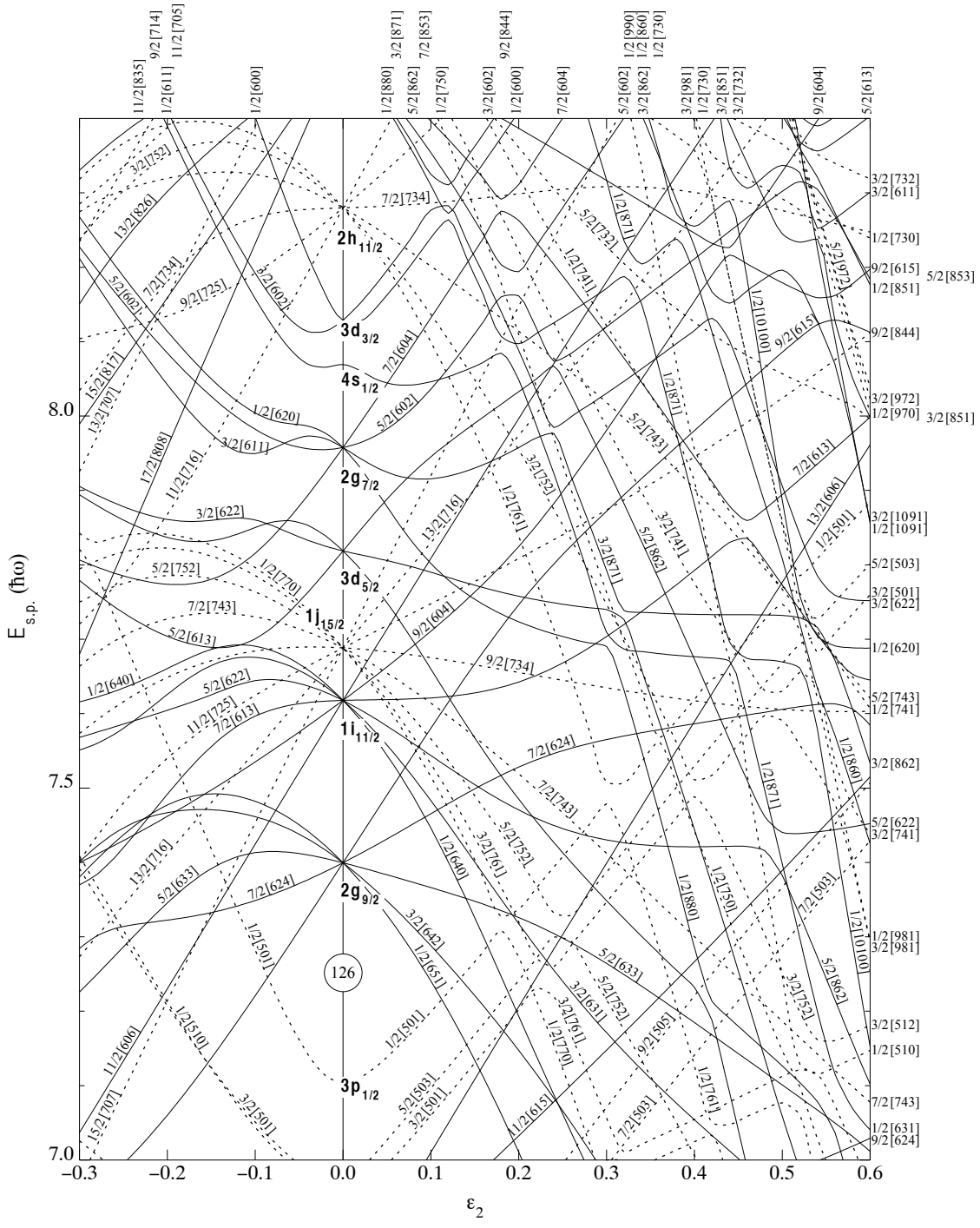

Figure 10. Nilsson diagram for neutrons, N ≥ 126 ($\varepsilon_4 = -\varepsilon_2^2/6$).

Figure A.2: Nilsson diagram for N≥126, taken from [Fir99]

Bibliography

[Afa03] A. Afanasjev, T. Khoo, and S. Frauendorf. 'Cranked relativistic Hartree-Bogoliubov theory: Probing the gateway to superheavy nuclei'. *Physical Review C*, **67**(024309) (2003)

[Ago03] S. Agostinelli et al. 'Geant4-a simulation toolkit'. *Nuclear Instruments and Methods in Physics Research Section A: Accelerators, Spectrometers, Detectors and Associated Equipment*, **506**(3) (2003) 250

[And04] A. N. Andreyev et al. 'GEANT Monte Carlo simulations for the GREAT spectrometer'. *Nuclear Instruments and Methods in Physics Research Section A*, **533**(3) (2004) 422

[Arm03] P. Armbruster. 'On the production of superheavy elements'. *Comptes Rendus Physique* (2003)

[Bas06] J. E. Bastin et al. 'In-beam gamma ray and conversion electron study of Fm250'. *Physical Review C*, **73**(2) (2006) 024308

[Bea92] C. W. Beausang et al. 'Measurements on prototype Ge and BGO detectors for the Eurogam array'. *Nuclear Instruments and Methods in Physics Research Section A*, **313** (1992) 37

[Bea96] C. Beausang and J. Simpson. 'Large arrays of escape suppressed spectrometers for nuclear structure experiments'. *Journal of Physics G: Nuclear and ...*, **527** (1996)

[Ben99] M. Bender et al. 'Shell structure of superheavy nuclei in self-consistent mean-field models'. *Physical Review C*, **60** (1999) 1

[Ben01] M. Bender, W. Nazarewicz, and P.-G. Reinhard. 'Shell stabilization of super- and hyperheavy nuclei without magic gaps'. *Physics Letters B*, **515**(1-2) (2001) 42

[Ben03] M. Bender, P. Heenen, and P. Reinhard. 'Self-consistent mean-field models for nuclear structure'. *Reviews of Modern Physics*, **75**(January) (2003) 121

[Boh37] N. Bohr and F. Kalckar. 'On the transmutation of atomic nuclei by impact of material particles'. *Mat. Fys. Medd. Dan. Vid. Selsk.*, **14**(10) (1937)

[Boh98] A. Bohr and B. Mottelson. *Nuclear structure.* World Scientific Publishing Company (1998)

[Bru97] R. Brun and F. Rademakers. 'ROOT An object oriented data analysis framework'. *Nuclear Instruments and Methods in Physics Research Section A: Accelerators, Spectrometers, Detectors and Associated Equipment*, **389**(1-2) (1997) 81

[But96] P. A. Butler et al. 'Electron spectroscopy using a multi-detector array'. *Nuclear Instruments and Methods in Physics Research Section A*, **381**(2-3) (1996) 433

[But02] P. A. Butler et al. 'Conversion Electron Cascades in $^{102}_{254}$No'. *Physical Review Letters*, **89**(20) (2002) 202501

[Cas01] R. F. Casten. *Nuclear Structure from a Simple Perspective (Oxford Studies in Nuclear Physics)*. OUP Oxford (2001)

[Cha06] A. Chatillon et al. 'Spectroscopy and single-particle structure of the odd- Z heavy elements ^{255}Lr, ^{251}Md and ^{247}Es'. *The European Physical Journal A*, **30**(2) (2006) 397

[Cha07] A. Chatillon et al. 'Observation of a Rotational Band in the Odd-Z Transfermium Nucleus $^{251}_{101}$Md'. *Physical Review Letters*, **98**(13) (2007) 132503

[Cox13] D. M. Cox et al. 'Transmission efficiency of the SAGE spectrometer using GEANT4'. *Fission and properties of neutron-rich nuclei - conference proceeding (To be published)* (2013) 1

[Ćwi96] S. Ćwiok, J. Dobaczewski, and P. Heenen. 'Shell Structure of the Superheavy Elements'. *Nuclear Physics A* (1996)

[Ćwi05] S. Ćwiok, P.-H. Heenen, and W. Nazarewicz. 'Shape coexistence and triaxiality in the superheavy nuclei.' *Nature*, **433**(7027) (2005) 705

[Esk71] K. Eskola et al. 'Studies of Lawrencium with Mass Numbers 255 Through 260*'. *Physical Review C*, **4**(2) (1971)

[Fie07] 'Vector Fields "OPERA Version 12"' (2007)

[Fir99] R. B. Firestone and S. Y. F. Chu. *Table of Isotopes, 8th Edition*. Wiley-Interscience (1999)

[Gai82] J. E. Gaiser. *Charmonium Spectroscopy form Radiative Decays of the J/Psi and Psi Prime*. Ph.D. thesis, Stanford University (1982)

[Ghi61] A. Ghiorso et al. 'NEW ELEMENT, LAWRENCIUM, ATOMIC NUMBER 103'. *Physical Review Letters*, **6**(9) (1961) 473

[GJ08] C. Gray-Jones. *Isomer Spectroscopy of* ^{254}*No*. Ph.D. thesis, University of Liverpool (2008)

[GM49] M. Goeppert-Mayer. 'On closed shells in nuclei. II'. *Phys. Rev* (1949) 1

[Gre08] P. T. Greenlees et al. 'High-K structure in ^{250}Fm and the deformed shell gaps at N=152 and Z=100'. *Physical Review C*, **78**(2) (2008) 021303

[Hau08] K. Hauschild et al. 'High-K, $t_{1/2}$ = 1.4(1) ms, isomeric state in ^{255}Lr'. *Physical Review C*, **78**(2) (2008) 4

[Her02] R.-D. Herzberg et al. 'In-beam spectroscopy of ^{253,254}No'. *The European Physical Journal A - Hadrons and Nuclei*, **15**(1-2) (2002) 205

[Her06] R.-D. Herzberg et al. 'Nuclear isomers in superheavy elements as stepping stones towards the island of stability.' *Nature*, **442**(7105) (2006) 896

[Her09] R.-D. Herzberg et al. 'Structure of rotational bands in ^{253}No'. *The European Physical Journal A*, **42**(3) (2009) 333

[Her11] R.-D. Herzberg and D. M. Cox. 'Spectroscopy of actinide and transactinide nuclei'. *Radiochimica Acta*, **99**(7-8) (2011) 441

[Jep09] H. B. Jeppesen et al. 'High-K multi-quasiparticle states and rotational bands in $^{255}_{103}$Lr'. *Physical Review C*, **80**(3) (2009) 5

[Kan04] H. Kankaanpää et al. 'In-beam electron spectrometer used in conjunction with a gas-filled recoil separator'. *Nuclear Instruments and Methods in Physics Research Section A*, **534**(3) (2004) 503

[Ket09] S. Ketelhut et al. 'γ-Ray Spectroscopy at the Limits: First Observation of Rotational Bands in ^{255}Lr'. *Physical Review Letters*, **102**(21) (2009) 212501

[Kib08] T. Kibédi et al. 'Evaluation of theoretical conversion coefficients using BrIcc'. *Nuclear Instruments and Methods in Physics Research Section A: Accelerators, Spectrometers, Detectors and Associated Equipment*, **589**(2) (2008) 202

[Kon01] F. G. Kondev et al. 'Identification of excited structures in proton unbound nuclei Au : shape co-existence and intruder bands'. *Physics*, **512**(July) (2001) 268

[Kra87] K. S. Krane. *Introductory Nuclear Physics*. Wiley (1987)

[Kru00] A. Kruppa, M. Bender, and W. Nazarewicz. 'Shell corrections of superheavy nuclei in self-consistent calculations'. *Physical Review C* (2000) 1

[Lal96] G. Lalazissis et al. 'Superheavy nuclei in the relativistic mean-field theory'. *Nuclear Physics A* (1996)

[Laz01] I. H. Lazarus et al. 'The GREAT triggerless total data readout method'. *IEEE Transactions on Nuclear Science*, **48**(3) (2001) 567

[Lei95] M. Leino et al. 'Gas-filled recoil separator for studies of heavy elements'. *Nuclear Instruments and Methods in Physics Research Section B: Beam Interactions with Materials and Atoms*, **99**(1-4) (1995) 653

[Möl92] P. Möller and J. Nix. 'Stability and decay of nuclei at the end of the periodic system'. *Nuclear Physics A*, **549** (1992) 84

[Möl94] P. Möller and J. Nix. 'Stability of heavy and superheavy elements'. *Journal of Physics G: Nuclear and Particle ...*, **1681** (1994)

[Moo07] S. Moon. *In-beam Gamma Spectroscopy Study of ^{253}No.* Ph.D. thesis, University of Liverpool (2007)

[Nil55] S. G. Nilsson. 'Binding states of individual neutrons in strongly deformed nuclei'. *Dan Mat Fys Medd*, **29**(16) (1955)

[Nil68] S. Nilsson, J. Nix, and A. Sobiczewski. 'On the spontaneous fission of nuclei with Z near 114 and N near 184'. *Nuclear Physics A*, **5** (1968)

[Nil69] S. Nilsson, C. Tsang, and A. Sobiczewski. 'On the nuclear structure and stability of heavy and superheavy elements'. *Nuclear Physics A*, **31** (1969)

[Nol94] P. J. Nolan, F. Beck, and D. Fossan. 'Large arrays of escape-suppressed gamma-ray detectors'. *Annual Review of Nuclear and Particle Science*, **45** (1994) 561

[Oga00] Y. Oganessian. 'Route to islands of stability of superheavy elements'. *Physics of Atomic Nuclei*, **63**(8) (2000) 1391

[Oga06] Y. Oganessian et al. 'Synthesis of the isotopes of elements 118 and 116 in the ^{249}Cf and ^{245}Cm+^{48}Ca fusion reactions'. *Physical Review C*, **74**(4) (2006) 044602

[Oga07] Y. Oganessian. 'Heaviest nuclei from ^{48}Ca-induced reactions'. *Journal of Physics G*, **34**(4) (2007) R165

[Pag03] R. D. Page et al. 'The GREAT spectrometer' (2003)

[Pap09] P. Papadakis et al. 'Towards combining in-beam γ-ray and conversion electron spectroscopy'. *AIP Conference Proceedings*, **1090** (2009) 14

[Pap10] P. Papadakis. *Combining in-beam γ-ray and conversion electron spectroscopy The sage spectrometer*. Thesis, University of Liverpool (2010)

[Pap12] P. Papadakis et al. 'A GEANT4 simulation package for the SAGE spectrometer'. *Journal of Physics: Conference Series*, **381**(1) (2012) 012051

[Par04] A. Parkhomenko and A. Sobiczewski. 'Proton one-quasiparticle states of heaviest nuclei'. *Acta Physica Polonica B* (2004)

[Par05] A. Parkhomenko and A. Sobiczewski. 'PHENOMENOLOGICAL FORMULA FOR α -DECAY HALF-LIVES OF HEAVIEST NUCLEI'. *Acta Physica Polonica B*, **36**(10) (2005) 3095

[Rah08] P. Rahkila. 'Grain - A Java Data Analysis System for Total Data Readout'. *Nuclear Instruments and Methods in Physics Research Section A: Accelerators, Spectrometers, Detectors and Associated Equipment*, **595**(July 2008) (2008) 637

[Rei04] P. Reiter. 'Nuclear Structure and Formation Mechanism of Heavy Shell-Stabilized Nuclei'. *Acta Physica Hungarica A) Heavy Ion Physics*, **19**(1-2) (2004) 127

[Rei05] P. Reiter et al. 'Structure of the Odd-A, Shell-Stabilized Nucleus $^{253}_{102}$No'. *Physical Review Letters*, **95**(3) (2005) 032501

[Rin04] P. Ring and P. Schuck. *The Nuclear Many-Body Problem (Theoretical and Mathematical Physics)*. Springer (2004)

[Ros09] D. C. Rostron. *Spectroscopy of ^{250}Fm using Tagging Techniques*. Ph.D. thesis, University of Liverpool (2009)

[Rub13] J. Rubert et al. 'First prompt in-beam γ-ray spectroscopy of a superheavy element: the ^{256}Rf'. *Journal of Physics: Conference Series*, **420** (2013) 012010

[Rud13] D. Rudolph et al. 'Spectroscopy of Element 115 Decay Chains'. *Physical Review Letters*, **111**(11) (2013) 112502

[Sch13] M. Schädel and D. Shaughnessy, editors. *The Chemistry of Superheavy Elements*. Springer (2013)

[She99] S. L. Shepherd et al. 'Measurements on a prototype segmented Clover detector'. *Nuclear Instruments and Methods in Physics Research A*, **434** (1999) 373

[Sto06] M. A. Stoyer. 'Island ahoy!' *Nature*, **442**(August) (2006)

[The93] J. Theuerkauf et al. 'TV'. *Private Communication* (1993)

[Wal99] P. M. Walker and G. D. Dracoulis. 'Energy traps in atomic nuclei'. *Nature*, **399** (1999) 35

[Wei35] C. F. v. Weizsäcker. 'Zur Theorie der Kernmassen'. *Zeitschrift für Physik*, **96**(7-8) (1935) 431

[Wei51] V. F. Weisskopf. 'Relative Transition Probabilities in Nuclei'. *Physical Review*, **83** (1951) 1073